U.S. Department of Energy

High Performance, Low Cost Hydrogen Generation from Renewable Energy

Subtitle	Program Final Report	*Sponsor*	U.S. Department of Energy, Energy Efficiency and Renewable Energy
Date	September 30, 2013	*Topic*	DOE DE-PS36-07GO97009 Topic 4
Dates Covered	September 1, 2009 – September 30, 2013	*Topic Title*	High Performance, Low Cost Hydrogen Generation from Renewable Energy
Principal Investigator	Dr. Katherine Ayers (203)678-2190 kayers@protonenergy.com	*TPOC*	David Peterson Phone: 720-356-1747
Contractor	Proton Energy Systems, Inc 10 Technology Drive Wallingford, CT 06492-1955	*Contract No.*	U.S. DOE, Energy Efficiency and Renewable Energy DE-EE0000276
Report No.	RPT1801	*Contract Value*	$3,396,826 (DOE share)

Table of Contents

Table of Figures

Table of Tables

1.0 Executive Summary

Hydrogen generation from electrolysis has been an important and cost effective process for industrial applications for decades. Hydrogen is a suitable replacement for helium in applications such as weather balloon filling, lifting gas for aerostats, and carrier gas for gas chromatography instruments, and OSHA requirements make onsite generation and low inventory increasingly attractive. Hydrogen is also used as a cooling gas in natural gas and coal power plants, many of which are in remote areas especially internationally, where delivery infrastructure is non-existent. Technology advancements therefore have immediate impact in the marketplace, and Proton has established a sustainable business with this industrial base.

As renewable sources of energy and fuels become an imperative for global environmental sustainability, energy storage also becomes an essential part of the puzzle. Renewable hydrogen from proton exchange membrane (PEM) electrolysis is gaining strong interest in Europe, especially in Germany where wind penetration is already at critical levels for grid stability. For this application as well as biogas conversion and vehicle fueling, megawatt (MW) scale electrolysis is required, and these applications represent billion dollar markets. However, the cost targets are more challenging than the existing industrial applications, and existing technology needs to be scaled up to meet the demands. Europe is putting significant investment into both materials research and product development for MW scale electrolysis. Proton has established a technology roadmap to achieve the necessary cost reductions and manufacturing scale up to maintain U.S. competitiveness in these markets, which require continued funding at the level of this program to achieve. This project represents a highly successful example of the potential for cost reduction in PEM electrolysis, and provides the initial stack design and manufacturing development for Proton's MW scale product launch.

The first task in this program was to establish the feasibility for significant reduction in the membrane electrode assembly cost through reduced use of precious metals and development of less labor intensive manufacturing processes. Focus was on the electrolysis anode, to bring this electrode in line with similar processes developed for the cathode. Reduction in catalyst loading of 50% was demonstrated to be possible, with further optimization of the process for better consistency and predictability. A subsequent SBIR program has further developed this technology to the point of commercialization and advancements in that program were incorporated into the large active area stack.

The remaining tasks focused on the bipolar assembly, which represented the largest cost in the legacy stack design. First, a comprehensive model was developed to integrate the electrochemical processes with flow distribution modeling. This model helped to streamline design efforts through the rest of the program. Cost reduction was then addressed in two phases. Immediate gains were possible through redesign and substitution of materials in the cathode flow field. This change was implemented within the first 18 months of the project and enabled over 15% reduction in stack cost. Additional research was then performed to achieve further cost reduction through more significant changes in design. New form factors for the bipolar assembly as well as new manufacturing methods were evaluated using a matrix approach and a final option was downselected.

In parallel, investigation of hydrogen embrittlement was performed in order to provide understanding of contributing factors and enable elimination of expensive treatment processes in the cell. Alternate coatings such as nitriding by various processes were examined as a function of hydrogen uptake and oxidative resistance. Initial results showed the impact of residual stress on hydrogen uptake and positive impact of nitrides on reducing embrittlement. Electrochemical testing showed feasibility of long term operation at high potentials with multiple titanium nitride compositions.

Based on these two subtasks, Proton finalized part dimensions and specifications to ensure that the part met the functional requirements of the electrolyzer, while maintaining manufacturability within the process control limits of the supplier. Final tooling was fabricated and small production runs were executed. The design was validated through inspection, cell measurements, and electrochemical performance. For Proton's 100 cm^2 active area stack, an overall cost reduction of 40% was achieved with the new design. The design was then scaled up in order to provide an initial stack for the MW electrolysis product. The scaled up design also provided approximately a 40% cost reduction vs. a previous design at large active area. This level of cost reduction was essential to compete in the marketplace even at product introduction. Production level part runs at the large active area were also completed and stack validation is in process. Based on the progress in this program and other parallel efforts, H2A analysis shows the status of PEM electrolysis technology dropping below \$3.50/kg production costs, exceeding the 2015 target.

Future work beyond this program includes final production documentation such as work instructions and acceptance testing procedures to commercialize both stack platforms. In addition, Proton has launched the system development effort for the MW-scale electrolyzer and is currently moving into the prototype phase. Cost analysis and market information indicates that the output of this program will support initial installations, but additional cost reduction is still required for long term commercial viability. The largest opportunity for cost reduction is to increase the output for a single cell stack through increasing number of cells and active area, not only for economies of scale in the stack but also for significant cost reduction in the power electronics subsystem. While the current design is scalable, limitations in the supply chain will require additional investment in manufacturing to remain competitive. Specific areas of need include continuing cost reduction of the membrane electrode assembly through reduction in catalyst usage and larger active area manufacturing capability, larger form factors for gas diffusion layer materials, and alternate sealing strategies to reduce membrane usage.

2.0 Introduction

With the ever-increasing addition of wind and solar renewable energy to the traditional electric grid, the need for energy storage also grows. Increased penetration of renewable sources of energy will require large energy storage systems in order to stabilize the supply and demand requirements. Hydrogen from electrolysis is a promising technology for renewable energy capture as it has the capability to store massive amounts of energy in a relatively small volume. Specifically, proton exchange membrane (PEM) electrolysis is a promising technology for hydrogen generation applications because of the lack of corrosive electrolytes, small footprint, and ability to generate at high pressure, requiring only water and an energy source. In addition, electrolysis can also provide ancillary services to the grid such as frequency regulation and load shifting resulting in multiple value streams. The hydrogen produced can alternatively be injected into the natural gas pipeline (thus making that energy carrier more green), in the production of high value chemicals such as ammonia, in upgrading of methanization-produced biogas, or used as a transportation fuel. DOE has laid out detailed targets for hydrogen and fuel cells with a focus on these end applications, particularly the transportation market.[1] For electrolysis, the overall production cost relies heavily on the cost of electricity. However, in applications where the electricity is provided by energy sources that would otherwise not be captured, the value proposition changes considerably.

Europe in particular has been committed to these pathways and is making heavy investment in both materials research and system design and development, as well as technology demonstration. The first area of interest is renewable energy capture. Germany alone has approximately 30 gigawatts of installed wind power, with another 65 gigawatts in the rest of the European Union.[2] Intermittent power changes can be over 80% for sources such as solar and wind, on minutes to hour-long time scales. Due to limitations in transmission capacity, 20% of the available wind energy is lost, which could be captured with effective energy storage means.[3] Therefore, in Germany, hydrogen is looked upon as a key part of the energy storage solution under “Energiewende,” their national sustainable energy transition plan. Germany is particularly interested in hydrogen-based energy storage due to the synergy with fuel cell transportation infrastructure, and in this context electrolysis would represent a multi-billion dollar market. Hydrogen also provides a unique link between the electric and gas grid infrastructures (often referred to as “Power-to-Gas”). Demonstration projects are underway with thirty Power-to-Gas demonstration projects already started or planned in Europe alone (Figure 1).

In addition, Germany is considered the global leader in biogas energy generation, with 18,244 GWh of generation in 2012 forecasted to grow to 28,265 GWh by 2025.[4] Without renewable hydrogen, the biogas conversion efficiency is poor (on the order of 50%). Significant decreases in carbon dioxide emissions can be realized through the subsequent injection of hydrogen and conversion to methane. The net conversion efficiency achieves 90% with the addition of renewable hydrogen, and large scale electrolysis is the enabling technology. Biogas production capacities thus also drive the need for megawatt (MW)-scale electrolysis and represent another multi-billion dollar market for hydrogen. This market is also synergistic with the renewable energy storage application and contributes to hydrogen’s flexibility and dispatchability (Figure 3).

Figure 1: Map of Power-to-Gas Projects

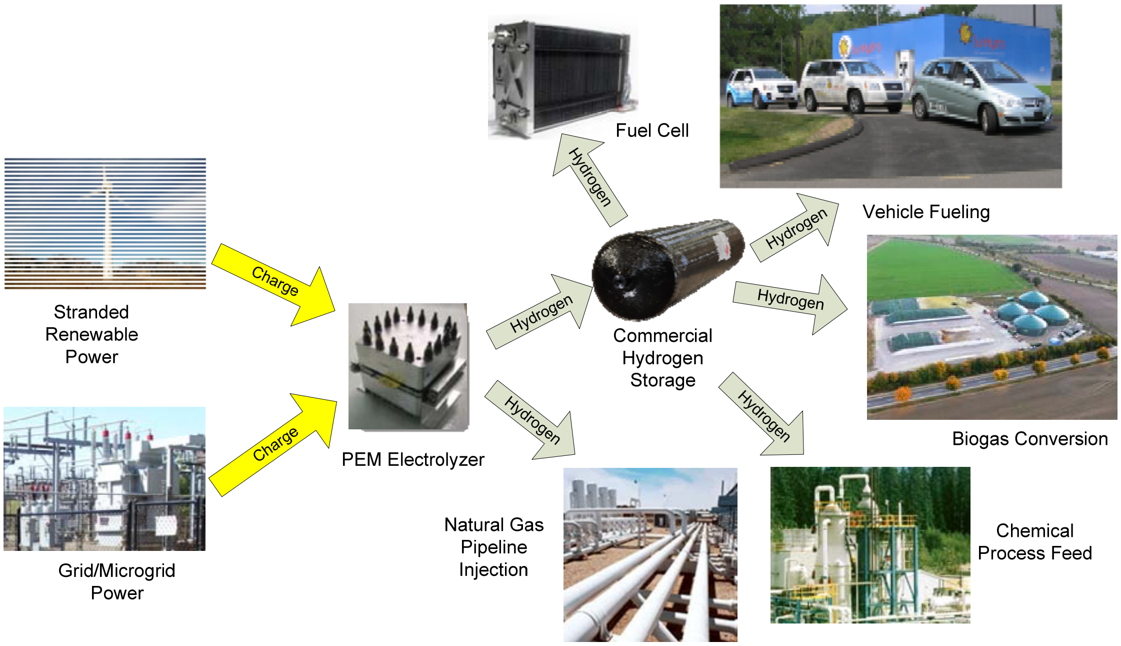

Figure 2: Hydrogen Flexibility as Energy Capture Media

Proton OnSite, the leader in PEM-based water electrolysis, is developing a MW-scale electrolyzer product in response to these emerging market demands. Proton's industrial hydrogen generators have a proven track record with more than 2000 units in customer hands in over 75 countries, representing an installed base of over 10 MW. Proton has built a successful, profitable, and sustainable commercial business around this technology, with a steady history of new product introduction (Figure 3) and compliance with international safety codes and standards.

Figure 3: Scale up of Proton Cell Stack and Systems

These products compete in the market today for industrial and government applications (Figure 4). Electrolysis has been used for decades for oxygen generation on space stations and submarines. High purity hydrogen is also utilized in manufacturing processes such as heat treating and semiconductor processing, as well as being used as a replacement for helium in analytical applications such as gas chromatography. Finally, hydrogen is used in many natural gas and coal power plants as a cooling fluid within the turbine windings. Distributed generation has advantages in many of these applications, from logistical challenges to safety issues in maintaining large hydrogen inventories. Typical payback for the PEM systems is 18-24 months, with some cases of less than 12 months achieved particularly in the power plant generator cooling markets. These payback times can be realized despite the present electrochemical inefficiencies, high precious metal loadings, semi-precious metal cell components, and inefficient hydrogen drying in the system.

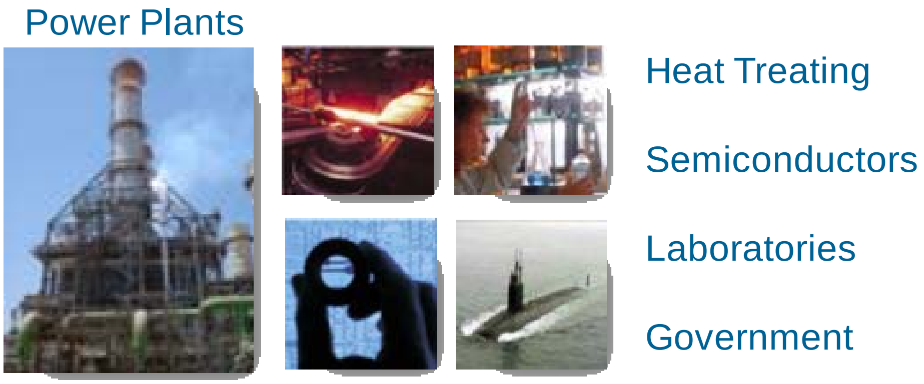

Figure 4: Existing Industrial Applications for Distributed Hydrogen Generation

However, for commercial energy markets, the main roadblocks to implementation are the capital and operating cost of the PEM electrolyzer. Proton has developed a technology roadmap to address the key cost and efficiency limitations of electrolyzers, and has demonstrated considerable progress in both, winning the DOE 2012 Hydrogen and Fuel Cell Technologies R&D Award. While PEM electrolysis technology has existed for many years, in general it has not been able to capitalize on many of the research advances in fuel cells due to the higher potentials and differential pressures in typical electrolysis cell stacks. PEM electrolyzers therefore still utilize legacy manufacturing processes which are highly energy and labor intensive. Figure 5 shows the cost pareto for the PEM cell stack, with the flow fields/separators (bipolar plate assembly), membrane electrode assembly, and labor representing over 75% of the cost.

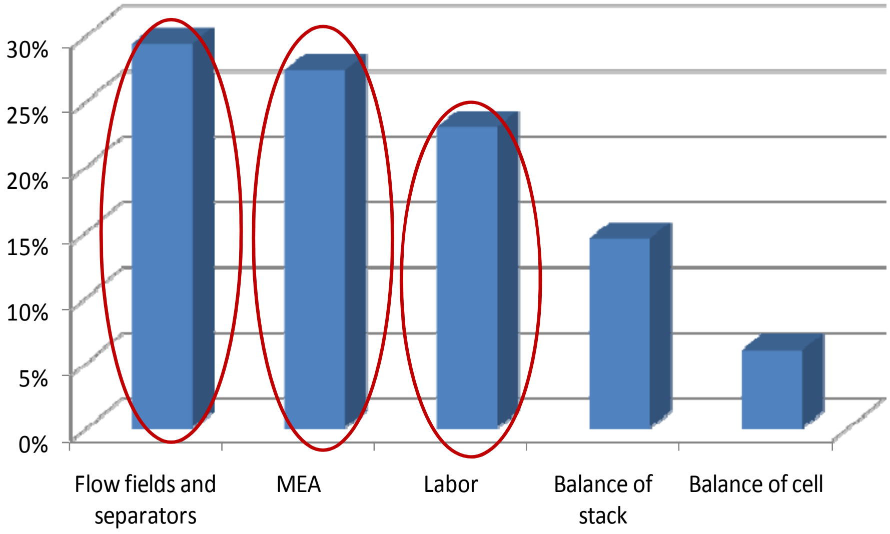

Figure 5: Cost Breakdown for 2009 Commercial Stack

This project is a primary component of Proton's technology roadmap. Within the period of performance of the program, Proton was able to address all three of these areas through development of improved MEA manufacturing processes, elimination of expensive cathode flow field materials, new manufacturing processes for the anode flow field and separator, and design scale up of over a factor of six. Specific project accomplishments are listed below:

- Demonstrated feasibility for reduced catalyst loading while maintaining desired electrical performance;
- Developed and qualified non-proprietary cell for collaborator use;
- Developed and validated a combined electrochemical and fluids model for prediction of behavior;
- Implemented 12% near term cost reduction in 2011 based on flow field material changes;
- Reduced additional part count through integration and elimination of complex subassemblies;
- Designed new assembly to enable high speed manufacturing process and qualified part at subscale;
- Scaled up active area for new manufacturing process, resulting in 40% cost reduction vs. the legacy large active area design; and
- Updated Proton's electrochemical interface to the new H2A model version and demonstrated near term pathway to \$5/kg H_2, high volume (>500 units/year) pathway to \$3.50/kg H_2.

3.0 Technical Background

3.1 Current Electrolyzer Technology Status

In addition to the large growth in energy markets discussed above, distributed hydrogen production via electrolysis for industrial applications is also still a growing market. Current commercial electrolysis technology involves two options: alkaline liquid potassium hydroxide (KOH) and proton exchange membrane (PEM)-based systems. PEM systems overcome many of the disadvantages of alkaline liquid systems, because the carrier fluid is deionized water, and the membrane-based cell design enables differential pressure operation. This approach enables inexpensive plastic components and simplest pressure control on the oxygen-water loop, and low hydrogen inventory allows installation without changing building classification. PEM systems are also much more efficient than alkaline liquid systems at the same current density. The liquid systems are limited by the much higher electrode separation vs. the membrane systems and the resistance of the separator media.

In the past, larger industrial applications were traditionally been dominated by liquid KOH systems. However, as PEM-based electrolyzers have reached similar output capacities, capital costs have become competitive with the alkaline liquid systems, and customers are beginning to understand the value proposition. These capital costs can be realized despite the present electrochemical inefficiencies, high precious metal loadings, semi-precious metal cell components, and inefficient hydrogen drying in the PEM systems. For the above applications, all of the major commercial entities have therefore committed to development of large scale PEM electrolysis for peak shaving and frequency modulation, including companies with well-established alkaline technology. Siemens, Hydrogenics, and ITM Power have all announced development in megawatt-sized PEM electrolyzers, and a large amount of funding has been allocated to European entities for research and development in PEM electrolysis. Maintaining U.S. competitiveness in this area is therefore crucial.

Proton's cell stacks are designed for extremely high reliability, with over 60,000 hours of operation demonstrated on the 200-400 psi commercial stack platform, and over 20,000 hours of operation on the high pressure 2400 psi stack developed in 2006 (Figure 6). Proton has continued to make significant year-over-year growth for the past few years despite continuing struggles in the overall economy.

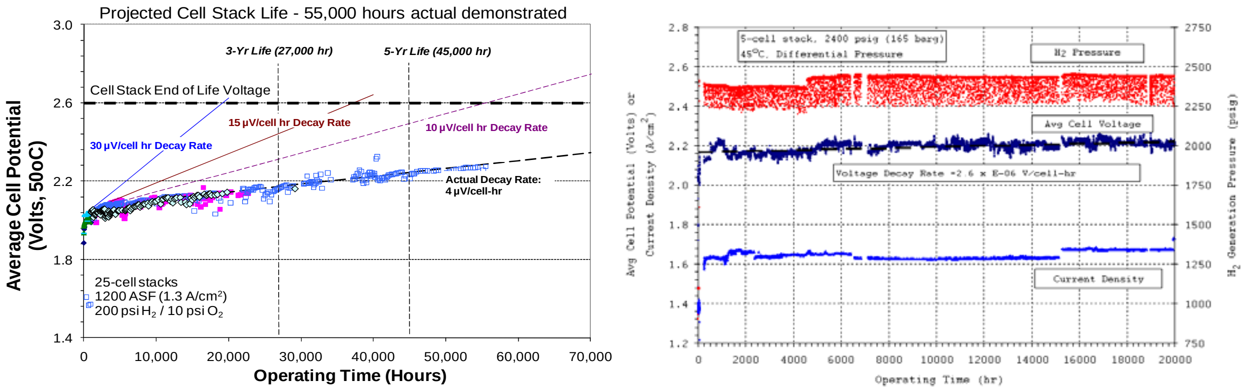

Figure 6: Electrolysis Stack Durability at 200 psi (60,000 hours) and 2400 psi (20,000 hours)

Past development in electrolyzer technology (prior to 2007) had not focused heavily on efficiency or cell stack cost reduction, instead centering on reliability, overall system capital cost relative to the existing markets, and sizing to meet the most common applications. Therefore, despite the relative maturity of electrolysis systems and products, substantial opportunities for materials improvements, efficiency increases, cost reduction, and scale-up exist.

Based on Proton's stable platform, Proton created a technology roadmap in 2008, in order to provide a pathway for adoption of PEM technology in energy markets. A key component of this roadmap is the ability to leverage advancements in fuel cells and other related electrochemistry and materials fields with marginal additional funding, nearly doubling the impact of the research funds already spent in those areas. The overall strategy has been to balance high and low risk projects and pursue short and long term pathways in parallel, in order to maintain steady improvement over time. Proton has also worked to match potential projects with the appropriate missions of the government agencies, including DOE, in order to address the needs of those agencies while advancing our existing and future commercial products. Projects leverage expertise and fundamental research capability of national labs and universities along with Proton's strong technical design skills and experience in commercialization. Proton has also shown a willingness and capability to invest its own funds as part of this strategy, demonstrating its long term commitment to the technology. This program has been highly successful to date.

Based on the emerging markets at MW-scale and Proton's commercial success in product scale up, Proton has launched a MW-scale electrolyzer design effort. Proton is already underway in the product requirements definition phase of this effort, and preliminary product concepts are being developed. Proton's stack roadmap for the MW stack is shown below (Figure 7).

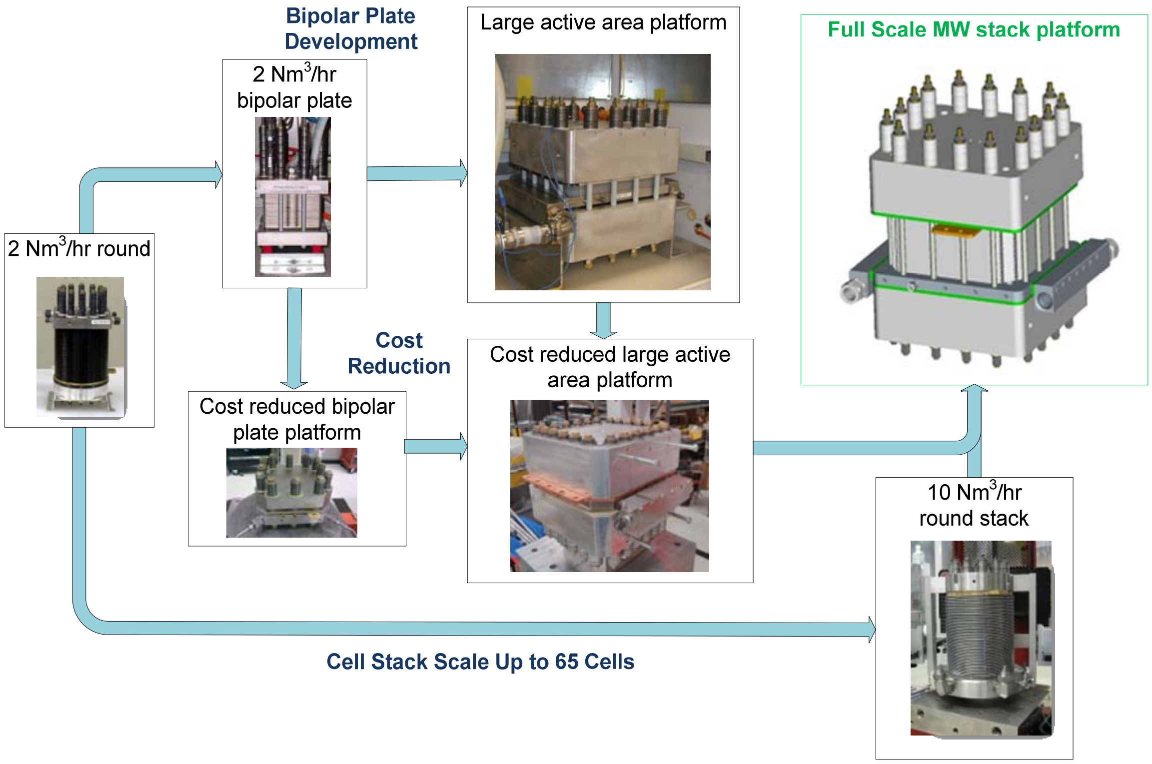

Figure 7: Cell Stack Roadmap for MW-Scale Electrolysis

Proton has already achieved significant validation at the required active area scale, using an initial design funded by MDA and TARDEC. Based on this experience, the design was cost reduced at both subscale and full scale active area under funding for this project, removing 40% of the cost through improvements in bipolar plate technology and initial MEA improvements. The investment from DOE is providing additional critical cost reduction opportunities for a product which is attempting to compete in very cost sensitive markets.

3.2 Key Areas of Study

Catalyst:

As mentioned above, electrolysis MEAs have not taken advantage of many of the advancements in manufacturing and electrode formulation made in the fuel cell field. Specifically, in the area of catalysts, the high potentials on the oxygen side of the cell preclude the use of carbon supports, resulting in high catalyst loadings to achieve sufficient coverage and reasonable operational voltages. At the beginning of the program, Proton had patented electrode formulations for the cathode, leading to improved distribution of the catalyst which enabled 50% reduction in loading. However, little work had been done for the anode. Because the cathode catalyst material typically consists of metal black nanoparticles, while the anode catalyst is often metal oxide-based, it was suspected that the electrode would require significant reformulation. In this program, the scope of the effort was to determine feasibility of making similar process and formulation improvements on the anode.

Bipolar Assembly:

The key focus of this project was cost reduction of the bipolar assembly. As seen in Figure 5 and Figure 8, this subassembly is the largest material cost contributor to the cell, as well as having a substantial labor component.

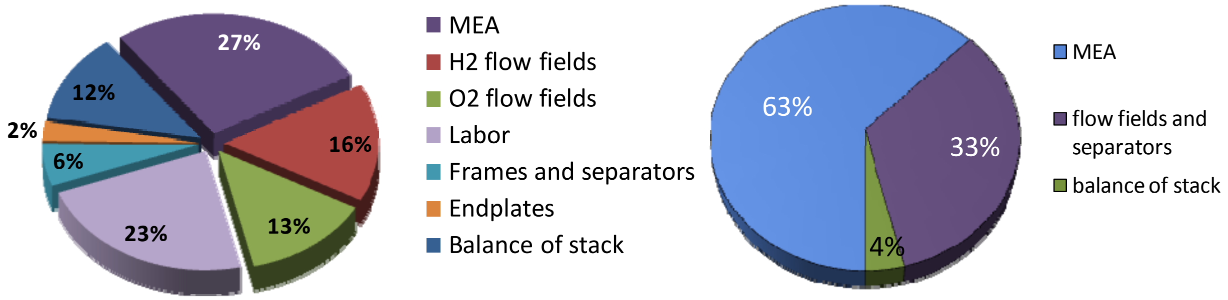

Figure 8: Cost Breakdown (Left) and Labor Breakdown (Right) for Major Stack Components

In order to design an improved component, an improved flow model was desired. Understanding of two phase flow is very important in electrolysis in particular to ensure proper water distribution on the oxygen side of the cell. For electrolysis, the relative gas and liquid flow depends on the cell electrochemistry and the operating cell current density. Therefore, an integrated electrochemical and fluid flow model was developed in order to narrow down the design options for an improved configuration.

Proton then pursued a 2-phase program for cost reduction and technology development of this part. Short term improvements involved replacement of the metal flow fields on the cathode (hydrogen) side of the cell with carbon, both for material and labor cost reduction and mechanical improvements to the cell. This step was relatively low risk based on past high pressure electrolysis work. In parallel, higher risk, higher reward approaches were planned for longer term study and development.

Finally, alternate surface treatments were evaluated to reduce the cost of the current processes used to mitigate hydrogen embrittlement and oxidation of the bipolar assembly on the cathode side of the cell, while providing oxidative resistance and maintaining conductivity on the anode. Nitriding has been demonstrated as one potential replacement for the conductive plating currently used. Different methods of adding a layer of titanium nitride to the surface of the part were therefore examined.

Scale Up: Active Area and Manufacturing

As discussed above, scale up of the stack design to an active area practical for MW-scale electrolysis is an important part of Proton's strategic mission. However, initial designs are developed at the subscale level, in order to validate concepts at lower cost and also enable product introduction at smaller scale, reducing financial risk. As part of the scale up effort, fluid distribution modeling of the proposed flow field channel and pore geometries are performed in order to design optimized configurations for improved water management, corrosion protection, and cell performance.

In addition, scale up of the manufacturing processes from laboratory or pilot scale to production is a vital part of product development. A key objective of this program was to transition parts to a process that was expandable in production volume without large amounts of additional capital investment. Compatibility of design features with equipment capability was considered and dimensions were modified to produce both a functioning part and consistent manufacturing.

Manufacturing Qualification

Qualification for production manufacturing involved iterations of tooling design to yield the desired quality of dimensions and features in the final part. Specific work instructions and acceptance test procedures were generated. Once the supplier qualification and procedures were developed, a pilot production run of several hundred bipolar plates was performed to validate the assumptions in the plate cost model and provide information to guide projections to larger volumes.

Cost Analysis

Validation of these design changes was achieved through cost analysis based on the H2A model. Proton has developed an electrochemical interface to the H2A model that integrates all the relevant parameters of electrolysis into the model. This interface includes polarization curve modeling based on membrane and catalyst parameters as well as ohmic losses, cell stack and system costs to the cell level, system and auxiliary power losses due to hydrogen permeation, hydrogen drying, power conversion, and thermal management. The cost model was utilized at both the subscale and large active area stack sizes in order to validate progress towards the DOE targets.

4.0 Experimental Methods

4.1 Task 1.0 Catalyst Optimization

In this task, optimization of the anode catalyst application process was performed in order to minimize loading. Differences in application method were expected to increase catalytic efficiency and utilization through optimization of the catalyst layer nanostructure. Variables such as catalyst preparation conditions, catalyst loading, and processing of the catalyst with the membrane were explored for impact on electrochemical activity.

Proton has patented formulations for platinum-based inks for electrolyzer cells. These formulas do not contain catalyst supports, based on traditional unsupported catalyst structures for electrolysis, especially on the anode side of the cell where potentials are too high to utilize carbon supports. However, despite this success on the cathode, past attempts at Proton to apply the ink methodology to the anode had proven unsuccessful, resulting in highly resistive electrodes and elevated, unstable operating voltages.

Ink Components

Inks are formulated to meet several requirements: compatibility with the printing process (viscosity and density), effective transfer to the membrane surface, uniformity of ink across the electrode surface, and acceptable electrochemical performance properties. The majority of printing inks consist of three component groups: 1) a pigment, typically a suspended solid and in this case the catalyst powder, 2) a “vehicle” or carrier fluid such as the ionomer solution, and 3) additives such as solvent and stabilizers to keep the ink from foaming or the catalyst from settling. In this case, the solid is the noble metal to be used as a catalyst in a water electrolysis cell stack. The resulting ink must be capable of homogeneous distribution onto the print substrate, followed by complete transfer on a printing press to be “decaled” to a membrane.

The nature and amount of the pigment that the ink contains, as well as the type of vehicle, contribute to the ink’s body and working properties (viscosity and density). The vehicle carries the pigment and adheres it to the substrate, and is composed mostly of resins and solvents. In the case of Proton’s cathode ink, the components of Nafion solution are polymers in a combination of water, ethers and alcohols. This vehicle carries the pigment, controls the flow of the ink on the press, and, after drying, binds the pigment to the substrate. The Nafion solution also provides the binding necessary for transfer onto the membrane during the heated bonding step conducted under mechanical compression.

The primary function of the solvent is to dissolve the binder and help to produce a fluid capable of being printed. The solvent selection is critical in determining performance of the printing ink and is governed by a number of factors. The solvent should dissolve the polymers chosen as binders and other additives. The solvent should also be easily removed by evaporation and interact minimally with other ink ingredients, thereby preventing ink instability. A typical additive used is polyvinyl alcohol (PVA), which enhances the ink characteristics by providing elasticity and preventing cracking of the electrode decal during the drying stage.

General Formulation Approach

The starting point chosen for this program was to formulate an ink with the same general composition as the cathode in order to baseline the performance of this formulation with the processing adjustments. The basic procedure used to create the ink batches was to place half of the total amount of water to be used in a beaker. Next, additives were introduced and the mixture was left to stir for several minutes. After this period, the Nafion dispersion was measured out and added to the warm mixture. The mixture was heated and stirred until it condensed to approximately half of its initial volume. After this evaporation period, the catalyst was weighed out and added to the remaining water in a separate beaker. After cooling the contents of the first beaker to room temperature, the catalyst-water suspension was added to the polymer mixture. A second evaporation period ensued, ending when the ink was condensed to the volume specified by the design. After the synthesis was complete, the composition of the ink was checked by measuring its density experimentally. This number was compared to an expected density, calculated by taking the average density of the components in the mixture, weighted by mass fraction.

Decal Preparation and Catalyst Loading Determination
After synthesis, the ink was applied to a Teflon sheet through a standard screen printing process. Once a decal was printed, it could be pressed onto a Nafion membrane to create an MEA, or used for a destructive loading test to determine the catalyst loading on the decal. It was assumed that all decals printed from a batch of ink had similar loading. The loading test involved cutting a decal into small strips and placing them into small preweighed ceramic crucibles to be heated to 650°C (1202°F) in an air environment. The extreme heat burned away all of the material except the catalyst. The amount of catalyst in the decal could then be determined by the difference in weight between the empty crucibles and crucibles with catalyst after heating. With a known print area, the catalyst loading in mass per area was determined.

Electrode Acceptance Testing
Electrical resistance was one of the desired methods for testing as-printed decals. Three measurements were taken to evaluate decal resistance, similar to current acceptance test protocol for MEAs: 1) a lateral resistance measurement, 2) a cross-cell resistance measurement, and 3) an in-cell resistance measurement. In theory, the lateral resistance measurement can be taken with a decal on a Teflon sheet before pressing or an MEA electrode. In this study, however, measurements taken of decals on Teflon invariably produced immeasurably high resistance numbers, and were not good indicators of decal quality. Therefore, only measurements on full MEAs were recorded. Prior to assembly in cells, visual inspections on the electrodes were also performed.

Operational Tests
MEAs which passed Proton's internal acceptance test protocol parameters were selected for use in integrated operational testing. Testing was supported for up to 300 hours to evaluate stability and durability in an electrolysis environment.

4.2 Task 2.0 Prototype Flow Field Development

In this task, flow field concepts were developed based on laminate structures and less expensive raw materials. In the initial part of the project, funding levels required focus on one or two options, with a longer term goal to investigate a broader range of manufacturing techniques. Modeling was also performed to determine the flow constraints for the current design in order to guide the redevelopment effort.

4.2.1 Subtask 2.1 Electrochemical and Fluids Model Development

The two-phase comprehensive PEM electrolyzer (PEMEL) model used in this project is based on the M^2 model originally developed by Wang and Cheng[5] and later extended to the fuel cell application by Wang et al.[6] The M^2 formulation is particularly suitable for two-phase PEMEL modeling. The M^2 model is a mathematical re-formulation of the classical two-phase model by viewing the multi-phase system as a chemical mixture. With this approach, multi-phase flow is then described in terms of a mass-averaged mixture velocity and diffusive flux, representing the difference between the mixture velocity and individual phase velocity. One major advantage of the M^2 model over classical two-fluid models is that it eliminates the need for tracking phase interfaces, thus simplifying the numerical complexity of two-phase flow and transport modeling. Another salient feature of the M^2 model for PEMEL is that all model equations are valid in all three types of regions possible in a PEMEL; single-phase gas, liquid-gas two-phase, and single-phase liquid. In addition, the M^2 model is mathematically equivalent to two-fluid models without invoking any additional approximations. Finally, the two-phase M^2 model can be easily devised to deal with the coupling of fluid flow, species transport and electrochemical reactions. These aforementioned advantages render the M^2 model to be a suitable two-phase flow and transport modeling framework for PEMELs.

Model Assumptions:

Utilizing the M^2 formulation for two-phase transport, the model incorporated the following assumptions:

- Ideal gas mixtures
- Laminar flow due to small flow velocities
- Isotropic and homogeneous porous diffusion media, characterized by an effective porosity and permeability.

Governing Equations:

With the above assumptions, the governing equations of mass, momentum, species, proton and electron transport in the M^2 model can be stated as:

Mass:
$$\nabla \cdot (\rho \vec{u}) = S_m \qquad (1)$$

Momentum:
$$\rho \vec{u} = -\frac{K}{\nu} \nabla p \quad \text{(Porous media)} \qquad (2)$$

Species:
$$\nabla \cdot (\gamma_c C^k \vec{u}) = \nabla \cdot (D_g^{k,eff} \nabla C_g^k) - \nabla \cdot \left[\left(\frac{mf_l^k}{M^k} - \frac{C_g^k}{\rho_g} \right) \vec{j}^{\,l} \right] + S_k \qquad (3)$$

Energy:
$$\nabla \cdot (\gamma_T \rho C_p \vec{u} T) = \nabla \cdot (k^{eff} \nabla T) + S_T \qquad (4)$$

Charge (electrons):
$$\nabla \cdot (\sigma^{eff} \nabla \phi_s) + j = 0 \qquad (5)$$

Charge (protons):
$$\nabla \cdot (\kappa^{eff} \nabla \phi_e) + j = 0 \qquad (6)$$

Source Terms:

The various source terms in the governing equations are the keys to the coupling of flow field, species transport and electrochemical reactions. There is a non-zero mass source in the mass conservation equation, S_m, arising from the summation of all species equations. It is assumed that in present model, the anode side consists of only oxygen and water species, while the cathode side consists of only hydrogen and water species. No species crossover through the membrane is considered as an initial approximation. Therefore the water equation is solved as a passive scalar in both anode and cathode side, with oxygen and hydrogen being the background fluid of the gas mixture in the anode and cathode, respectively. The mass fraction of oxygen and hydrogen can thus be simply calculated by $1-mf_{H_2O}$ in anode side and cathode side, respectively. Specifically one has:

$$S_{m,a} = M_{O_2}\frac{j}{4F} - M_{H_2O}\left[\nabla\cdot(n_d\frac{i_e}{F}) + \frac{j}{2F}\right] - \frac{K_m}{v_l}\nabla p \tag{7}$$

where $S_{m,a}$ is the mass source term in the anode catalyst layer (CL), and

$$S_{m,c} = -M_{H_2}\frac{j}{2F} - M_{H_2O}\nabla\cdot(n_d\frac{i_e}{F}) - \frac{K_m}{v_l}\nabla p \tag{8}$$

Where $S_{m,c}$ is the mass source term in the cathode CL.

The transfer current density, j, has positive value in the anode side and negative on the cathode side. The first terms in the right hand sides of the equations (7) and (8) are for oxygen and hydrogen generation, respectively. The second term in equation (7) is for water consumption and water flux through membrane via electro-osmotic drag. The third term in the equation (7) is for water transport through membrane due to hydraulic permeation under the pressure gradient between anode and cathode side. The source terms for water species equation is therefore:

$$S_{H_2O,a} = -M_{H_2O}\left[\nabla\cdot(n_d\frac{i_e}{F}) + \frac{j}{2F}\right] - \frac{K_m}{v_l}\nabla p \tag{9}$$

$$S_{H_2O,c} = -M_{H_2O}\nabla\cdot(n_d\frac{i_e}{F}) - \frac{K_m}{v_l}\nabla p \tag{10}$$

The source terms in the charge equations are used to describe the transfer current between the electronic and electrolyte phases inside of each anode and cathode CL. The transfer current densities are represented by the simplified Butler-Volmer kinetics equations as follows:

OER: $j = ai_{0,a}\left(\frac{C_{O_2,ref}}{C_{O_2}}\right)^{\gamma}\exp\left(\frac{\alpha_a F}{RT}\eta_a\right)$ in anode CL (11)

HER: $j = ai_{0,c}\left(\frac{C_{H_2,ref}}{C_{H_2}}\right)^{\beta}\left(\frac{\alpha_a+\alpha_c}{RT}F\eta_c\right)$ in cathode CL (12)

The activation overpotentials are defined as:

Anode CL $\eta_a = \phi_s - \phi_e - U_0$ (13)

Cathode CL $\eta_c = \phi_s - \phi_e$ (14)

The heat sources due to the electrochemical phenomena need more elaboration. The total heat release in an electrolyzer can be derived according to thermodynamics. The reversible heat release, also called the entropic heat release, can be written as $j\cdot T\frac{dU_0}{dT}$. It is positive (i.e. a heat source) for fuel cells since the water formation reaction from hydrogen and oxygen is an exothermic reaction. It is, however, negative (i.e. a heat sink) for the electrolyzer due to the endothermic nature of the water splitting reaction. Other heat sources terms have a positive sign for both fuel cell and electrolyzer, namely $\frac{i_e^2}{\kappa^{eff}}+\frac{i_s^2}{\sigma^{eff}}$ for the ohmic heating and $j\eta$ for the heating from activation polarizations, both of which are irreversible heat release.

Two-Phase Flow in Channels:
The present modeling approach is to view all components in an electrolyzer as porous media. The channels can be regarded as a structured porous media or a bundle of straight capillary tubes. The analogy between the PEM fuel cell (PEMFC) channels and the porous media was elaborated by Wang and Wang.[6]

Hence, Darcy's law is used to describe two-phase flow and transport throughout the entire PEMEL domain including the channels. The absolute permeability K in the Darcy's equation is an intrinsic geometrical property for both channels and porous media. Its value for porous media has to be determined by experiments or more advanced microscopic modeling methods. The absolute permeability for the flow channels can be computed by numerical experiments of simulating single-phase flow through the flow channels. Under the laminar flow assumption, the absolute permeability for channels can also be determined through the well-known Hagen-Poiseuille equation:[7]

$$K = c\frac{d_h^2}{32} \qquad (14)$$

where c is the shape factor describing various cross-section of channels and d_h is the hydraulic diameter of the channel:

$$d_h = 4\frac{\text{cross-section area}}{\text{channel perimeter}} \qquad (15)$$

Two-Phase Mixture Relations:
The two-phase mixture density and velocity are given by:

$$\rho = \rho^l \cdot s + \rho^g \cdot (1-s) \qquad (16)$$

$$\rho\vec{u} = \rho^l \vec{u}^l + \rho^g \vec{u}^g \qquad (17)$$

Here, s and (1-s) denote the volume fraction of the open pore space occupied by liquid and gas phases, respectively. The liquid saturation, s can be expressed as a function of mixture water mass fraction:

$$s = \frac{\rho m_w - C_{sat} M_w}{\rho^l - C_{sat} M_w} \qquad (18)$$

The individual phase flux is expressed by Darcy's law using the concept of relative permeability as follows:

$$\rho^l \vec{u}^l = -\frac{k_r^l K}{\nu^l} \nabla P^l \qquad (19)$$

$$\rho^g \vec{u}^g = -\frac{k_r^g K}{\nu^g} \nabla P^g \qquad (20)$$

where the relative permeability of individual phase is assumed to be proportional to phase saturations, raised to the fourth power, i.e.:

$$k_r^l = s^4 \quad k_r^g = (1-s)^4 \qquad (21)$$

In addition, the mixture kinematic viscosity and the mobility of each phase in the multiphase mixture are defined as:

$$\upsilon = \left(\frac{k_r^l}{\nu^l} + \frac{k_r^g}{\nu^g}\right)^{-1} \qquad (22)$$

$$\lambda^l = \frac{k_r^l}{\nu^l}\nu = \frac{k_r^l / \nu^l}{k_r^l / \nu^l + k_r^g / \nu^g} \qquad \lambda^g = 1 - \lambda^l \qquad (23)$$

The second term on the left hand side of the species equation (3) represents the advective term, in which the advection correction factor, γ_c is given by:

$$\gamma_c = \frac{\rho}{C_{H_2O}}\left(\frac{\lambda^l}{M_{H_2O}} + \frac{\lambda^g}{\rho^g}C_{sat}\right) \tag{24}$$

In the M^2 model, a diffusive mass flux of each phase relative to the whole multiphase mixture is defined. The diffusive mass flux of liquid phase, $\vec{j}^l$ can be expressed as a function of capillary pressure, P_c such that:

$$\vec{j}^l = \rho^l \vec{u}^l - \lambda^l \rho \vec{u} = \frac{K}{\nu}\lambda^l \lambda^g \nabla P_c = \frac{\lambda^l \lambda^g \sigma \cos(\theta_c)}{\upsilon}(K\varepsilon)^{1/2}\frac{dJ}{ds}\nabla s \tag{25}$$

The capillary pressure, P_c is expressed as:

$$P_c = P^g - P^l = \sigma \cos\theta \left(\frac{\varepsilon}{K}\right)^{1/2} J(s) \tag{26}$$

where ε is the porosity and K the permeability of porous media, and θ is the contact angle. Leverett function, *J(s)* is given for both hydrophobic and hydrophilic porous layers as:[8]

$$J(s) = \begin{cases} 1.417(1-s) - 2.120(1-s)^2 + 1.263(1-s)^3 & \text{if } \theta < 90^\circ \\ 1.417s - 2.120s^2 + 1.263s^3 & \text{if } \theta > 90^\circ \end{cases} \tag{27}$$

Boundary conditions

A benefit of the current two-phase electrolyzer model is that only minimum amount of boundary conditions are required in the calculation. All of the interfacial boundary conditions between different layers have been taken care of automatically. The inlet velocity is determined by flow stoichiometry, average current density, active area of the membrane, inlet species concentration and the cross-sectional area of channels, as the following:

$$u_{in} = \frac{St\, I_{avg}\, A_{mem}}{\alpha F C^k A_{in}} \tag{28}$$

where F is the Faraday constant and α is the charge number. Liquid water is assumed to be fed into the channels, and thus the water molar concentration at inlet is equal to the liquid water concentration.

The outlet boundary condition is assumed to be fully developed:

$$\frac{\partial \vec{u}}{\partial n} = 0,\ P = P_{ref}, \frac{\partial C^k}{\partial n} = 0, \frac{\partial T}{\partial n} = 0 \tag{29}$$

At all wall boundaries we have:

$$\vec{u} \cdot n = 0, \frac{\partial P}{\partial n} = 0, \frac{\partial C^k}{\partial n} = 0, \frac{\partial T}{\partial n} = 0 \qquad (30)$$

The following boundary conditions are exerted for the charge transfer equations:

$$\phi_s |_{cathode\,wall} = 0, \frac{\partial \phi_s}{\partial n} |_{anode\,wall} = I_{avg} \qquad (31)$$

$$\frac{\partial \phi_s}{\partial n} |_{mem-cl} = 0 \qquad (32)$$

$$\frac{\partial \phi_e}{\partial n} |_{cl-gdl} = 0 \qquad (33)$$

Numerical Procedures
The governing equations, Eq. (1) to Eq. (6) are coupled nonlinear partial differential equations and can only be solved by numerical methods. The equations along with the appropriate boundary conditions are discretized by the finite volume method and solved in a commercial CFD code, Star-CD, by SIMPLE algorithm. The source terms and various physical properties are implemented using the user-defined functions (UDF) in Star-CD. Overall species and charge balance are checked in addition to the equation residuals as important convergence criteria.

4.2.2 Subtask 2.2 Flow Field Design and Fabrication

Subtask 2.2 Plastic Frame Design and Fabrication
As discussed above, the initial phase of cost reduction involved maintaining Proton's basic cell construction but replacing the highest cost metal components on the cathode side of the cell with carbon. This effort required modifications to the legacy cell design in order to accommodate the form factor for the lower cost materials. For example, the cell frame needed to be modified. A combination of mechanical analyses and information gathering was completed in order to determine the optimal geometry and thicknesses of critical features. Structural analyses were performed using either fundamental equations or finite element analysis software. Specifically, a comparison study was conducted to see how the load requirements for the newly proposed frame would compare to other existing designs. Various elements of manufacturing design were addressed through collaboration with the supplier.

Stress calculations were performed in specific zones known to experience high stress concentrations. The selected element represented the material spanning a single flow channel in the frame. The results of analyses on this element should then be indicative of other similar elements. The fundamental modes of failure in these zones were determined to be shear and bending of these span wise members. Shear analysis and bending analysis were performed and then de-rating factors were applied to ensure that required safety factors would be met. This modeling was done at higher operating temperatures than Proton's existing commercial products, since higher operating temperatures are a part of Proton's long term technology roadmap. It should be noted that although these calculations provide reasonable approximations for the stresses in cell components, they are better interpreted as a means of providing a relative comparison to existing parts, such that existing design values are maintained.

Once the frame parameter space had been defined, a downselect of the design was performed based on manufacturability of parts, similarity to existing tooling, compatibility with higher operating pressure, and other considerations. These dimensions then determined critical dimensions for the other corresponding cell parts. A decision was made to keep the anode components fixed and make adjustments only to the cathode and frame gasketing until desirable performance was achieved. The challenge with this approach is that it limited the degrees of freedom in the design. Since there was a desire to maintain the same endplate load for the new design as was specified for the legacy design, the active area pressure would have to be very similar. For a given endplate load, a significant change to the ratio of active area pressure to seal area pressure could result in either an inability to seal or unacceptably high cross-cell resistance. Prototypes were therefore fabricated in a range of thicknesses to be tested in a range of configurations.

New fixtures were also fabricated to ensure accuracy and repeatability during the assembly of the new flow fields to ensure concentricity of all components. In an effort to reduce variability wherever possible, a simple new tool was created to provide tighter control of concentricity. The assembled units were characterized using both ex-situ and in-situ tests with laboratory test equipment and pressure film analyses. These activities aided in the determination of free height, as well as the average pressure and height while compressed. The objective was to ensure adequate support of the MEA while maintaining the ability of the cell to seal against both cross-cell and overboard leaks up to the desired proof pressure.

For each configuration considered, a single cell stack was built, taken through Proton’s standard processes, and proof pressure tested. In addition to these steps, pressure films were also collected during assembly and disassembly. The purpose of the pressure film analysis was to better quantify the active area pressure in the cell, as well as verify continuity of loading on the sealing features in the seal area. Cross-cell resistance was also used as a rough indicator of active area pressure. Lower resistance readings implied higher active area pressure while higher resistance readings implied lower pressure.

Balanced pressure hydrostatic proof testing was using a hydrostatic hand pump test. Each cell stack assembly was plumbed to the test rig, primed with water, purged of gas, and then gradually pressurized. The objective was to achieve a pressure decay of less than 25 psig over a three minute trial at a pressure of 650 psig (1.5 times operating pressure).

Subtask 2.3 Metal-Composite Laminate Plate Design and Fabrication

In the initial year of the project, budget was limited to pursuing a single alternative for potential long term cost reductions. Based on the existing level of knowledge around the different options, pursuing a carbon plate design with an impermeable coating was judged to be the top priority for determining feasibility. Proton worked with Entegris to make plates and coat them with titanium or titanium nitride.

Electrochemical Testing of Samples

The first stage of testing was designed to evaluate the quality of the titanium coating and corrosion resistance for the substrate material. Efforts within this stage included visual examination of sample parts followed by *in-situ* electrochemical testing. Examinations of the parts after being exposed to actual electrolyzer cell operating conditions provided an indication of stability. Materials included sealed and unsealed versions of high performance graphite as well as conductive thermoset plastics. Samples were vapor deposition coated with either a two step titanium / titanium nitride or a single step titanium coating. Some combinations were not possible due to incompatibilities between the substrate material properties and the coating process conditions.

For initial testing, round sample discs were designed to be placed as inserts in modified flow fields within the anode cavity of the cell. This was done to allow for the exposure of the various samples to the electrolysis environment without having to do any extensive design work or advanced fabrication of bipolar plates. It was anticipated that if the titanium coating was not uniform and continuous, the substrate would corrode and carbon dioxide would be released into the water flow stream. It was also believed that this would not negatively impact the test rig. Specialized flow fields were developed for this test in order to accommodate the graphite discs, to form a deep pocket once assembled (Figure 9).

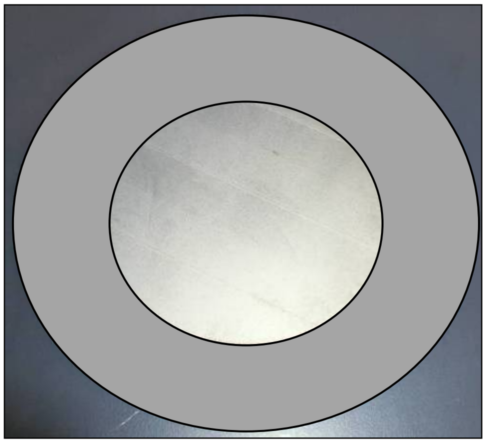

Figure 9: Coated Carbon Sample in Obscured Flow Field Pocket

To monitor corrosion, each sample was measured on an analytical balance both before and after operation. For consistency, the parts were allowed to dry thoroughly after being taken out of the pocketed screen packs before taking their final mass. Prior to assembling the samples into test cells, the parts were also analyzed visually. The parts with a titanium base coat followed by a titanium nitride final coat, had a brighter, more golden appearance than parts having only the titanium nitride. Simple tape tests at Entegris indicated that adhesion of the nitride layer was greatly improved with the two step process.

Testing was performed using 3-cell stacks within which two cells contained pocketed flow fields and samples. In every case, the third cell was assembled with a control flow field as a baseline. After passing Proton's acceptance testing protocol (ATP), the stacks were run for 500 hrs at 100 psig. After operation, each cell stack was removed from the test stand and taken through ATP again. The stacks were then disassembled and the sample parts were analyzed.

Material Testing of Samples

The second stage of testing was designed to evaluate the mechanical strength, material compatibility, and durability of the uncoated carbon materials as well as the ability of the manufacturer to successfully create sealing features. Efforts within this stage included material property data collection in conjunction with mechanical compression testing. Although actual production components would incorporate molded features rather than machined, it was anticipated that the use of machined samples would provide representative and conservative results. In an effort to further characterize the compatibility of these alternative materials, small samples of each material were also used to conduct a non volatile residue (NVR) test.

A simple way to verify the strength of the alternative materials was to apply the same range of pressures to the samples that would be required in an actual cell design. Any cracking or breakdown of the test strips would indicate inadequate strength. Before commencing with compression trials, each test strip was examined under the laboratory microscope and photographed to document its baseline condition. Thickness readings were also taken for reference. Once characterized, each test strip was placed on a steel platen, and then covered with a strip of gasket material. A piece of pressure film and a load concentrator block were then placed over the gasket to ensure a fixed contact area between the upper platen and the sealing features. With a known contact area, it was possible to correlate applied force with desired pressure. In order to avoid the possibility of immediate damage, each sample was loaded in gradually increasing steps to sealing pressures required for a 30-bar capable design. A new pressure film was used and a visual inspection was performed between each step. After completing the compression trials, the samples were carefully examined again under the microscope and measured to check for plastic deformation.

Electrochemical Testing of Functional Cell Components

Although the round samples were exposed to the corrosive conditions in the anode cavity of the test cells, they were not forced to conduct all of the electrical current through the cell. The perimeter of the original flow field was still in contact with the separator, thus allowing current to flow around the relatively higher resistance alternative materials. In order to quantify the performance penalty caused by higher resistance materials, it was necessary to fabricate and test a variety of functional cell components. Test parts included full bipolar plates from the carbon base components as well as anode and cathode flow field inserts. The bipolar plates were machined to the existing drawings. Upfront CFD analysis was used to design networks of flow channels which provided uniform coolant flow across the entire active area of the cell with minimal pressure drop.

Examination of Functional Parts

Prior to assembly, the functional parts were examined in a similar fashion as the round samples. A key difference between these parts and the previous samples was the inclusion of complex features and flow field geometries. While the coatings seemed sufficient on the top surfaces and sealing features, some of the flow channels and through holes appeared to have lower uniformity of coating (Figure 10). Some parts also tended to have defects presumed to be related to the fixturing process (Figure 11). These defects were closely examined after operation to check for growth of the defect area or corrosion.

Figure 10: Through Holes

Figure 11: Fixture Marks

4.3 Task 3.0 Prototype Bipolar Plate Development

In this task, efforts were continued to assess additional bipolar plate concepts based upon laminate structures and simple forming methods that are applicable to high volume manufacturing. Lamination technologies examined included metal-to-metal bonding, metal-to-plastic bonding and metal-to-composite bonding. Each approach was investigated in parallel to determine which technology could yield the lowest cost plate while meeting the necessary technical requirements.

4.3.1 Subtask 3.1 Manufacturing Downselect

A detailed evaluation of a broad range of metal-composite bipolar assemblies were categorized and a set of criteria to evaluate the range of options was created. The information required to complete the critical evaluation was gathered through preliminary design sketches, concept 3D designs, and discussions with fabrication suppliers. Criteria for each of the metal-composite bipolar designs was entered into a decision matrix to understand the potential cost reduction impacts and the level of technical maturity of the fabrication processes. From this analysis, several proof-of-concept feasibility tests were identified to further facilitate a down-select in metal-composite bipolar assembly approaches.

Supplier visits and conference calls were completed to further assess the options and understand critical issues for the top five candidates. Experimental plans were developed to obtain parts for concept validation and address early potential issues. Quotes were obtained for prototype parts and larger volumes of production runs (up to quantities of 10,000). A decision matrix was created to evaluate top candidates for fabrication methods. Criteria included level of risk (cost, reliability, and material), non-recurring costs (tooling and development), piece cost, and process maturity/development time. Limited experiments were performed on conceptual parts incorporating key features to determine feasibility. A concept review was performed with selection of a main option for future work and a backup option. Initial design efforts were performed at the 100 cm^2 active area level, to be scaled up as part of Subtask 4.3.

Based on the output of the concept review, a model was developed to represent two-phase flow distribution from a header to cell plates incorporating proposed flow field designs. CAD drawings of candidate bipolar assemblies and tooling to fabricate them were generated, and flow distribution based on computational fluid dynamics (CFD) was performed across the plate to verify uniformity. Finite element analysis (FEA) was also performed to ensure all stresses in the part were within acceptable design limits. Components were supplied to Proton for initial stack level design. The surrounding gas diffusion layers and gasketing had to be designed based on the actual part dimensions and tolerances. Flow testing and pressure film testing was performed in order to verify the results of the CFD modeling and FEA analyses before operational cells were built.

4.3.2 Subtask 3.2 Hydrogen Resistant Coatings

In this task, surface treatments were explored in order to reduce the cost and increase effectiveness of the current processing steps for mitigating hydrogen embrittlement of the bipolar plate, while providing surface conductivity. These methods included annealing, thermal nitriding, plasma nitriding, and reduction in plating content.

Test coupons from treated parts were sent to Oak Ridge National Lab for characterization before samples were fabricated for electrochemical testing. Analysis included layer thickness, uniformity, and composition. Depth was measured by microhardness measurements or sputtering of the surface with periodic XPS measurements. Accelerated hydrogen uptake testing was also performed at Oak Ridge by placing various samples in a sealed vessel filled with hydrogen at elevated temperature and pressure. Based on Arrhenius relationships, 100 hours of testing at these conditions should roughly correspond to 10 years of electrolysis operation at room temperature. Tests were performed for up to 400 hours and hydrogen uptake was periodically measured by weight change. In addition, residual stress measurements were taken after different process steps in order to determine whether stress in the part was contributing to uptake, and when it was introduced during processing.

Electrochemical testing was then performed on different types of nitrided samples to determine the oxidative stability of the coating on the anode side of the cell. Test parts were initially tested at Oak Ridge to examine the impact of different alloys and nitriding processes on performance, compared to a plated or unplated baseline. Parts were visually examined after operation and also characterized by XPS.

Promising processes from the Oak Ridge investigation were used to treat production parts for Proton electrochemical testing. High pressure testing in Proton's 2400 psi cell stack hardware was performed to check correlations with the accelerated hydrogen uptake measurements. Long term tests were also initiated to examine potential loss of nitride or part oxidation during operation.

4.4 Task 4.0 Prototype Bipolar Plate Evaluation

4.4.1 Subtask 4.1 Operational Testing

Based on the output of Task 3 and the resulting bipolar assembly design, parts were manufactured for cell stack verification. Single cell stacks were built and proof tested to at least 1.5 times the operating pressure of 30 bar using hydrostatic testing. Similar to the MEA testing described above, Proton's standard acceptance test procedures (ATP) were utilized to test the integrity of the stack before operation. Proton's stack ATP is comprised of three assessment elements in addition to operation at full current and pressure: 1) a high frequency resistance measurement conducted at ambient and full pressure conditions to ensure minimal resistive losses in each cell, 2) an electrical isolation measurement to check for the absence of potential shorting in or between cells, and 3) a pressurized leak test at up to 1.5 times normal operating pressure to ensure there is no evidence of a cross-cell or overboard leak. Cells were operated for several hundred hours to evaluate stability and performance. Automated data acquisition was used to log relevant information including inlet/outlet temperature, pressure, current, and voltage. Current-voltage polarization curves were conducted periodically to characterize activation and ohmic losses in comparison to baseline performance.

4.4.2 Subtask 4.2 Post Operational Testing Analysis

For the initial single cell stacks, visual teardown analyses of the cell stacks were conducted. Cell components were examined for evidence of degradation or delamination. Plates with alternate surface treatments were submitted for hydrogen uptake analysis.

4.4.3 Subtask 4.3 Stack Scale Up

The results of Subtasks 4.1 and 4.2 were used to make final design decisions and downselect to a single candidate configuration for further manufacturing scale-up and cost analysis. Proton's full validation process typically involves operation of a full commercial scale stack (at least 10 cells) for 5000 hours. A 10-cell stack was therefore built for long term testing.

Based on initial results of the 3-cell testing, scale-up efforts were also initiated for a cell stack of greater than 500 cm^2 active area. The electrode form factor was determined by considering the current limitations of Proton's supply chain while maintaining design symmetry with the 100 cm^2 active area design. The flow field was then modeled based on similar CFD and FEA analysis to the 100 cm^2 design. An analogous design effort was undertaken to the 100 cm^2 design, including dimensional tolerancing, flow testing, seal testing, and operational testing.

4.5 Task 5.0 Bipolar Plate Manufacturing Development

In this task, evaluation of the down-selected prototype bipolar plate design were continued in order to evaluate the material's long-term durability. In addition, initial studies of manufacturability were conducted. Critical suppliers were identified and manufacturing equipment and test equipment were specified at a preliminary level. Initial characterization of manufacturing tolerances, uniformity and process yield were completed.

4.6 Task 6.0 Bipolar Plate Manufacturing Qualification

In this task, critical suppliers were qualified based on Proton's internal ISO processes. This qualification included the design and fabrication of tooling dies for the chosen scaled up manufacturing process. Iterations were conducted to develop the tooling to yield the quality of dimensions required for a pilot production run consisting of several hundred plates. Parts were inspected based on critical drawing dimensions. Similarly, parts were treated for hydrogen uptake using the large scale equipment expected to be utilized for ongoing production runs. These manufacturing sets were used to validate the assumptions present in the plate cost model and provided information that can be used to guide the projections to larger volumes. A 10-cell stack was also built at the larger scale active area for long term durability testing.

4.7 Task 7.0 H2A Model Cost Analysis

An electrolysis cell stack system model designed to determine component performance requirements and to estimate the $/kg impact from implementing advanced catalysts and bipolar plates had been developed under a previous DOE sponsored program. This model apportions the overall electrolysis system cost across the major electrolysis subsystems, including that for the cell stack. The cell stack model provides further cost resolution based on electrochemical performance inputs. The resulting values are then integrated as inputs to the H2A model. In this task, the estimated component costs served as inputs to the existing model in order to quantify the impact of design changes developed in Tasks 1-3 on the $/kg cost of hydrogen. An initial analysis was performed as part of the downselect process at the end of Task 2, and a final analysis of the preferred configuration was performed at the end of the program.

5.0 Results and Discussion

5.1 Task 1.0 Catalyst Optimization

Baseline Formulation

The first batches of ink manufactured showed deviations between the intended density and measured values, reflecting a difficulty in controlling the final ink composition by volume. An area that was identified as a potential source of error was the final condensing step to a fixed volume. With the small ink volumes being produced in this study, if the final volume was off by a few milliliters, the catalyst loading in the ink changed significantly. Weight was therefore used as a more sensitive measure to control the final composition of the ink.

Loading consistency was also initially an issue. The anode ink did not have the same flow properties as the cathode ink, even at similar viscosities, likely due to differences in the surface characteristics of the catalyst powders and interaction with the ink components and print media. Scaling the catalyst loadings from a baseline formulation required decisions on which formula ratios to keep constant. It was recognized that changing the amount of one component of the formulation relative to the others could change the properties of the formulation. As discussed below, formulation development was therefore needed for the anode ink.

To help decouple the formulation step from the printing step, additional analytical steps were taken to determine the catalyst content in the ink before printing the ink on a Teflon sheet, in a similar method to the destructive loading test used throughout this study. A small amount of ink was poured into a crucible and then weighed. Knowing the density, it was then possible to determine the volume of ink in the crucible. The ink was then placed in the furnace to burn off all non-metals in the ink. The weight of catalyst per volume of ink was then able to be calculated. In order to test ink transfer from the screen, a test was conducted where a section of Teflon sheet was weighed, a decal was printed on the sheet, and then the sheet was weighed again with the ink on it. Knowing the density of the ink, it was then possible to calculate the volume of ink printed on the Teflon sheet. These new measures were incorporated into the synthesis of later ink batches in order to work toward a better-controlled synthesis process.

Formulation Development

Initial samples were made close to baseline loadings. A destructive test was performed on one of the decals from each formulation, indicating a loading very close (within 3%) to the design intent. Visually, the printed decals appeared to be homogeneous layers with only pinhole voids present. A three-cell stack was built with two ink formulations and a baseline for comparison. The voltage trends observed were stable and lower than the baseline cell. Operating cell potential can be seen in Figure 12 below.

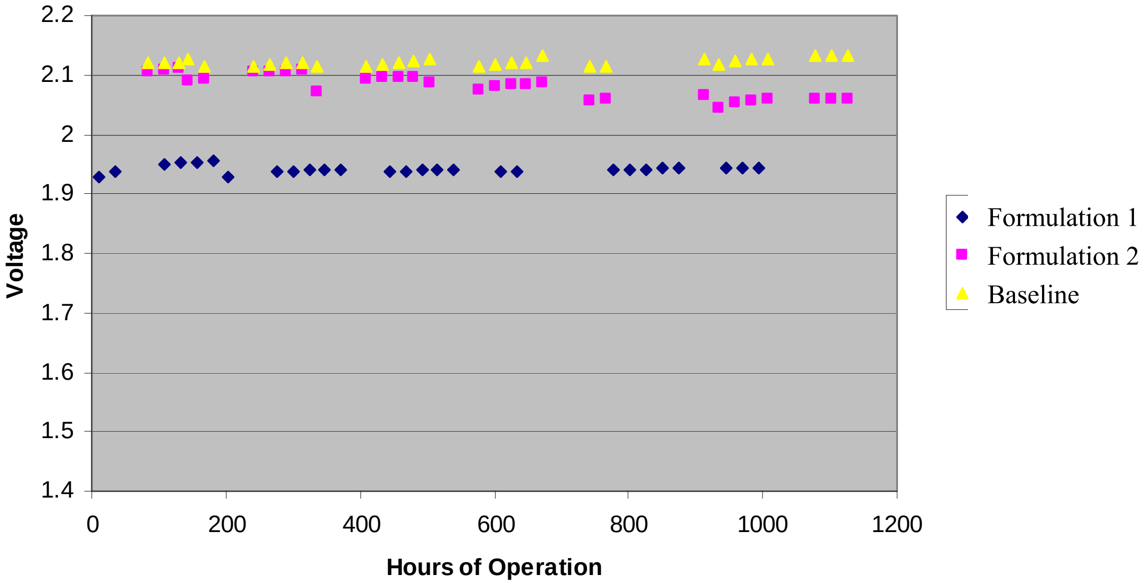

Figure 12: Operating Potential Data for Inked Anode Electrodes, 200 psi, 50°C

One inked formulation held at about 180 mV lower than the baseline, and the other had dropped to about 70 mV below the baseline cell by the end of the testing, displaying a gradual but consistent downward trend throughout the test period. Polarization curves were also generated for this test and are shown in Figure 13 below. The linear response through the range of currents shows the ability of the new catalyst formulation to remain stable at elevated currents. This behavior also serves as context for evaluating electrodes with significantly reduced loadings. As shown in the graph, the ink formulation which performed best in the steady-state trends also showed lower resistance based on the slope of the polarization curve.

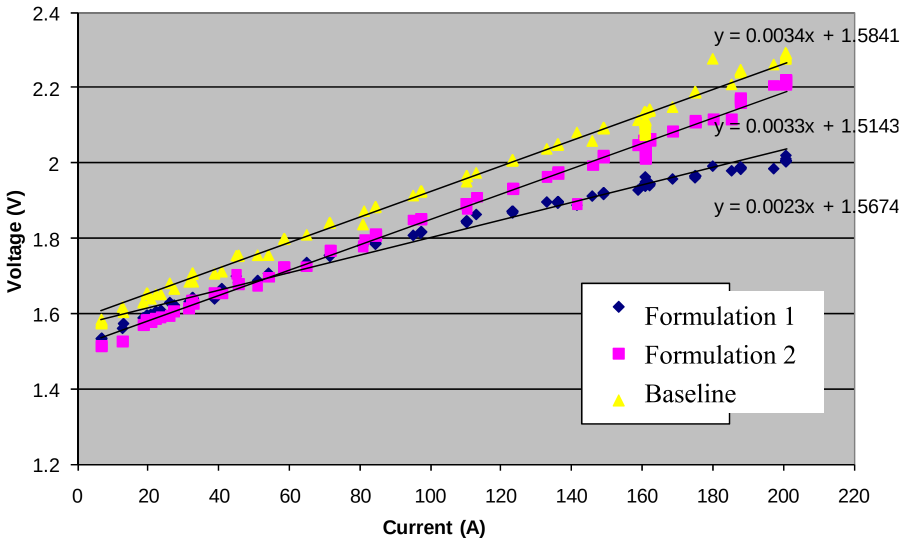

Figure 13: Polarization Curves for Inked Anode Electrodes, 200 psi, 50°C

Before and after in-cell testing, resistance measurements were taken on each of the MEAs. There was clearly an activation of the MEAs upon initiating electrolysis as indicated by large decrease in resistance. The cross-cell resistances for these MEAs had fallen to values in line with a typical production MEA. The in-cell resistances had also dropped, again putting them in the acceptable range for a typical MEA. These results are summarized in Table 6 below.

	Cross-Cell Resistance (mΩ)		In-Cell Resistance, No Pressure (mΩ)		Operating Potential at Test End (V)
Cell	Before	After	Before	After	-
Formulation #1	444%	97%	568%	103%	1.94
Formulation #2	380%	101%	502%	102%	2.06
Baseline	112%	100%	107%	100%	2.13

Table 1: Test Results for Ink Decals and Baseline

Loading Reduction Tests: Phase 1

Having had success in the first attempt at creating an anode ink with acceptable electrochemical performance, the goal for the second round of samples shifted to reducing the catalyst loading to the maximum degree without causing a loss in performance. The test plan for the next set of samples was to fabricate three batches of ink with target loading reductions of 12%, 25%, and 50% vs. the baseline.

The same type of analysis was carried out on this set of ink batches as with the first. The density in each of the three inks was measured to be within 2% of the expected density, suggesting good control over the final compositions. The printed decals, however, displayed bubbles over large portions of the surface, which had not been present in the first set of samples (Figure 14). This result could have been due to the approach used to dilute the catalyst content, which also reduced the proportion of binder and additive in the total ink volume as discussed above.

Figure 14: Printed Ink Decal Showing Bubble Agglomerates

The loading test also yielded very inconsistent results. While the different formulations yielded a reasonable range of loadings for examination, the predicted loadings went in the reverse trend to the targets. Loading results, normalized resistance measurements and operating voltage data can be seen in Table 2 below.

Target Loading Reduction	Actual Loading Reduction	Cross-Cell Resistance (mΩ)		In-Cell Resistance, No Pressure (mΩ)		Operating Potential at Test End (V)
		Before	After	Before	After	-
12%	46%	N/A	116%	375%	1584%	2.081
25%	39%	N/A	109%	907%	146%	2.034
50%	23%	N/A	109%	390%	133%	2.049

Table 2: Test Results for Ink Decals in Second In-Cell Operational Test

Even with the reduced loading, stable performance was achieved through the duration of the test and can be seen in the steady-state trends and polarization curves in Figure 15 and Figure 16, respectively. Cell operating conditions were the same as above as in Figure 12 and Figure 13. All of these samples exhibited lower voltages than the baseline MEA in Figure 12 (2.13 V).

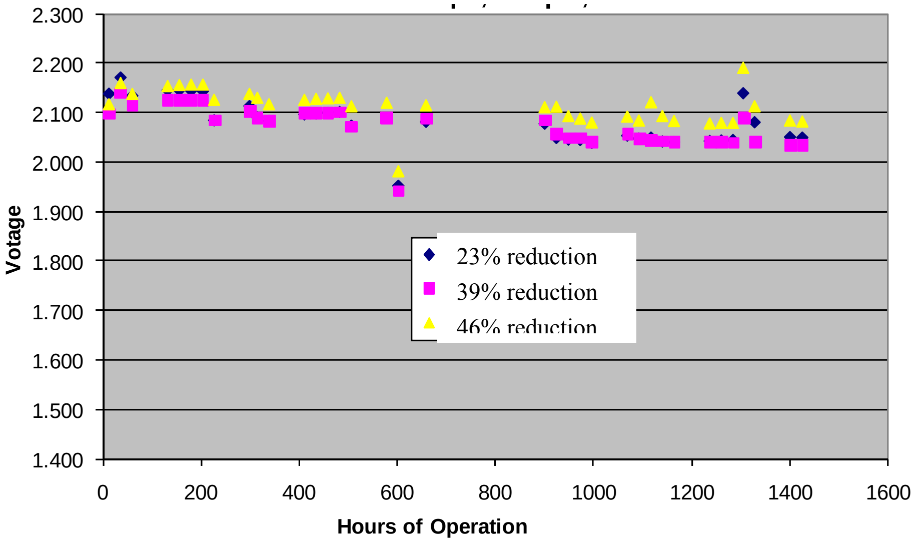

Figure 15: Steady-State Operating Potential Data For Second Ink Test

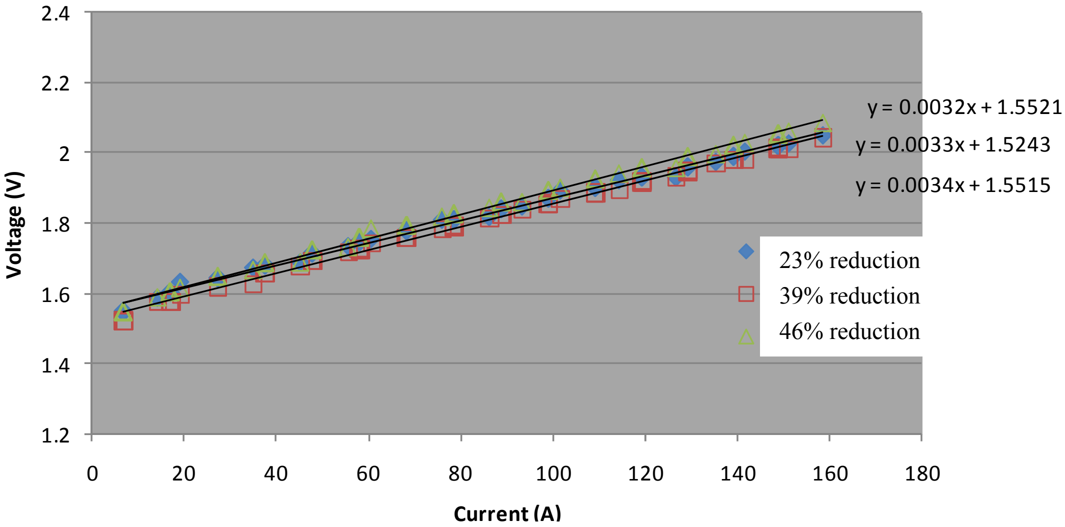

Figure 16: Polarization Curves for Second Ink Test

While the performance was good, the decals not have the expected composition. In addition, the trends were variable, making it impossible to determine a correction factor.

The only improvements seen in the next set were that all of the measured loadings were lower than the target loading, and that the experimental loading figures followed the same order that the target loadings did (Table 3).

Target Loading Reduction	Measured Loading Reduction
0%	45%
20%	60%
37%	63%
55%	64%

Table 3: Test Results for Anode Ink Decals in Third Test

Testing results for the lowest loadings are shown in Figure 17 below, showing an upward trend early in the test, which could be indicative of exceeding the lower limit threshold for catalyst loading. Polarization data is included in Figure 18 showing stability through the range of currents, but the potentials in the higher current ranges are higher than the baseline sample.

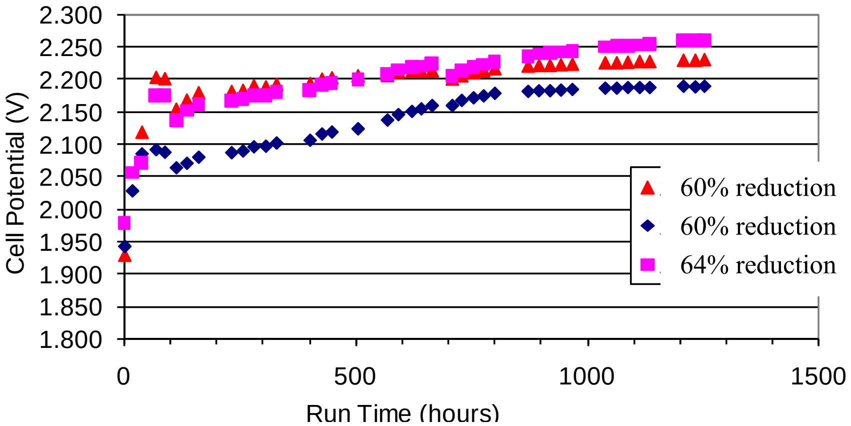

Figure 17: Steady-State Operating Potential Data for Third Test.

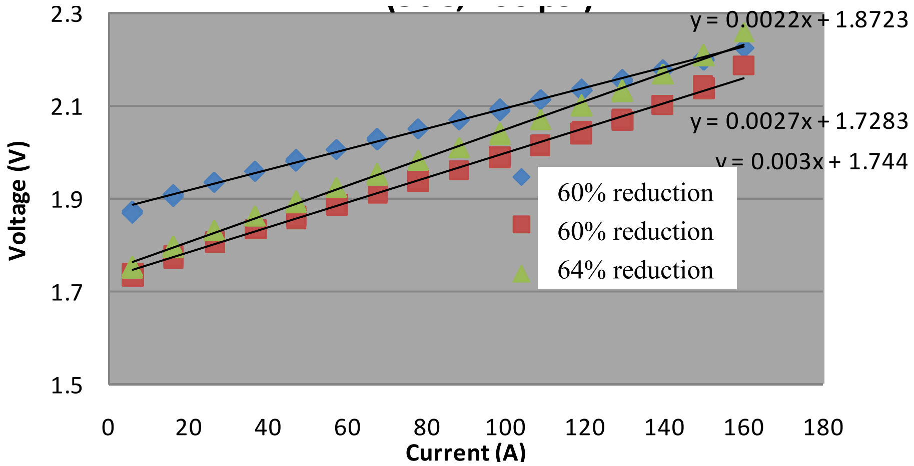

Figure 18: Polarization Curves for Third Test

Loading Reduction Tests: Final Phase

After observing the inconsistent results from the tests described above, it was discovered that while the total density of the ink was close to specification, the catalyst density was low, resulting in catalyst loading in a decal being lower than desired. It is possible that the metal was not held in suspension well enough, since the measured catalyst density was lower than would be expected based on the final overall density. Also as hypothesized, the anode ink formulation does not seem to pass through the screen as freely as the cathode does. A destructive loading test showed that the catalyst loading in a decal printed from this batch of ink was further reduced from expected based on the actual catalyst density. This new data helped to shed light on the reasons for the inconsistencies observed between the ink design and the final product.

The final test in this phase of the program was designed to better define the lower limit of catalyst loading for an anode ink formulation that would provide equivalent performance to Proton's current production anodes. Measured loadings were still considerably lower than target, but in a predictable trend, showing improvement based on the learnings above. Table 4 below shows the loadings and operating potentials associated with these MEAs, while steady-state voltage data can be seen in Figure 19 below.

Measured Loading Reduction	Operating Potential at Test End (V)
40%	2.148
54%	2.170
83%	2.666

Table 4: Test Results for Anode Ink Decals in Final Test

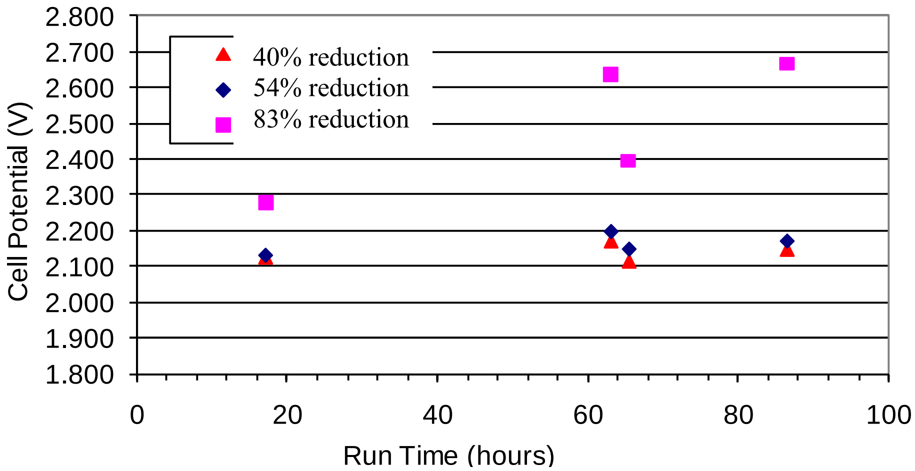

Figure 19: Steady-State Operating Potential Data for Final Test

The initial results clearly indicate an unacceptable potential for the lowest loading cell, while the other two are in an acceptable range and operated at a steady potential over the first 100 hours. Overall this trial is a significant improvement over the previous tests and while it was clear that more work needed to be done to hone the ink synthesis and printing processes, it appears that a step was taken in the right direction with the new mass control method. Based on the promising results obtained in this initial feasibility study, a separate SBIR project was awarded to Proton with a focus on low catalyst loading and high utilization. Continuing work was therefore pursued under that program.

5.2 Task 2.0 Prototype Flow Field Development

Model Validation:

One of the most important issues in CFD modeling and the computational science community in general is how to validate the developed mathematical models. Converged calculations based on the developed models don't always generate physically meaningful results. The validity of the models has to be carefully verified using available relevant experimental results. The ultimate goal of the validation process is to make sure the model can accurately describe the under-study phenomena both quantitatively and qualitatively.

Experimental data in terms of the two-phase flow and species transport of electrolyzers in literature are very scarce. Most of the existing work on electrolyzers had been focused on the material and chemistry areas. Very little work had been done studying the flow and transport phenomena. Experimental data for single and two-phase flow in channels was therefore used validate the model. Fluid flow in channels is of particular interest because the flow channels supply reactant water to and remove generated gaseous bubbles from the porous media. It is crucial for the cell performance that the flow channels can generate uniform flow distribution over the active surface and remove the gaseous bubbles effectively. The flow field is also one of the most expensive components in an electrolyzer, representing a potential area for high cost reduction.

The model accounts for the two-phase flow in anode channels, without considering the coupling of channel and porous media. Specifically, water consumption and oxygen injection boundary conditions are applied at the bottom surface of the channels. It is assumed that the current density distribution in the active surface is uniform and thus the mass flow rates of water consumption and oxygen generation are constant. The geometry and mesh are shown in Figure 20, while simulation parameters are listed in Table 5. The complex flow distribution regions in the inlet and outlet, which have less channel depth than the main parallel channels, are considered in the current calculation.

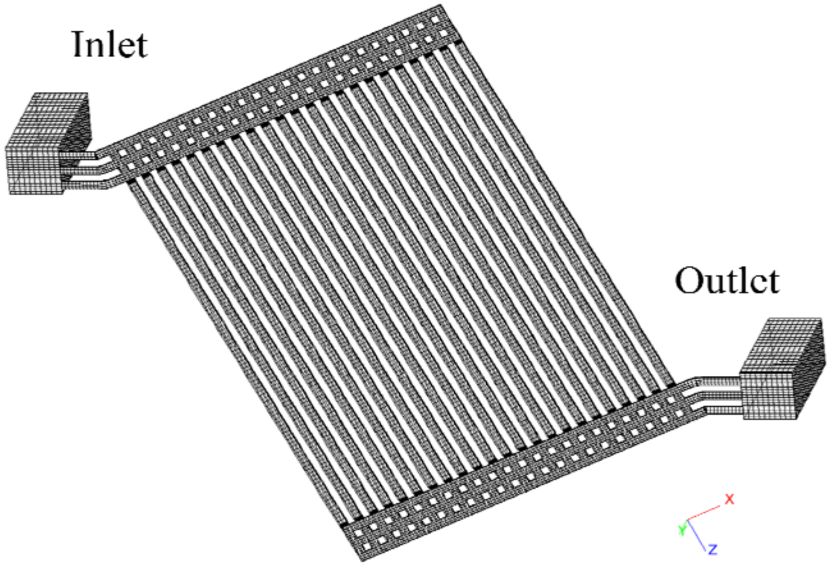

Figure 20: Geometry and Mesh of the Anode Channels

Description	Value
Exchange current density × ratio of reaction surface to catalyst layer volume in anode side (A/m^3)	6.67 × 10^7
Exchange current density × ratio of reaction surface to catalyst layer volume in cathode side (A/m^3)	732.67
Reference hydrogen molar concentration (mol/m^3)	40.876
Reference oxygen molar concentration (mol/m^3)	40.876
HER/OER reaction order	0.5 / 1.0
Electronic conductivity in BP (S/cm)	1.92 × 10^4
Electronic conductivity in GDL (Anode/Cathode) (S/cm)	9.6 × 10^3 / 2.13 × 10^2
Electronic conductivity in catalyst layer (Anode/Cathode) (S/cm)	1.887 × 10^3 / 1.92 × 10^2
Proton conductivity in membrane (S/cm)	0.1
Hydraulic permeability of porous media (m^2)	7.5× 10^{-10}
Hydraulic permeability of membrane (m^2)	5.0× 10^{-20}
Faraday constant (C/mol)	96487
Universal gas constant (J/mol K)	8.314
Surface tension (N/m)	0.0625
Liquid water density (kg/m^3)	972
Liquid water viscosity (N s/m^2)	3.5× 10^{-4}
Flow shape factor *c*	1.127
Thermal conductivity in BP (W/m K)	16.4
Effective thermal conductivity in GDL (Anode/Cathode) (W/m K)	8.2/1.7
Effective thermal conductivity in catalyst layer (Anode/Cathode) (W/m K)	8.2/2.0

Table 5: Simulation Parameters

There were two reasons to perform the single-phase calculations. One is to compare with the experimental results. The other is to get the absolute permeability of the channels which will serve as input parameters for the two-phase calculation. Figure 21 shows the velocity magnitude contour in the channels for the highest flow rate measured.

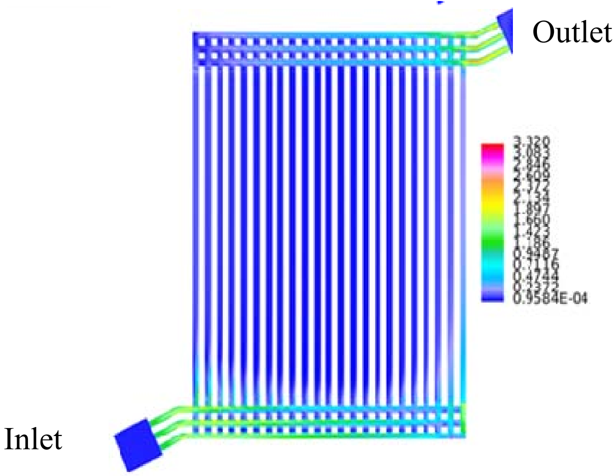

Figure 21: Velocity Magnitude Distributions in Anode Channels (Single-Phase Flow)

The flow accelerates itself when going from the inlet header to the three distribution channels due to the reduction of flow area. As the flow goes through the inlet distribution network, it is gradually extracted into the parallel main channels downstream. The pressure also decreases due to the resistance of the distribution network. Figure 21 illustrates the calculated average axial velocity distribution among the different channels. It can be seen that the average axial velocity in all channels increases with the inlet water flow rate. But the flow distribution among different channels is not uniform. For all inlet water flow rates, the average axial velocity is larger in the channels on the side than the channels in the middle region. The velocity decreases from the channels near the inlet to the channels in the middle because of the pressure loss in the inlet distribution network channels. Figure 23 shows the relative pressure distribution in the anode channels.

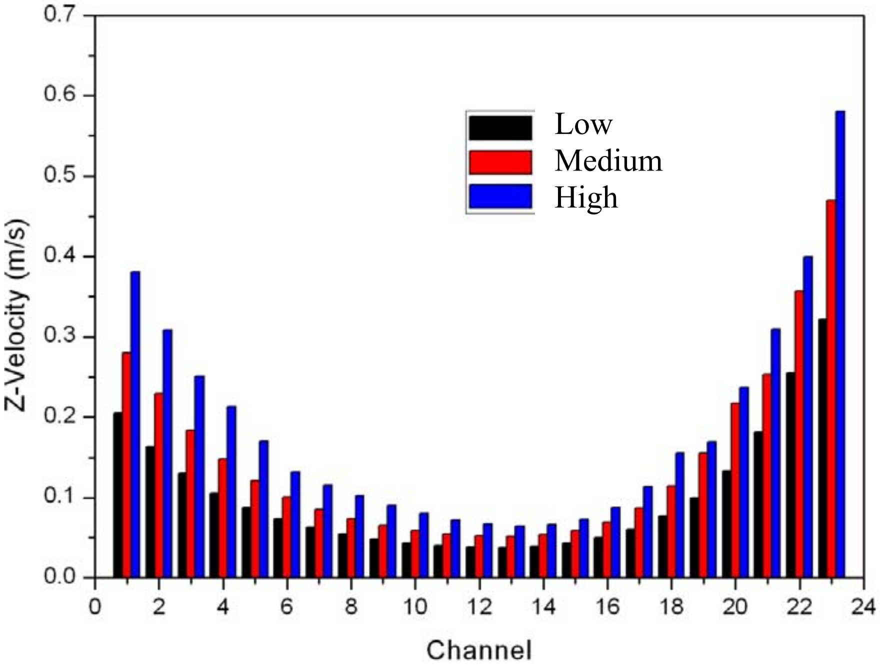

Figure 22: Axial Velocity in Anode Channels vs. Flow Rate

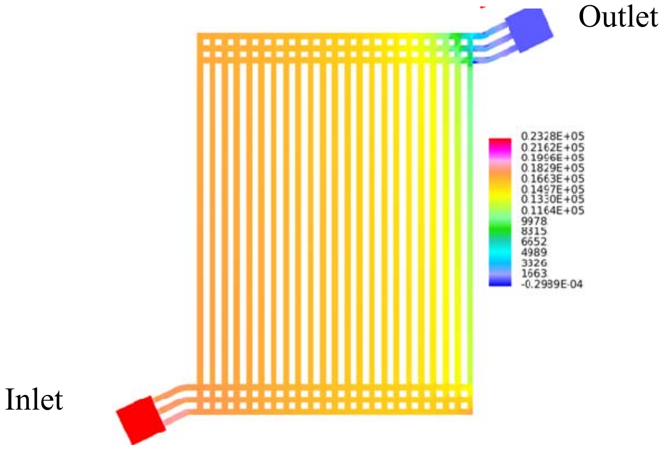

Figure 23: Relative Pressure Distributions in Anode Channels

The oxygen volume fraction in the channels is illustrated in Figure 24. The oxygen volume fraction is defined as one minus the liquid water saturation, which can be obtained from Eqn. 18. An assumption has been made that gaseous water vapor and oxygen share the same amount of volume which is according to the gas law. Figure 24 shows the oxygen volume fraction distribution in the channels viewed from the channel/GDL interface, as well as the oxygen distribution in the channels viewed from the other side.

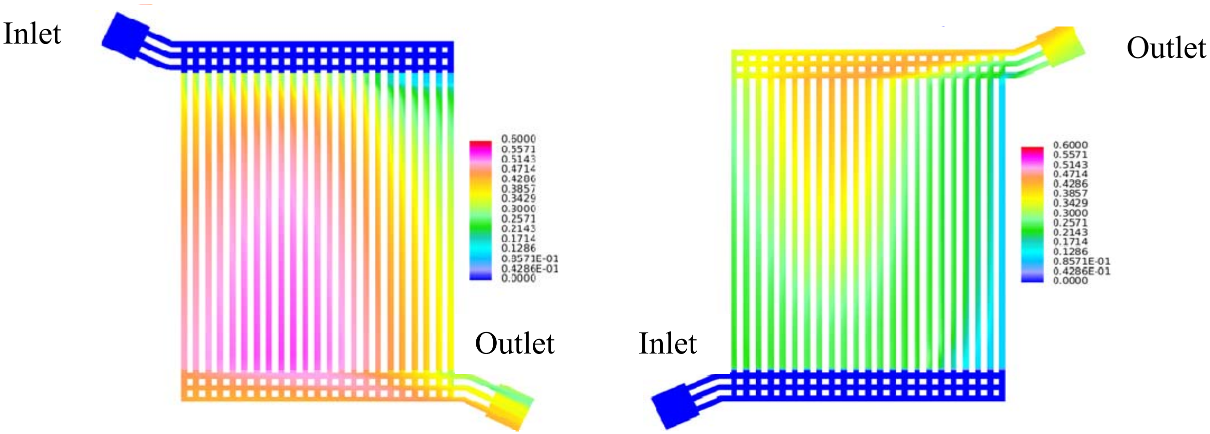

Figure 24: O_2 Volume Fraction Distribution in Anode Channels
(Viewed from GDL/Channel Interface, Left, and Channel Bottom, Right)

Several observations can be made. First, for all cases the oxygen volume fraction increases from the channel inlet to outlet. This is due to the accumulative effect of oxygen injection along the flow direction. Second, the overall average oxygen volume fraction decreases with the inlet water flow rate, which means higher water flow rate is more effective for water removal. Third, the oxygen volume fraction is higher near the channel/GDL interface since oxygen bubbles are transported in the channels mainly by convection rather than diffusion. Finally, non-uniform distribution of oxygen volume fraction among channels can be seen. The volume fraction is lower in those channels on the sides than those in the middle. This can be explained by examining the velocity magnitude distribution in Figure 25. Similar to the single-phase flow, the velocities in the side channels are higher than in the middle channels.

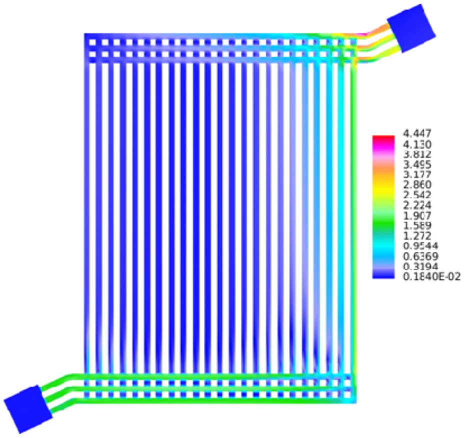

Figure 25: Velocity Magnitude Distributions in Anode Channels (Two-Phase Flow)

The velocity distribution in the main channels at three different along-the-channel locations is shown in Figure 26. The distribution is similar to that of single-phase cases except that the non-uniformity is exaggerated for the two-phase cases. The velocity in the channels near the outlet increases significantly from the channels near the inlet. This is because the pressure drop in the outlet distribution network is much larger than the single-phase cases due to the two-phase flow. This results in higher pressure drop in those main channels that are near the outlet side, which causes the higher velocity.

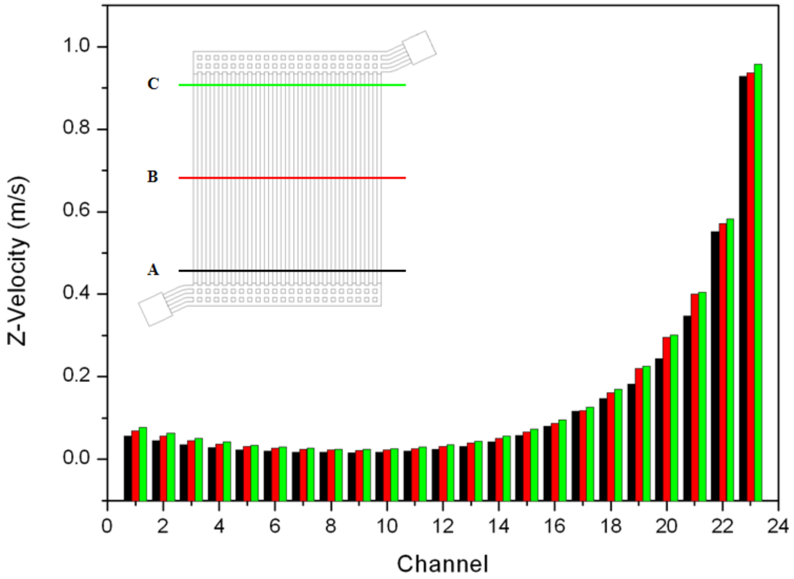

Figure 26: Axial Velocity Distribution in Anode Channels (Two-Phase Flow)

Figure 27 shows the comparison of the current calculations results with available experimental data. It can be seen that the results from the current model matches the single-phase measurements data very well.

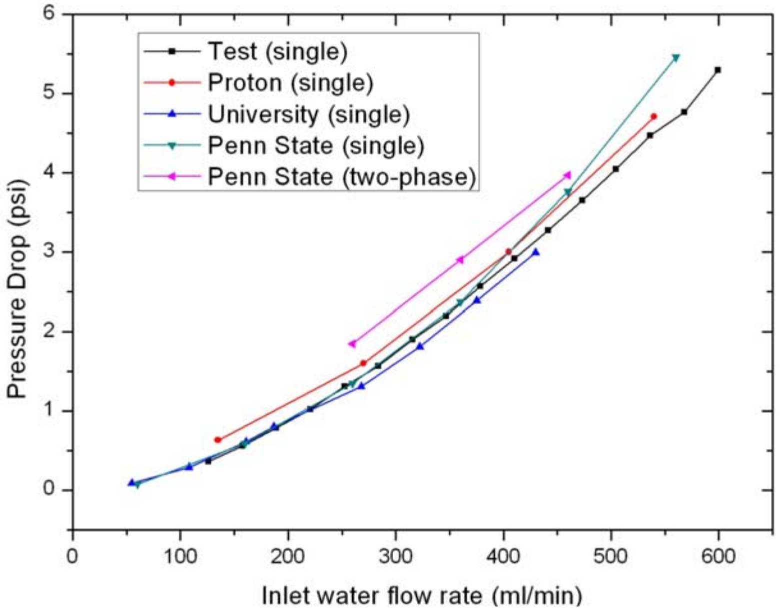

Figure 27: Comparison of Predicted Pressure Drop with Experimental Data

The pressure drop for the two-phase cases is higher than the single-phase cases, which is physically reasonable. Therefore the current two-phase comprehensive electrolyzer model is able to generate physically meaningful and experimentally comparable results. Utilization of the model for parametric study and the round-porous flow field analysis is detailed in the following sections.

Parametric Study using the Comprehensive Model

The power of the present two-phase comprehensive model lies in its ability to treat the entire geometry, including all the components such as flow channels, GDLs, catalyst layers and membranes, as a single calculation domain. The governing equations are the same in each sub-domain and all the interfacial boundary conditions are taken care of automatically. In addition, the current model is cast into the standard CFD form, making it easy to be implemented into commercial CFD packages. The strong meshing power of the commercial software makes the model very suitable for complex geometries.

In order to fully utilize the power of the comprehensive model and study the effect of various parameters on the electrolyzer performance and flow behavior, several multi-channel cases were simulated using the comprehensive model. The geometry is shown in Figure 28. The description of the eight cases is listed in Table 6.

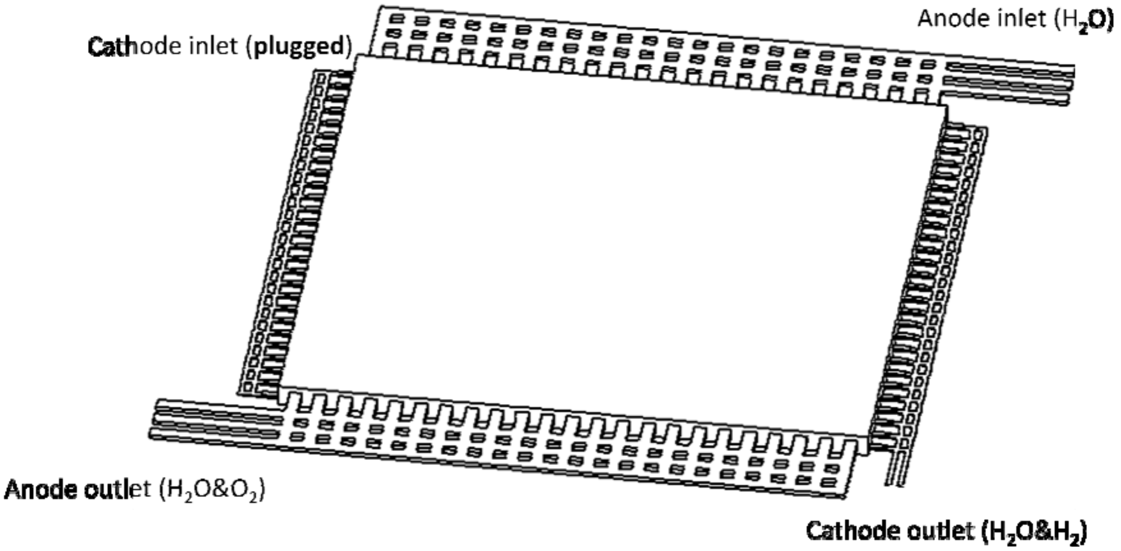

Figure 28: Geometry of the Multi-Channel PEM Electrolyzer Cell

.Case No.	Magnitude of change
1	Baseline
2	½ anode channel width and depth
3	2x anode channel width
4	Without header sections
5	Switch anode inlet and outlet
6	2x GDL thickness
7	30^{o}C inlet
8	80^{o}C inlet

Table 6: Description of the Parametric Study Cases

The following quantities are extracted from the calculations and compared for different cases to examine the parameter effect:

- Cell voltage
- Pressure drop in anode channels
- Average oxygen volume fraction in anode GDL
- Average oxygen volume fraction in anode channels
- Standard deviation of current density in the membrane
- Distribution of pressure, species volume fraction, current density and temperature

Figure 29 shows the predicted cell voltages for the eight cases. Although the coupled solid state potential equation and electrolyte potential equation are solved to get the detailed potential distribution in three-dimensional space, the contribution of various parameters to the cell voltage can be simply approximated by the following lumped model:

$$E_{cell} = E_0 + \eta_{OER} + \eta_{HER} + \eta_{ohm,e^-} + \eta_{ohm,H^+} + \eta_{\text{mass}} \tag{34}$$

where E_0 is the equilibrium cell potential which is a strong function of cell temperature and pressure. The various η terms in Eqn. (34) account for the various over-potentials caused by OER/HER reactions, electrical resistance due to electron and proton transport, and mass transfer loss. For normal electrolyzer operation conditions, mass transfer loss is rarely observed. Thus its contribution to the cell voltage can be neglected here. The activation losses due to HER and ohmic losses due to the electron transport in backing layers are also much smaller than the other terms in Eqn. (34). Therefore the cell voltage mainly depends on the equilibrium potential, OER activation losses, which are highly influenced by temperature, and ohmic losses due to proton transport, which are a strong function of membrane thickness and water content in the membrane.

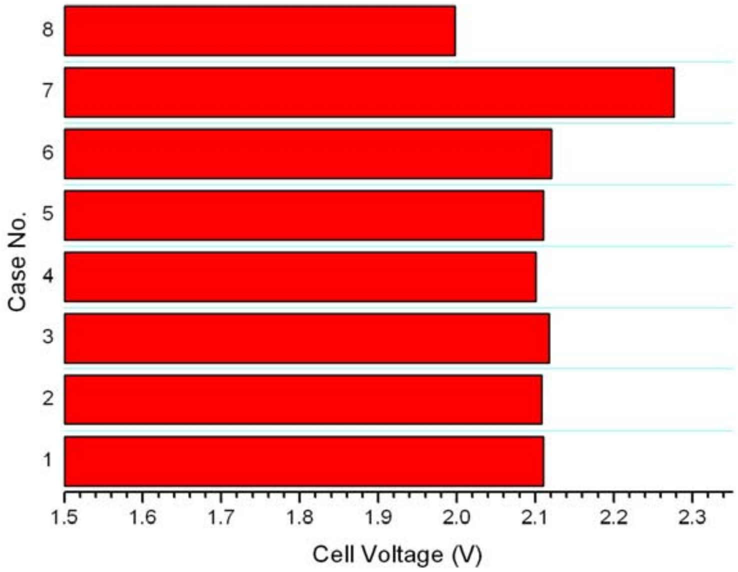

Figure 29: Predicted Cell Voltages (Case 1-8)

Higher cell temperature gives better cell performance and vice versa. This is because the equilibrium potential decreases with temperature and the OER activation over-potential also decreases with temperature due to the increased electrochemical reaction activity at higher temperature. However, the other cases, i.e. case 1 to case 6 show little difference in cell voltage. This is because the current inlet water flow rate is sufficient enough to avoid rising mass transfer loss for all of these cases. The equivalent stoichiometry number of the inlet flow is on the order of hundreds, which means that the flow field configuration, i.e. the dimensions of the flow channels and porous GDLs, won't have too much influence on the cell voltage. It is believed that they will have much greater impact on the cell performance at low stoichiometry numbers. However, the PEM electrolyzers rarely operate under low inlet stoichiometry since the inlet water not only feeds the OER reaction but also removes heat generation by the electrochemical reactions and joule heating.

Although the flow field may not have too much impact on the cell voltage, it does have substantial influence on the pressure drop and species distribution. One of the issues of the electrolyzer design is that inlet water with very high stoichiometry number has to be utilized to avoid mass transfer loss and cool the cell. The problem is that high flow rate can cause large pressure drop, which leads to a high parasitic power loss. And the pressure drop is even larger for two-phase flow, as discussed in the previous section. Thus it is necessary to better design the flow field to minimize the pressure drop.

Figure 30 shows the anode channel pressure drop for the eight cases. The pressure drop is significantly smaller for case 4, in which part of the channels are removed in the inlet and outlet distribution network. This verifies that the header sections induce the majority of the pressure drop for the other cases.

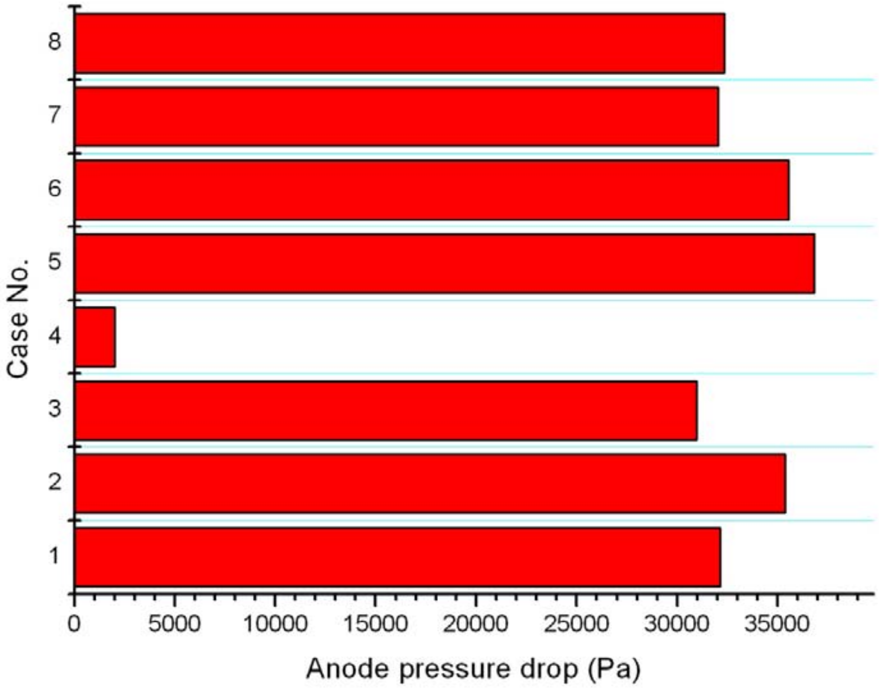

Figure 30: Predicted Anode Pressure Drop (Case 1-8)

It is also shown that the case with 2x channel width has the second smallest pressure drop. This is because that the two-phase mixture velocity is lower in the wider channel, and the number of the wider channels is only half of the baseline case. However, the down side of the wider and fewer channels is that the current density distribution is less uniform than the other cases, as shown in Figure 32, leading to inferior cell performance. Therefore, to minimize the pressure drop it is desired to have wider channels and fewer channel numbers, but many smaller channels would be helpful to the species distribution, leading to uniform current density in the membrane.

Figure 31 shows the average oxygen volume fraction in the anode GDL and channels. Generally speaking, the GDLs have higher oxygen volume fraction than the channels. This is obvious since the oxygen is generated in the catalyst layers and transports through GDLs to the channels, where it is carried away by the flow water. For all the calculated cases, the variation of the oxygen volume fraction in both GDLs and channels is not very significant. This is also because of the large stoichiometry number of the inlet water flow.

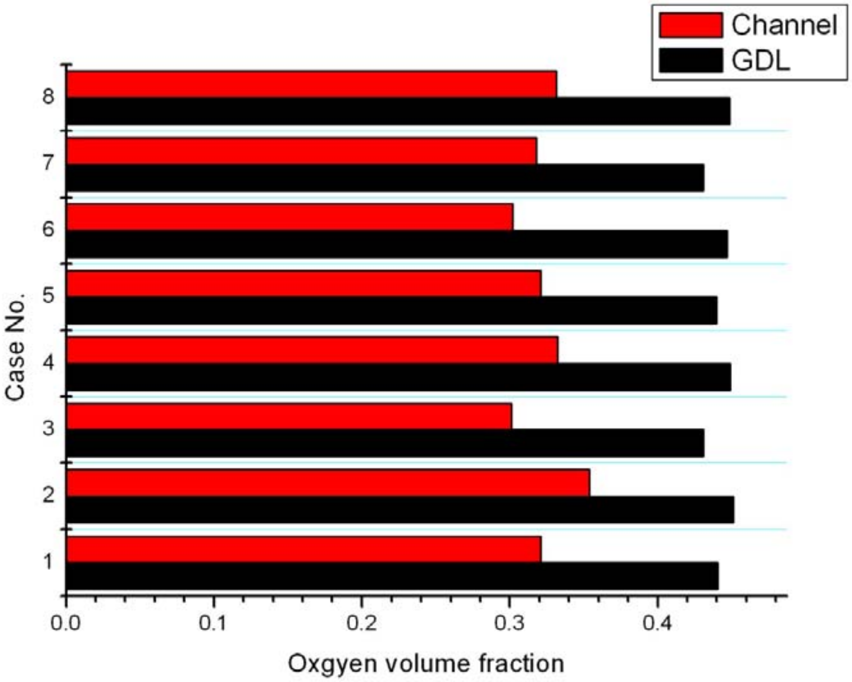

Figure 31: O_2 Volume Fraction in Anode Channels and GDL (Case 1-8)

In order to analyze the non-uniformity of the current density in the membrane, we calculate the standard deviation of the current density data in the membrane. The standard deviation is defined as:

$$\sigma = \sqrt{\frac{1}{N}\left[\sum_{i=1}^{N}(x_i-\mu)^2\right]} \tag{35}$$

where x_i s are the calculated current density data and μ is their mean value. The smaller the standard deviation the more uniform the current density distribution is and vice versa. Figure 32 displays the standard deviation for all eight cases. It can be seen that the case without the header distribution network has the smallest standard deviation, meaning most uniform current density distribution. The largest standard deviation occurs in the case with 2x channel width and fewer channel numbers.

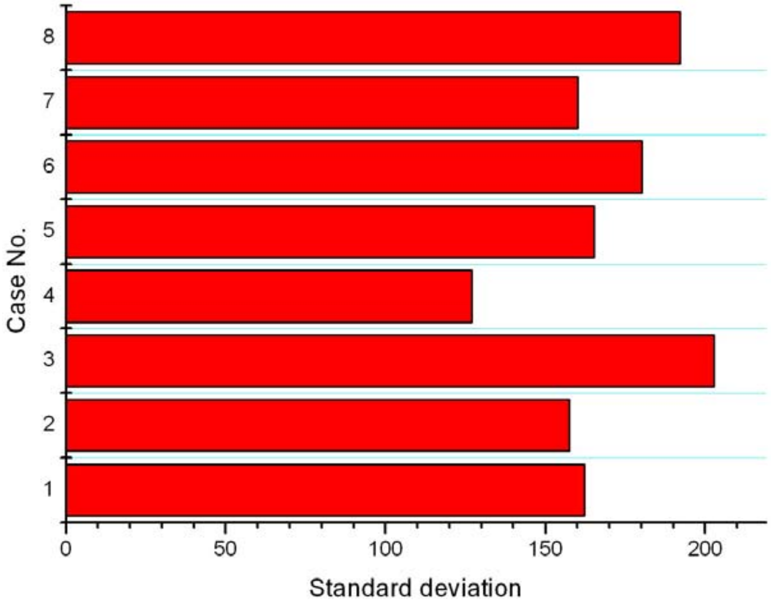

Figure 32: Standard Deviation of the Current Density in Membrane (Case 1-8)

Three cases, case 1, case 3 and case 4, are chosen for more detailed quantity analysis. Figure 33 to Figure 35 show the pressure distribution in anode channels. It can be seen that the pressure drops diagonally from inlet to outlet for case 1 and case 3. For case 4, where the header sections don't exist, the pressure drop from each channel is more or less the same.

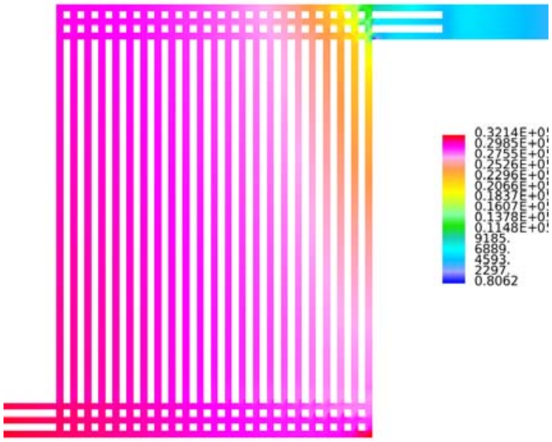

Figure 33: Relative Pressure Distribution in Anode Channels (Case 1)

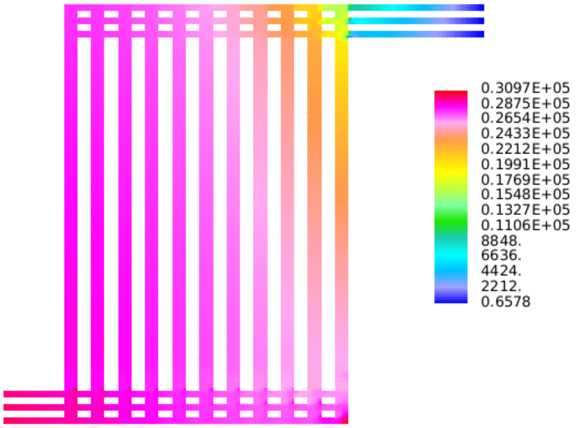

Figure 34: Relative Pressure Distribution in Anode Channels (Case 3)

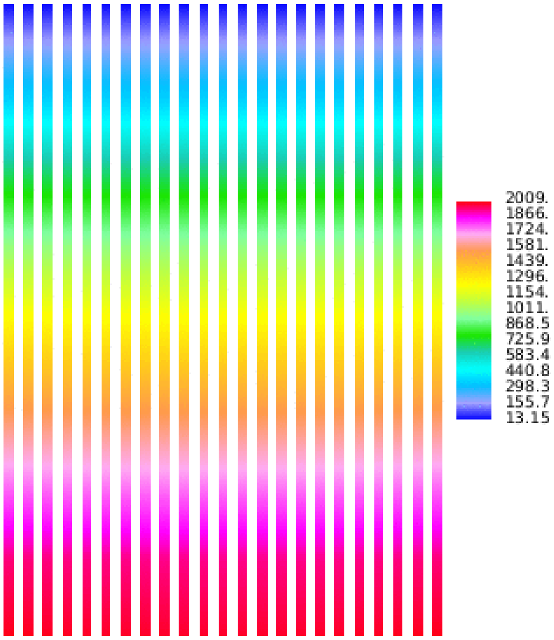

Figure 35: Relative Pressure Distribution in Anode Channels (Case 4)

Figure 36 to Figure 38 display the oxygen volume fraction distribution in the anode channels. It can be seen that the distribution is similar to the channel modeling results during the validation process in the previous section.

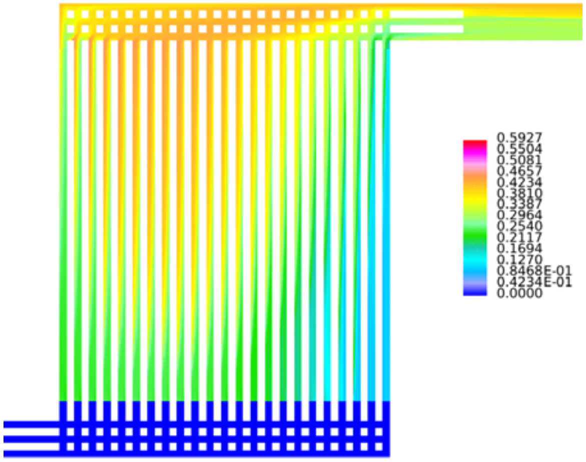

Figure 36: O_2 Volume Fraction in Anode Channels (Case 1)

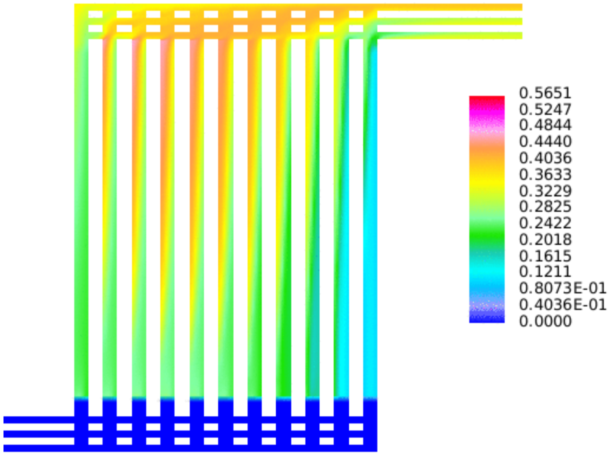

Figure 37: O_2 Volume Fraction in Anode Channels (Case 3)

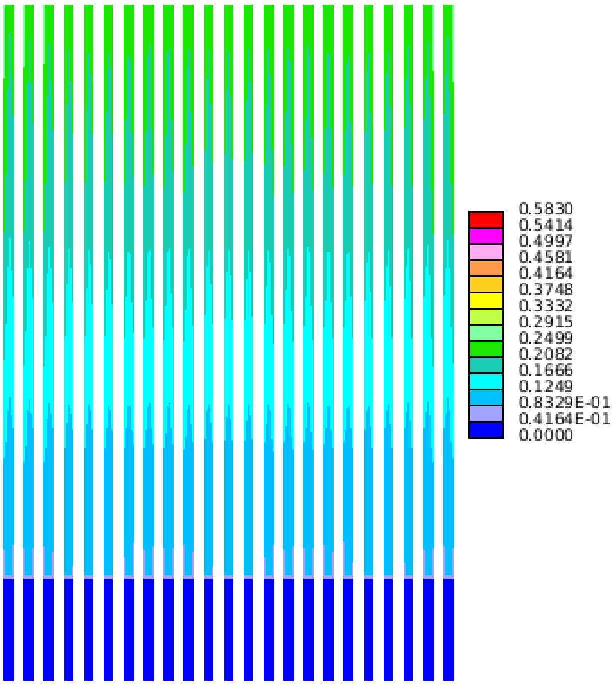

Figure 38: O_2 Volume Fraction in Anode Channels (Case 4)

The oxygen volume fraction in the anode GDL is shown in Figure 39 to Figure 41. Case 4 displays the most uniform distribution of the oxygen volume fraction. Each of its channels have a similar distribution pattern. The amount of oxygen is less in the region in contact with the bipolar plate and more in the region under the channels. This is reasonable since oxygen generated under the channel can be more easily carried away by the channel flow. Case 1 and Case 3, however, show less uniform oxygen distribution. In general, the oxygen is higher in the upper left and smaller in the lower right. The oxygen also tends to accumulate in left and right edges of the cell for all cases. It can then be concluded that the flow configuration without header sections and with more channel numbers would be helpful for uniform oxygen distribution.

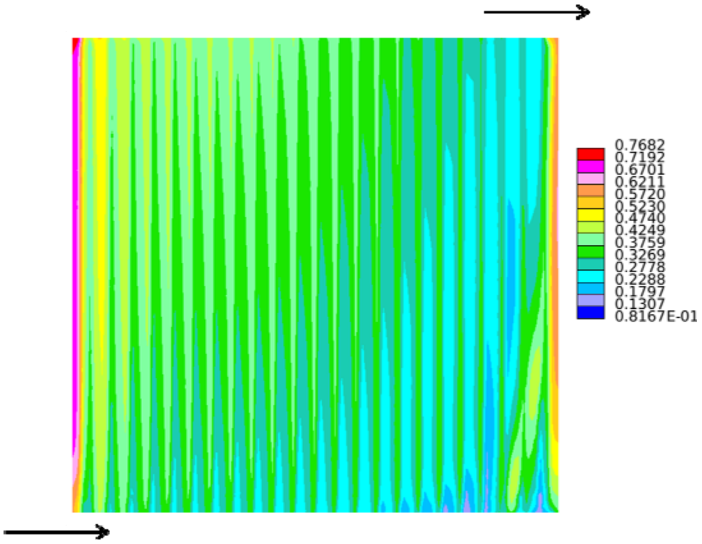

Figure 39: O_2 Volume Fraction in Anode GDL (Case 1)

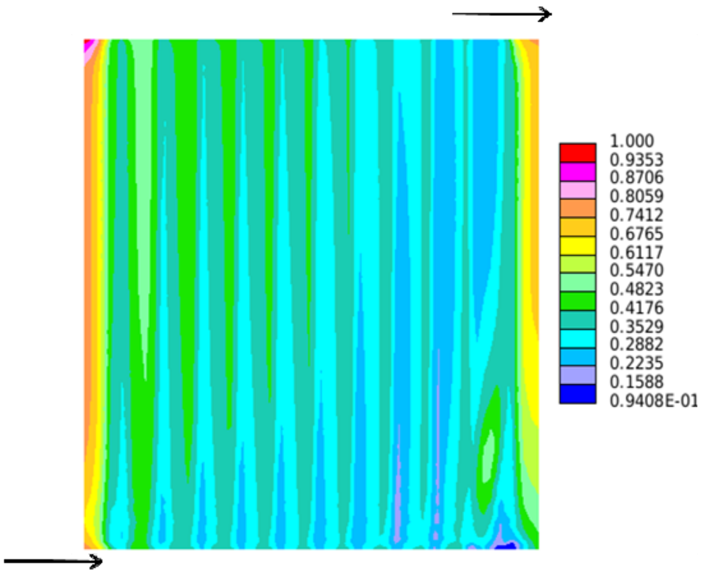

Figure 40: O_2 Volume Fraction in Anode GDL (Case 3)

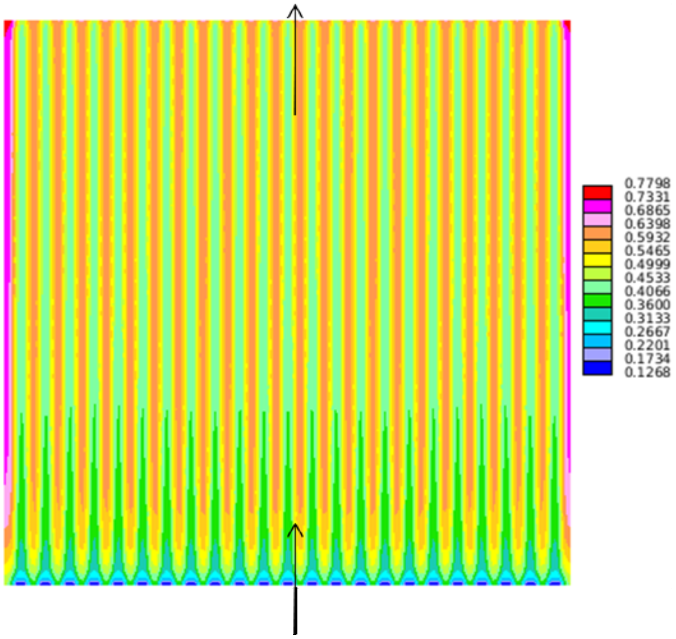

Figure 41: O_2 Volume Fraction in GDL Channels (Case 4)

The current density distribution for the three cases is presented in Figure 42 to Figure 44. As illustrated in the figure of standard deviation before, the current density distribution in Case 4 is more uniform than the other two cases. One factor that affects the current density distribution is the water transport in the porous media. It can be seen from Figure 42 to Figure 44 that the current density is higher in those regions that are under the flow channels than those regions under the bipolar plate land. The higher oxygen volume fraction under the land area will decrease the electrochemical reaction activity, leading to smaller current density. The area under the channel, however, has the best feed of water and removal of generated oxygen. Thus the current density is higher in those regions.

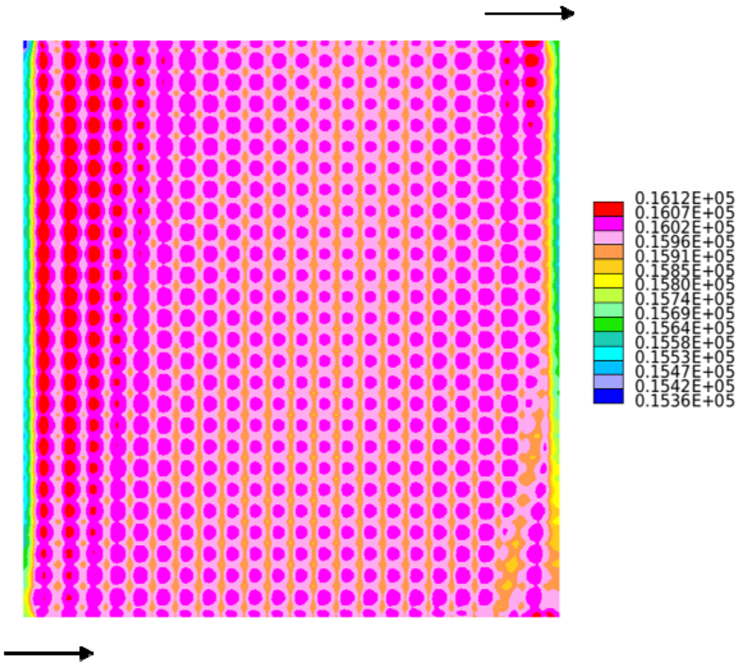

Figure 42: Current Density Distribution in the Membrane (Case 1)

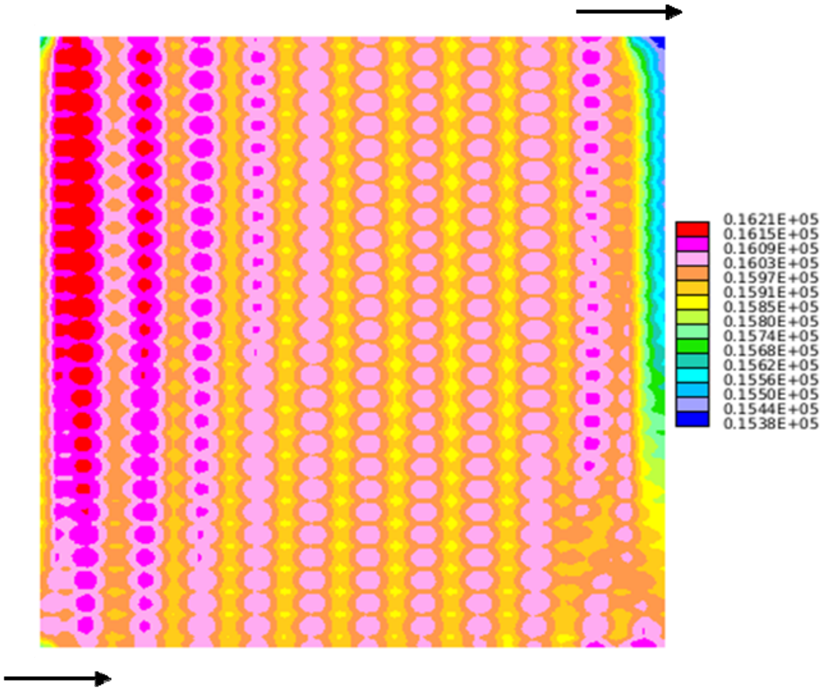

Figure 43: Current Density Distribution in the Membrane (Case 3)

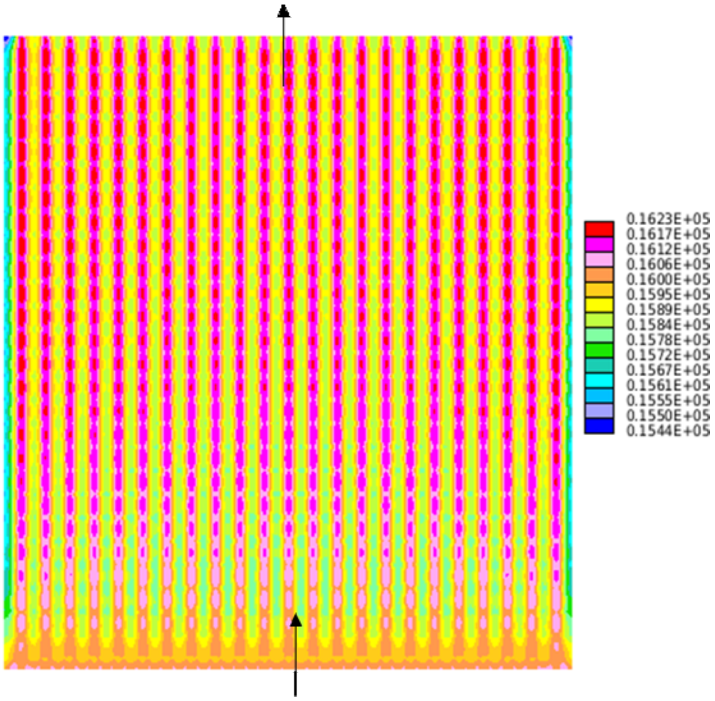

Figure 44: Current Density Distribution in the Membrane (Case 4)

For Case 1 and Case 3, the current density is higher in the upper left region, where the temperature is the highest, as shown in Figure 45 and Figure 46. Therefore, temperature also has a great influence on the current density distribution.

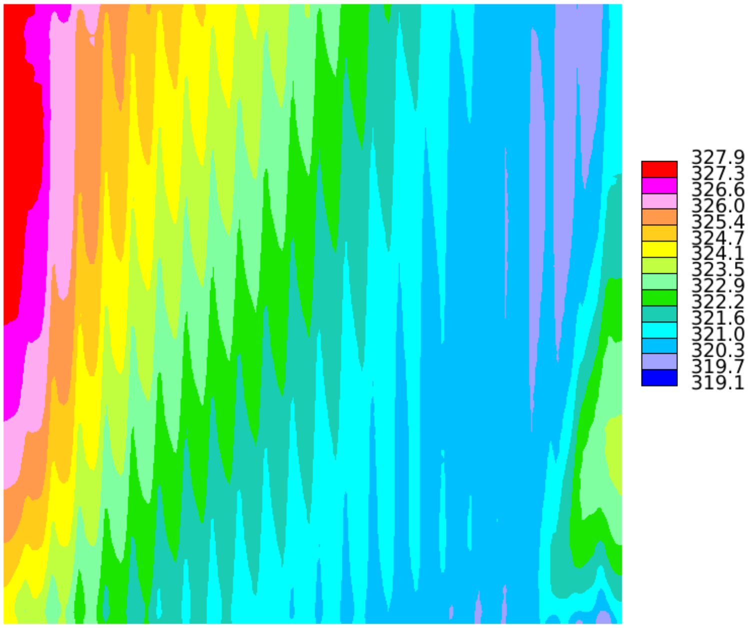

Figure 45: Temperature Distribution in the Membrane (Case 1)

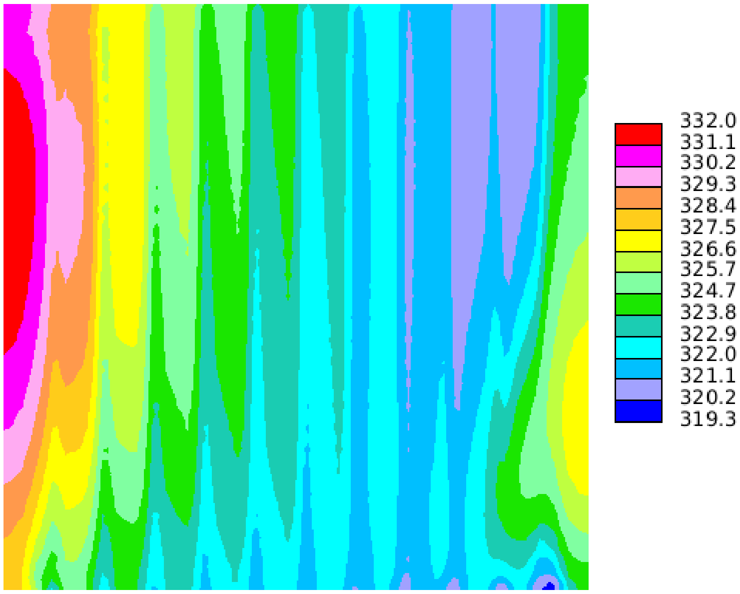

Figure 46: Temperature Distribution in the Membrane (Case 3)

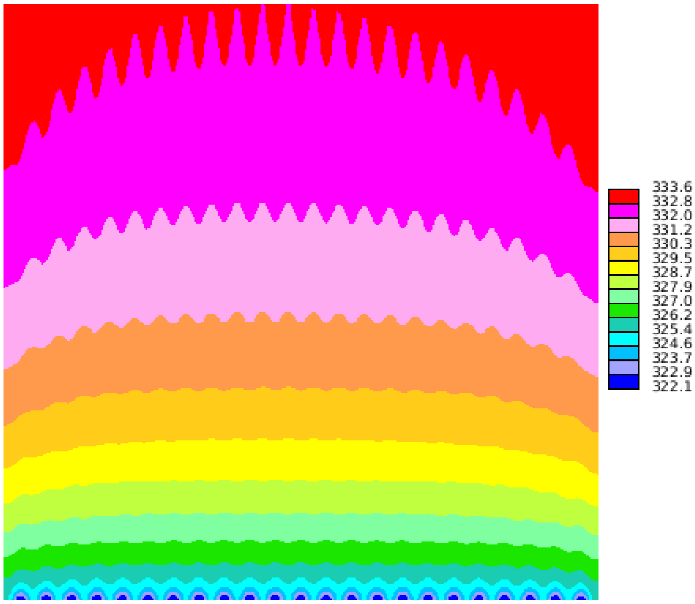

Figure 47: Temperature Distribution in the Membrane (Case 4)

Modeling of the Round-Porous Flow Field

Figure 48 shows the geometry and CFD mesh of a round-porous flow field for a PEM electrolyzer. Due to the complexity of the geometry, unstructured polyhedral mesh is used for the calculation. It is assumed that the round part of the flow field is filled with isotropic porous media with uniform permeability. The permeability cannot be determined analytically and must be obtained from experimental data or from running single-phase flow calculation on the geometry. Therefore, single-phase water flow is considered to determine the permeability at first. Darcy's law is used for the momentum equation in the porous flow field instead of Navair-Stokes equation:

$$\rho\vec{u} = -\frac{K}{\nu}\nabla p \tag{36}$$

and the permeability K can be determined as:

$$K = \frac{\rho\nu}{\left(\alpha\left|\vec{u}\right| + \beta\right)} \tag{37}$$

where α and β are the parameters that need to be calibrated. α and β can be obtained by running calculations on their various values and compared with the experimental data.

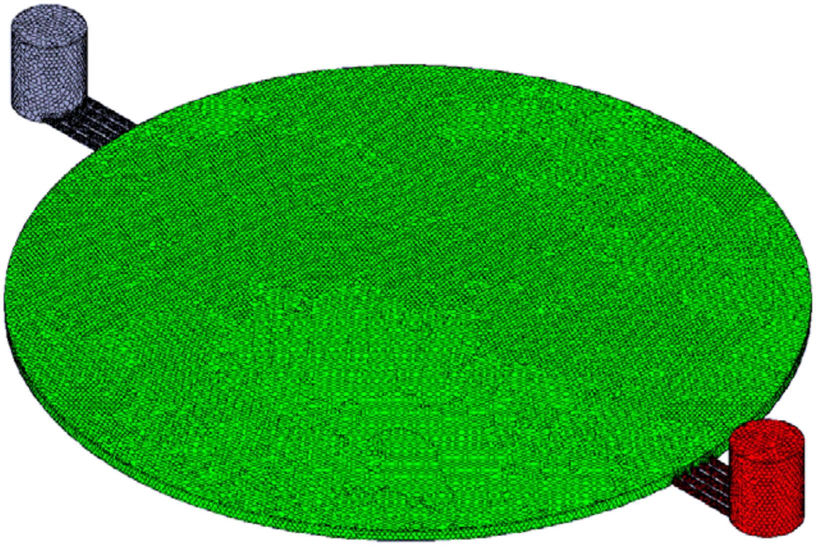

Figure 48: Geometry and Mesh of the Porous Flow Field

Figure 49 shows the comparison of simulation result with experimental data for the single-phase modeling on the round-porous flow field. The α and β are chosen to be 3.53290 10^6 and 4.144300 10^5, respectively. It can be also observed in Figure 49 that calculations on the chosen parameters match the experimental data well. The pressure drop versus flow rate variation has some non-linear effect due to the presence of the α term in the equation (37). The permeability of the geometry is not a constant but deceases with velocity. This has the effect of increasing the predicted pressure drop at high flow rate cases.

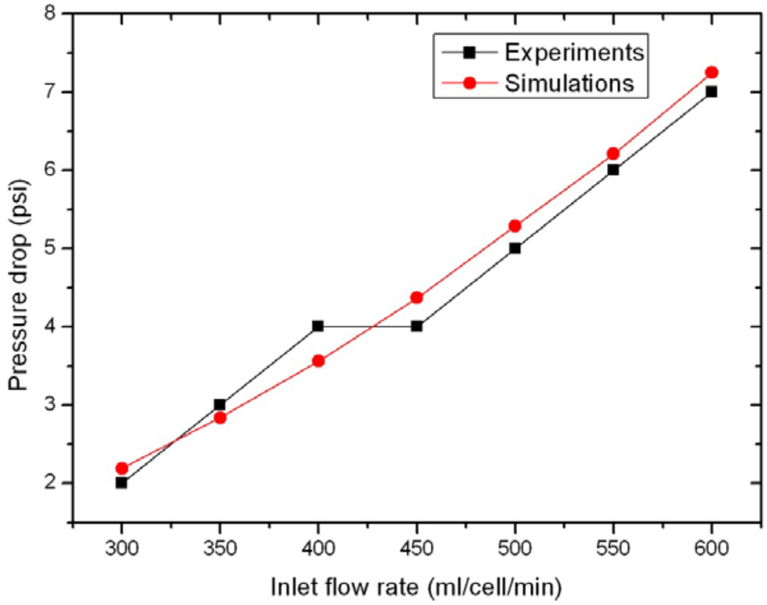

Figure 49: Pressure Drop (Single-Phase Flow)

The calibrated parameters are used for the two-phase flow calculations. At the GDL/channel interface, both oxygen bubble injection and water consumption fluxes are considered. The magnitudes of the fluxes are proportional to the running current. It should be noted that the water consumption flux accounts for both the water consumption due to the OER reaction and also the water flux due to the electro-osmotic drag effect. Figure 50 shows the calculated pressure drop in comparison with experimental data. It can be observed from Figure 50 that the pressure drop of the two-phase flow is generally larger than the single-phase flow. The increase of the pressure drop with inlet flow rate is not linear and is smaller than it should have been if it varies linearly with the inlet water flow rate. This is because that as inlet water flow rate increases, there will be less oxygen bubbles in the flow causing a relative decrease of the pressure drop.

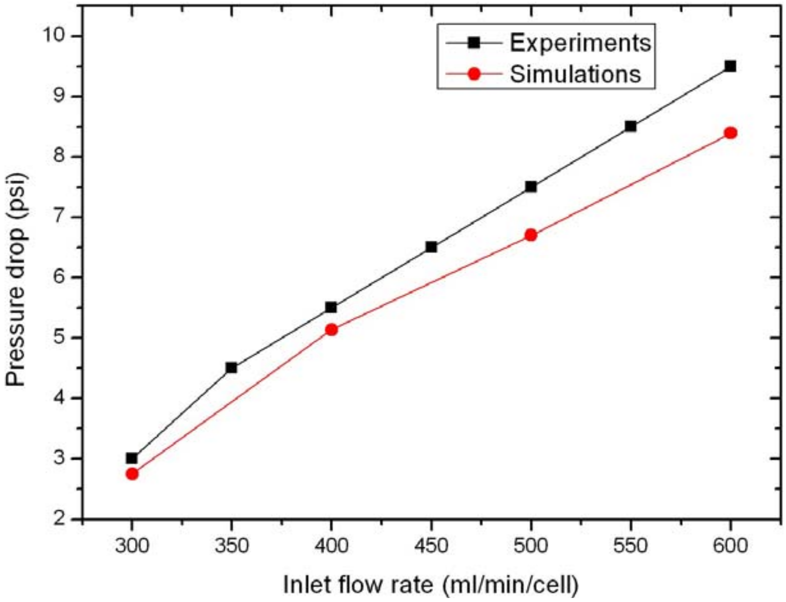

Figure 50: Pressure Drop (Two-Phase Flow)

Figure 51 shows the oxygen volume fraction distribution in the porous flow field. An interesting oxygen species distribution pattern can be observed. Generally speaking, the oxygen volume fraction increases in the round porous media from the inlet to the outlet due to the water consumption and oxygen injection at the GDL/channel interface. The average oxygen volume fraction decreases with the inlet water flow rate as similar to the bipolar plate channel cases before.

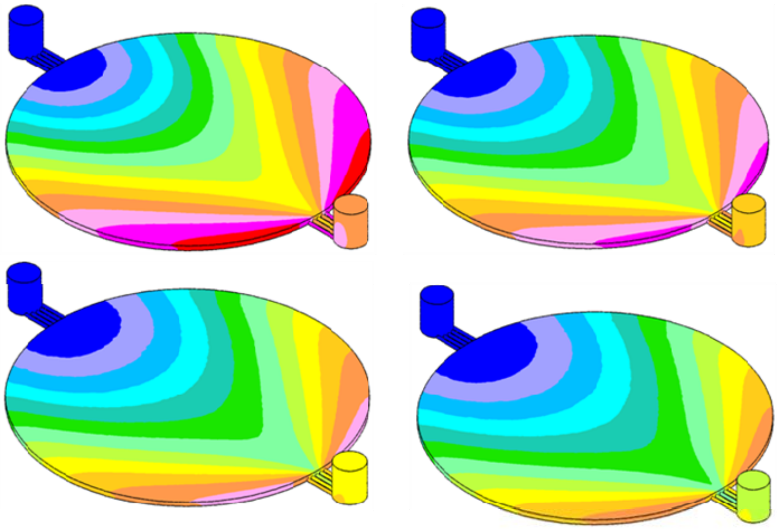

Figure 51: O_2 Volume Fraction Distribution, Low to High Flow Fate

It should also be noted that the oxygen distribution in the round porous media is not uniform. There is more oxygen in the near edge region than in the middle region. This is due to the fact that the two-phase flow velocity is higher in the center than that near the edge, which can be seen in Figure 52.

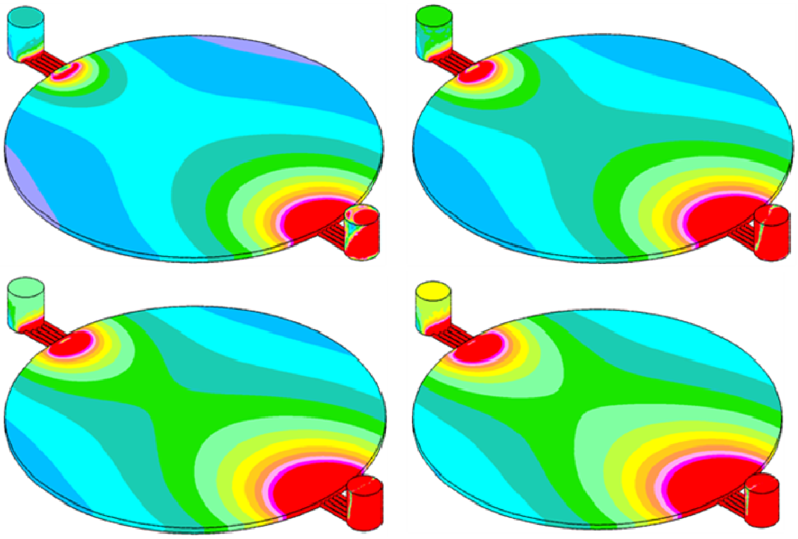

Figure 52: Velocity Magnitude Distribution

The smaller velocity near the flow field edge is due to the lower pressure gradient compared with that in the middle area. The pressure gradient is the driving force for the flow, which is proportional to the flow velocity. The relatively low velocity near the edge causes the oxygen bubble accumulates very quickly along the edge from the inlet to the outlet, especially for small inlet flow rate cases (e.g. 300 ml/min). Therefore there is room for improving the current flow field design, probably by dividing the flow field into several sub-domains, which may increase the manufacturing difficulty.

These models and results were utilized and considered in the design of the bipolar assemblies throughout the course of the project. As discussed in the approach section, the initial effort focused on material changes in the round cell format.

Flow Field Design and Fabrication

This portion of the project centered on the design and incorporation of a new cathode flow field into the cell assembly. After repeating the process steps in the approach several times with various configurations, two plausible options were identified involving two different flow field and gasket options. Pressure films in Figure 53 and Figure 54 indicated that active area pressure was uniform and close to the desired values. Cross- cell resistance readings were also within specification. Neither configuration showed any sign of overboard leaking up to 823 psig during proof pressure testing. It should be noted that subsequent testing at the 3-cell level revealed that in order to seal to proof pressure, it was necessary to increase endplate load for configuration 1. Configuration 2 enabled an endplate load within 5% of the legacy cell design at the 34-cell level.

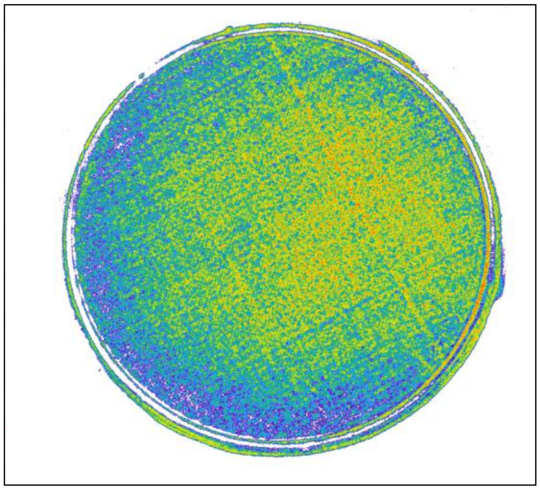

Figure 53: Pressure Film Results for Configuration 1

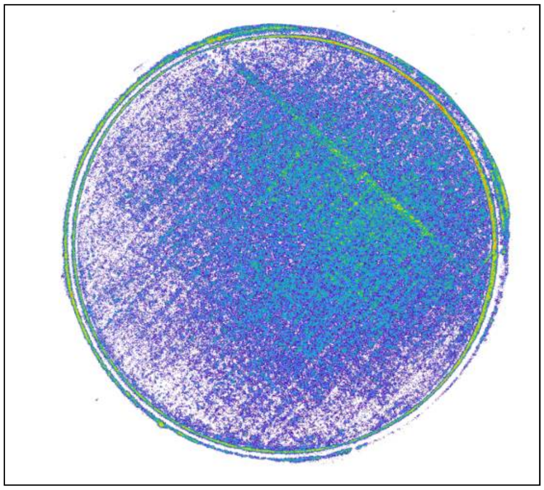

Figure 54: Pressure Film Results for Configuration 2

In addition to the balanced pressure hydrostatics pressure test, a decision was made to perform an unbalanced submersion leak test with pressurized nitrogen on configuration 1. This option was considered more prone to overboard leaks than configuration 2. This test was intended to present the cell design with a smaller fluid media and possibly reveal leak paths which may be taken by hydrogen. The escapement of gas would be observed as bubbles issuing from the cell stack assembly. Unless the test is run for a long period of time, it does not guarantee that gas bubbles are not escaping from the active area of the cell into the volumes around each bolt. A separate cell stack was assembled specifically for this test because once a cell stack has been submerged, there is a possibility that water may be retained in the perimeter of the cells potentially allowing a short path between separators. It is also recognized that during the submersion test, metal ions from other components in the stack may be absorbed by the perimeter of the MEAs and result in contamination.

The stack was built, heat soaked, subjected to Proton's ATP , and proofed to 650 psig using the balanced hydrostatic pressure test procedure. The next step was to plumb a regulated supply of nitrogen to one of the hydrogen ports. The oxygen ports were not drained in an effort make any gas leaks more immediately apparent. The assembly was then submerged in the tank of DI water and gradually brought up to 650 psig. At that time, the isolation valve was closed and the contained pressure was monitored with a gauge plumbed between the cell stack and isolation valve. If the isolation valve was not closed, the presence of any leak into the bolt hole columns could go unnoticed because of the pressure regulator's ability to regulate pressure. Two consecutive five-minute trials were conducted. During these trials pressure decayed only 15 psig and no bubbles were observed. As with the hydrostatic pressure test, it assumed that some decay will always be present as a result of creep in the cell components.

A decision was made to build, ATP, and operate 3-cell verification stacks of both configurations for comparison purposes. The intention was to compare voltage trend data for the first 200 to 500 hours. Despite its lower active area pressure, configuration 2 was considered more desirable because it would not require changing the frame gasket or significantly increasing endplate load. If the performance was significantly better for the configuration 1, then the implementation of the required frame gasket and embodiment hardware changes would be justified. Cell stacks were assembled, ATP'd, and proof pressure tested. Both stacks passed all acceptance criteria. Once again, a balanced pressure hydrostatic proof pressure test was performed for each of the 3-cell stacks. Typically, it is more challenging to achieve proof pressure sealing as the number of cells in series increases. This was evident during testing of configuration 1 when it became necessary to increase endplate load. The results of the proof pressure tests for both options are shown in Table 7 below.

RND1014402 Configuration 1			
P1 (psig)	P2 (psig)	dP (psig)	Result
250	N/A	< 5	P
375	357	18	P
455	437	18	P
503	490	13	P
555	549	6	P
606	599	7	P
652	645	7	P

RND1018801 Configuration 2			
P1 (psig)	P2 (psig)	dP (psig)	Result
245	228	17	P
355	336	19	P
450	430	20	P
555	534	21	P
555	547	8	P
600	587	13	P
657	653	4	P

Table 7: Verification Stack Proof Pressure Test Data

Electrochemical Testing
Each of the 3-cell stacks were placed on R&D test stands for long term operation, during which time voltages and other key parameters were monitored and recorded. The operational conditions during this test period can be seen in Table 8 below. For comparison purposes, the voltage trend data for both cell stacks has been plotted in Figure 55.

Operating Conditions			
Current	Pressure	Temperature	Flow
160 Amps	425 psig	50 °C	400 mL/min

Table 8: Verification Stack Operating Conditions

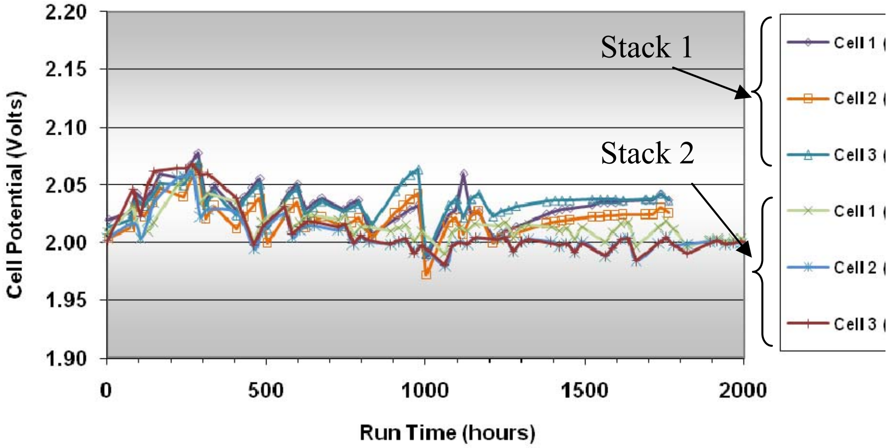

Figure 55: Verification Stack Trend Data, 160 Amps, 425 psi

After completing 500 hours of operation, it was observed that the performance of the two cell configurations was very similar. A decision was made to proceed with full scale validation testing using configuration 2. With flow field design and verification complete, the final cell configuration was identified. The theoretical thickness of the cell design could then be predicted by summing the nominal thicknesses of all cell components in the seal area. While the anode electrode components were assumed incompressible, the remaining active area components were assumed to be compressible. Although the compressed cell thickness was very similar to the legacy cell design, the uncompressed height of the cathode flow field was higher than for the legacy cell. This difference was important to note because it would have an impact on the assembly process. If the cells were too tall during assembly, they might not all fit on the insulated section of the bolts. Using the theoretical cell thickness, a total cell stack height was calculated and compared to the old cell to ensure compatibility of the bolts. Later in the project, after the construction of the 34-cell validation stack was complete, it was possible to take a measurement of the compressed cells and determine an actual thickness. In order to prevent snagging parts on threads but still take advantage of the full bolt length, thread covering tubes were fabricated and eventually used in the build of the 34-cell validation stack.

Once the appropriate ATP steps were complete, the full scale cell stack was installed in the production test rig for standard break-in operation (48 hour green run). The conditions for the testing can be seen in Table 9 below as well as the measured cell potentials at the 1, 24, and 48 hour time intervals.

Green Run Conditions of RND1020201			
Current	Pressure	Temperature	Flow
160 Amps	385 psig	50 °C	Standard

Green Run Performance Data RND1020201								
			Potential (Volts) at 162 Amps					
	Time (hours)		Average	MIN	MAX	Std Dev		Temp (deg C)
Ambient	n/a		n/a	n/a	n/a	n/a		n/a
388 psig	2		1.99	1.97	2.01	0.007		50
385 psig	25		1.99	1.98	2.00	0.005		50
388 psig	48		1.99	1.98	2.00	0.005		50

Table 9: Green Run and ATP Data

The cell stack was then operated for over 1,000 hours. During that period of testing, the new cell stack assembly successfully demonstrated achievement of target cell potentials and gas production without leaks or failures occurring. The conditions for this longer term durability test can be seen in Table 10 below while the measured total cell potentials can be seen in Figure 56. The voltage trend indicates that the cell stack operated as should be expected in the first 1,000 hours.

Operating Conditions of RND1020201			
Current	Pressure	Temperature	Flow
160 Amps	415 psig	50 °C	Standard

Table 10: Operating Conditions

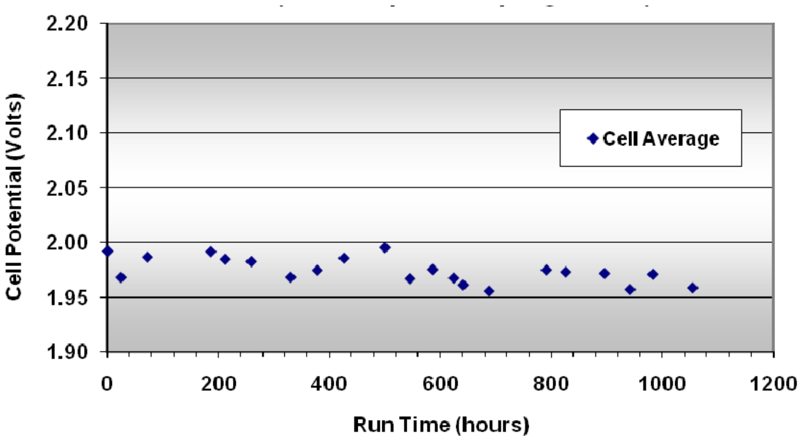

Figure 56: Average Trend Data, 34-Cell Stack

5.2.3 Subtask 2.3 Metal-Composite Plate

The properties listed in Table 11 below characterize the three carbon materials evaluated vs. the baseline. The data indicates that the impermeability of Carbon 1 would be ideal for preventing diffusion of hydrogen or oxygen if used to make bipolar plates. In contrast, the conductive plastics would theoretically allow some diffusion of gas and therefore may be limited to use as flow field inserts. It was anticipated by Entegris engineers that the presence of a titanium or titanium nitride surface coating would be sufficient to mitigate this issue.

Summary of Relevant Material Properties				
Property	Ti	Carbon 1	Carbon 2	Carbon 3
Compressive Strength (ksi)	20 (tensile)	20 (comp.)	11 (comp.)	5.9 (tensile)
Electrical Resistivity (µOhm-cm)	49	1,470	25,000	25,000
H2 Permeability (*Barrer 10-10cm3cm/cm2scmHg)	Negligible	0.063	35.6	243
O2 Permeability (*Barrer 10-10cm3cm/cm2scmHg)	Negligible	Negligible	10.9	73
Material Compatibility	Yes	Yes	TBD	TBD

Table 11: Material Properties of Carbon Materials vs. Ti Baseline

Although it was anticipated that resistances would be significantly higher for the plastic samples once assembled into cells, the recorded resistance values were all very close to the baseline. This may have been because the perimeter of the pocketed screen pack provided a conductive path around the samples thus masking their resistance. Representative operational cell potential data has been plotted in Figure 57 below. In all cases, performance was steady between 2.10 and 2.20 volts, which is normal for the configuration tested. These operating potentials also should have been sufficient for creating a corrosive environment around the samples. Ultimately, there were no observed decay rates which would have indicated significant oxidation of the coatings or corrosion of the substrates. Each cell stack was diffusion tested at 200 psig but only operated at 100 psig in an effort to reduce the chance of any leak related failures and increase the chance of having an uninterrupted 500 hour electrochemical exposure.

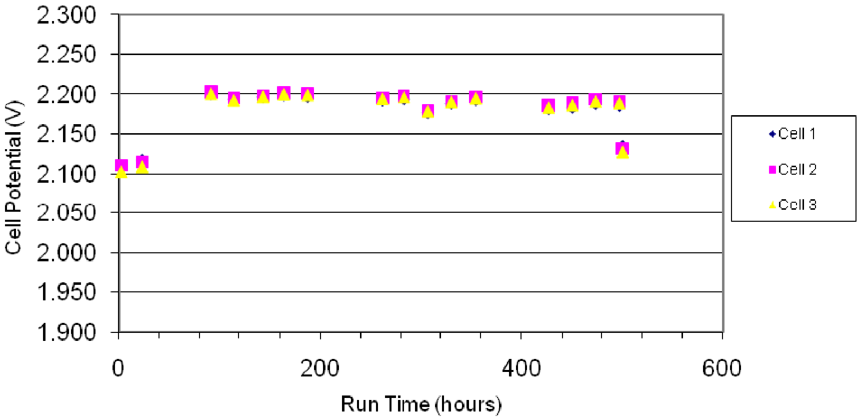

Figure 57: Flow Field Durability Testing: Cell 1 = Carbon 1 + TiN, Cell 2 = Carbon 2 + TiN

The masses of each test sample were recorded before and after operation. Rather than losing mass as a result of corrosion, the samples generally increased in mass. This was most likely due to absorbed water within the samples, as it was observed that the parts were typically saturated when removed from the cell assembly. An effort was made to allow the parts to dry out thoroughly before measuring mass, but residual water may have still been present. This apparent tendency to absorb water provides an indication of material/coating permeability. Electrochemical corrosion calculations developed after the test indicated that these samples should have lost less than 0.01 grams in 500 hours, potentially falling below the measurement accuracy of this test. In contrast, a 10,000 hour test should result in a 0.20 gram loss, thus making it easier to determine if corrosion was occurring as expected.

In all combinations of substrate materials and coating types, a common defect was chipping of the coating at the sharp edges of the parts. Several of these defects may have been created during installation into the pocketed screen pack as made evident by the proximity of the chips with the adjoining part (Figure 58). Some scratches had crisp, straight edges (Figure 59) which were unlikely to have formed by corrosion mechanisms. These defects certainly illustrate the sensitivity of the coated parts and show that careful design and handling of the parts would be required in a production scenario.

Figure 58: Chipped Edges

Figure 59: Scratched Edge

Despite the resulting exposure of substrate material, digital images taken of particular sites before and after operation showed no sign of significant corrosion. The images in Figure 60 and Figure 61 show a crescent shaped defect before and after operation. In some cases, long cracks were found in the flat area of the samples before operation. Figure 62 and Figure 63 show the before and after images of such a crack. In all cases, images of a given defect before and after operation showed no sign of corrosion. This may indicate that the corrosion rate of these substrate materials is very low or perhaps negligible. Long term endurance testing of parts will be required in order to verify this.

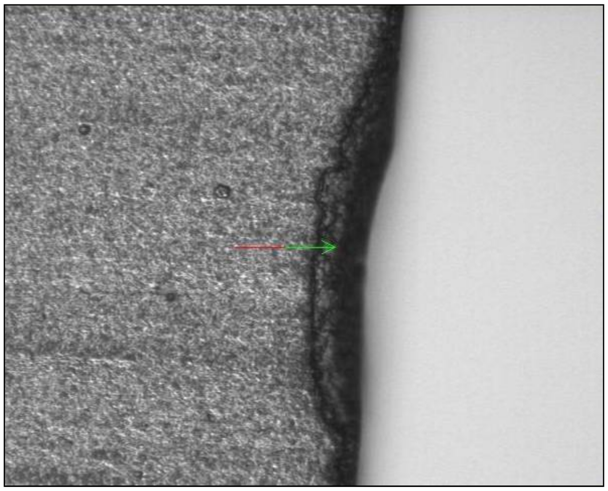

Figure 60: Crescent Defect, Before Operation

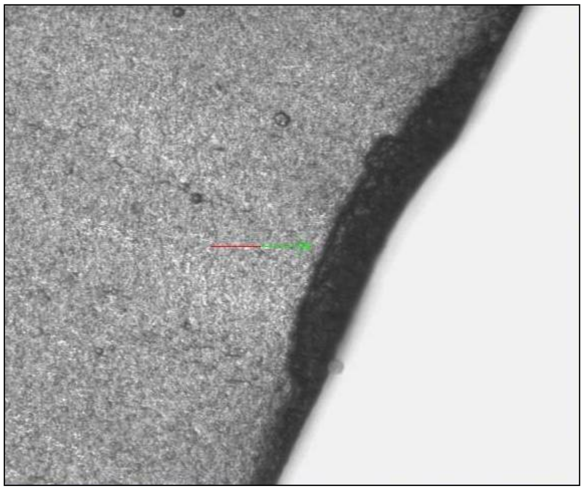

Figure 61: Crescent Defect, After Operation

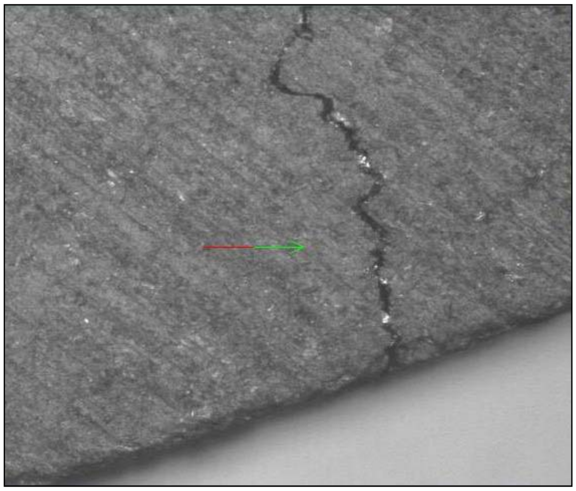

Figure 62: Crack Defect, Before Operation

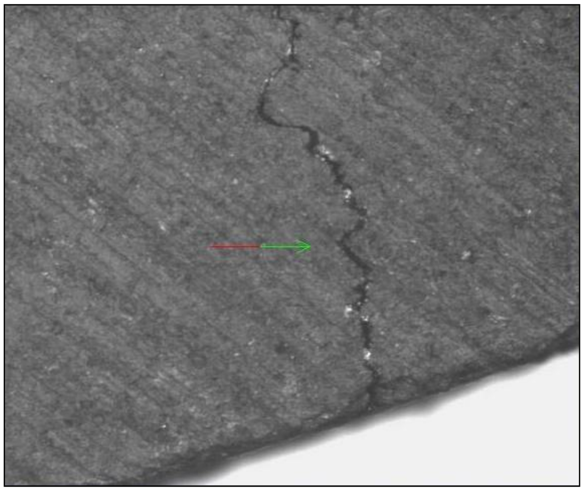

Figure 63: Crack Defect, After Operation

Results of the material strength analysis indicated that all three material samples experienced between 7,000 and 8,000 psi when axially loaded to 5,410 lbf. In conjunction with loading the test strips, it was also necessary to verify that the samples successfully withstood the applied pressure without crumbling or cracking. The collected images of sealing features from before and after loading showed no signs of cracking or crumbling. In an effort to quantify permanent deformation, the thickness measurements were also made before and after testing. The results indicated that sealing features appeared to have a negligible height reduction after being compressed.

After completing an extraction test to determine the non-volatile residues (NVR) that could potentially contaminate the cell stack, the data was tabulated against historical baseline data for polypropylene (Table 12). It was decided that these results were close enough to the baseline to justify experimental testing within electrolyzer cells. When comparing the water absorption percentages below to the observed mass increases, it may be concluded that the Carbon 1 is less permeable than the Carbon 2 and Carbon 3. This is consistent with the permeability properties presented in Table 11.

NVR Testing of Alternative Materials		
Material	Average NVR, (mg/in^2)	Average water absorption (%)
Polypropylene (baseline)	0.09	0.91
Carbon 1	0.81	ND
Carbon 2	0.44	0.57
Carbon 3	1.51	0.66

Table 12: NVR Test Results

Operational Testing

In this stage of testing, focus shifted to functional components designed to operate in place of traditional components. These cells generally had higher resistances than typically experienced in cells with 10-mil membrane, but they were still within the previously accepted cross-cell resistance ranges. The use of Carbon 2 seemed to have lower impact on cell resistance when used as a cathode insert as opposed to an anode insert. This indicates that Carbon 2 may be comparable to carbon paper based flow fields but not as close to titanium flow fields. When used as anode inserts, Carbon 3 and Carbon 2 appeared to have comparable impact on resistance.

Although ATP resistances provide a useful initial assessment of cell integrity, measured cell potentials at operating conditions provide a much better indication of performance. Operational trend data for short stacks is plotted below. Steady performance was observed in all cases and it was possible to make some comparisons between materials and coatings. The operating potentials in Figure 64 and Figure 65 below indicate that the Ti+TiN coated Carbon 2 bipolar plate ran 100 mV lower than the Ti coated Carbon 1 version. This result correlates with the cross-cell resistance data observed during ATP but does not seem consistent with the published material conductivity properties. Further testing would be required to determine if this was a function of the bipolar plate material properties, active area pressure, or variation in the MEAs.

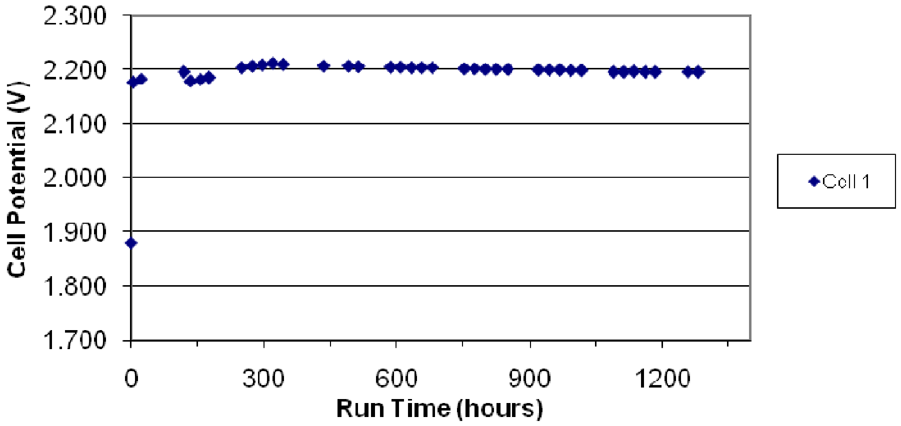

Figure 64: Operational Potentials for Ti Coated Carbon 1 Plate

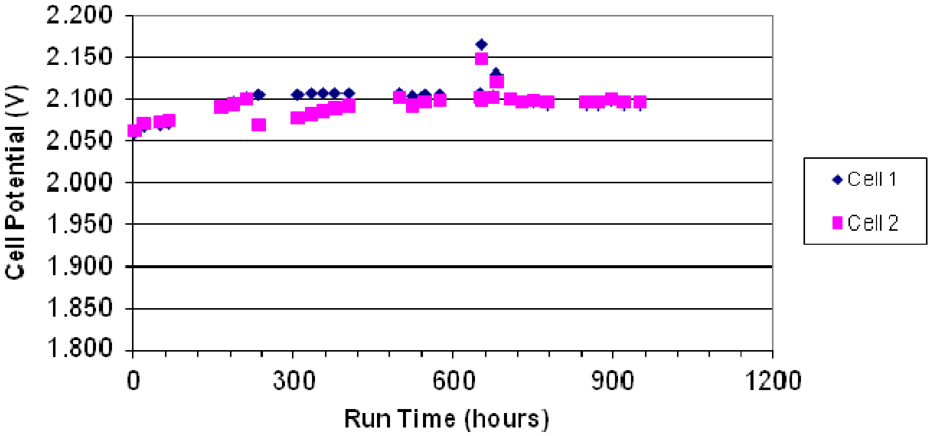

Figure 65: Operational Potentials for TiN Coated Carbon 2 Plate

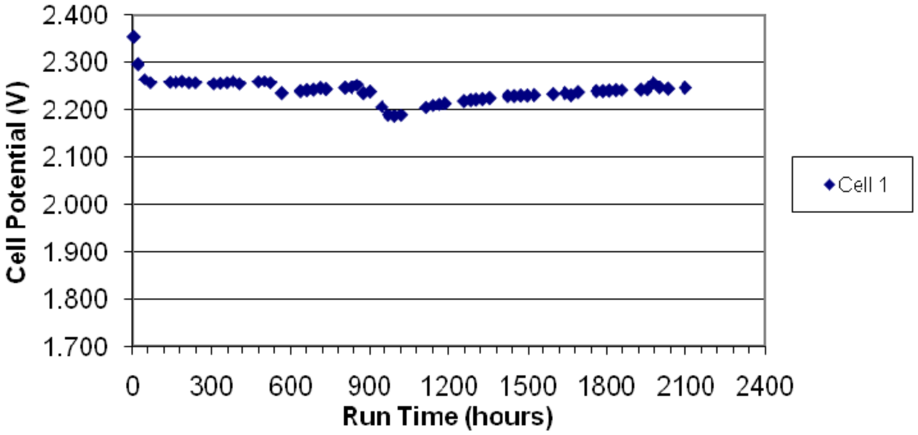

Figure 66: Operational Potentials for Ti Coated Carbon 3 Insert

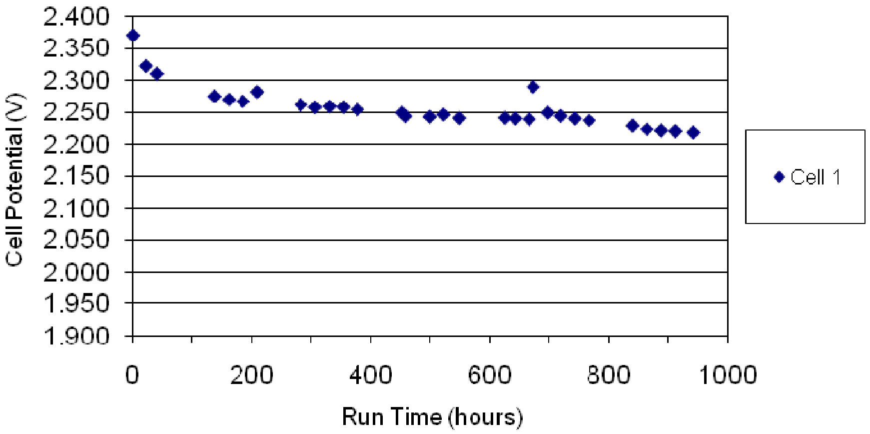

Figure 67: Operational Potentials for TiN Coated Carbon 2 Insert

Additionally, the data shown in Figure 68 indicated that uncoated Carbon 2 cathode insert can perform comparably to a legacy 0.1 ft^2 cell. The chart in Figure 69 shows how any voltage penalties incurred from using these alternative materials compares to the legacy 0.1 ft^2 cell design as well as the solid chem.-etched bipolar plate.

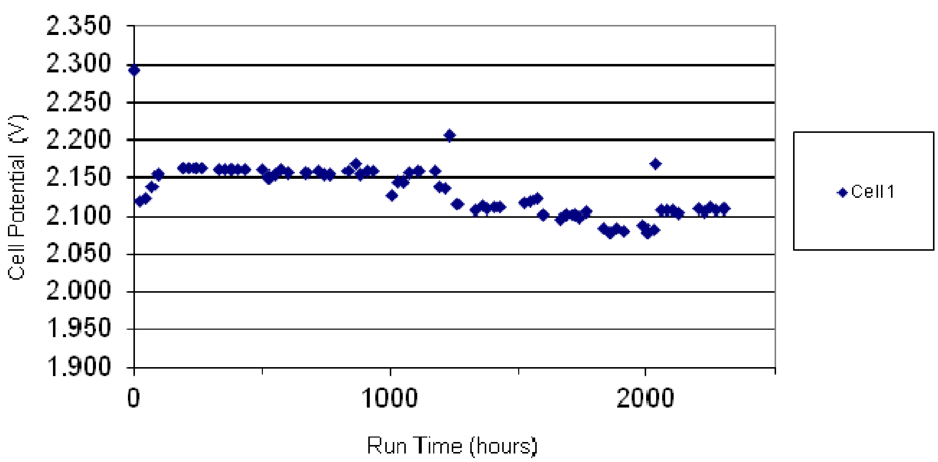

Figure 68: Operational Potentials for Uncoated Carbon 2 Cathode Insert

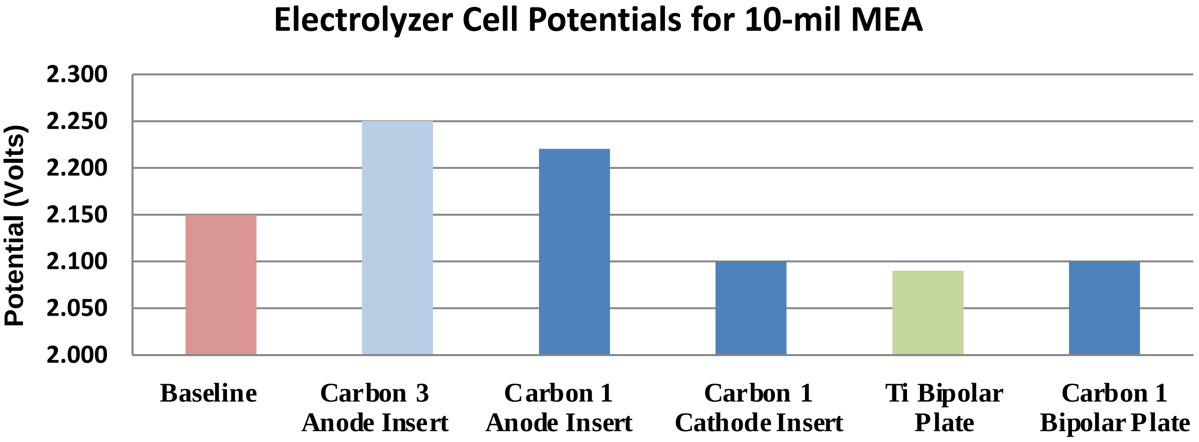

Figure 69: Relative Cell Potentials, 0.1 ft^2, 50 °C

The results of this testing provided confidence in the general approach, to be compared with the other design options described below.

5.3 Task 3.0 Prototype Bipolar Plate Development

In addition to the carbon-based plate described above, other configurations were evaluated for potential cost reduction. Alternate cell architectures including full bipolar plates, anode and cathode inserts, or intermediate integration of parts were considered. Manufacturing technologies included plastic injection molded parts, diffusion bonding, adhesive bonding, electron beam welding, hydroforming, stamping, coining, machining, chemical etching, and investment casting.

A decision matrix was created to track different combinations and associated cost. Within the matrix, a list of 27 possible candidates was created based on the combinations, which were scored on multiple criteria including assembly cost, non-recurring engineering (NRE) cost, risk, development time and cost, fabrication steps, material risk, process maturity, and cross-cell permeability. The existing round and square cell designs were used as the cost baseline. Figure 70 shows examples of the rankings for non-recurring/development expenses, technical risk, and cost at volumes of 10,000. As seen from the chart, there are several potential methods which could reduce the cost of the plate by half, at moderate risk levels and relatively low non-recurring costs.

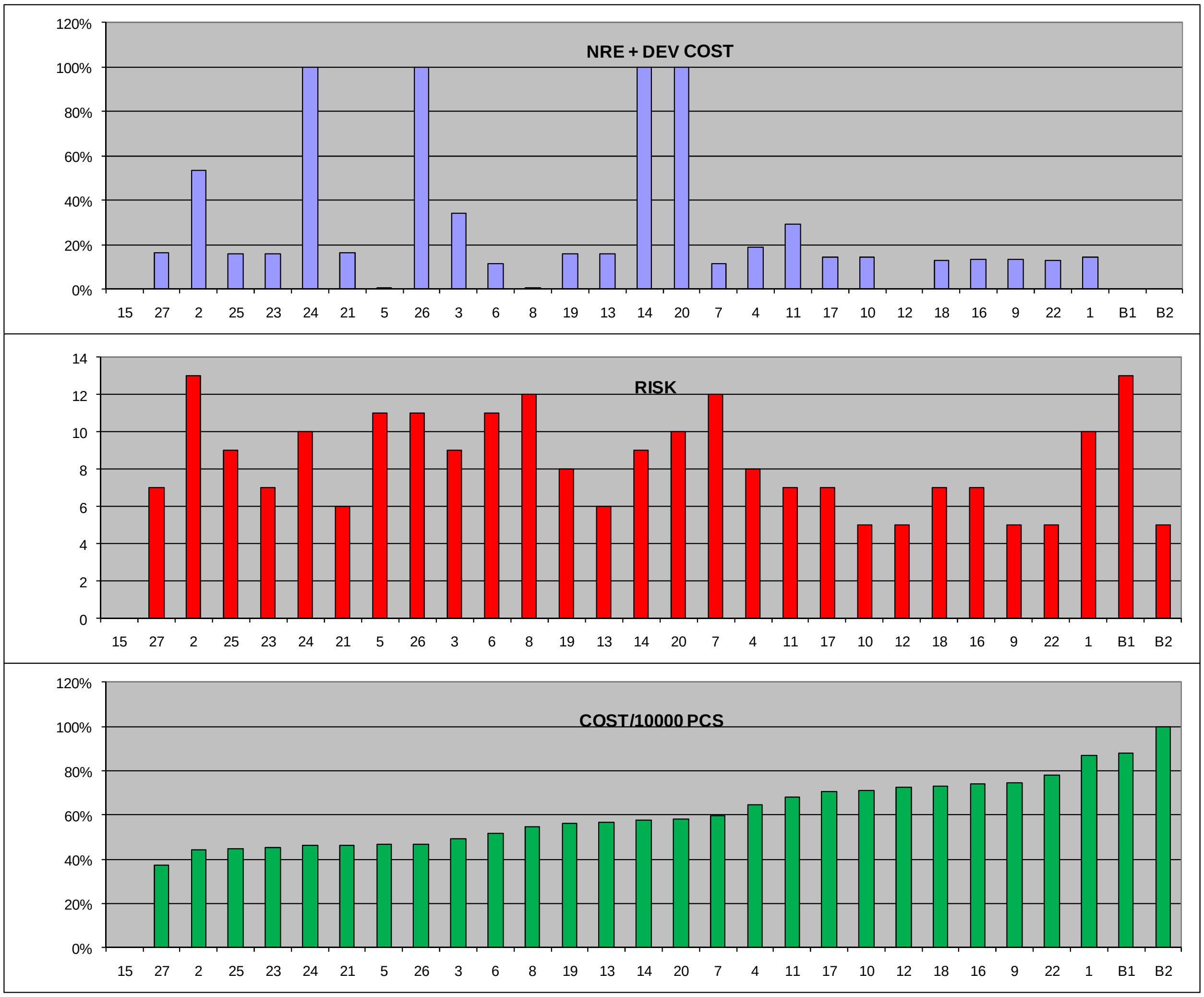

Figure 70: Evaluation Results for 27 Concepts vs. Baseline

Based on part cost and risk level, conceptual parts were made with some suppliers to determine feasibility. These included E-Beam welding of multiple layered thin Ti sheet, coining of sealing features into Ti sheet, and machined carbon parts with and without TiN coating. Through this screening, some manufacturing methods were determined to not be cost effective. For example, diffusion bonding is a batch process with limited ability to increase units/batch without oven size upgrades, so cost per part can be high. Lead candidate suppliers also indicated limitations on stackup height. The process has two variables, pressure and temperature, such that controlled pressure in a large stackup can be problematic. After investigation, investment casting Ti with small features was also found to be difficult. Similarly, stamping/coining thin sheet Ti is difficult to process and would most likely result in a distorted or twisted part. Flow field area was of particular concern due to long thin webs of material. Chem-etching was judged to be very complex, with multi-step parts resulting in high supplier fallout and high prices. Machined graphite plates were also determined to be too expensive.

Based on the analysis and test parts, the downselected option was a titanium separator plate with formed anode features, and a single piece molded cathode flow field. This option provides significant part reduction, no machining, and enables high speed manufacturing of the anode plate. It also enables significant reduction in titanium usage, providing both material and labor savings. Based on supplier audits, this technique also has the capability to scale to the desired active area for Proton's next cell stack platform.

Once this pathway was selected, a similar development pathway was followed as described above for the cathode flow field effort. Prototype parts were used to evaluate the cell stack up and active area pressure, sealing capability, and flow characteristics. Based on the electrochemical and flow modeling that had been completed as part of Task 2.1, initial parts performed very well and very little modification in dimensions or cell features were required before parts were fabricated for electrolysis testing. In cell testing is described in the next section.

Hydrogen Resistant Coatings
It was hypothesized that residual stress in titanium plate could increase hydrogen uptake and eventual embrittlement in the part. Results of residual stress testing are shown in Table 13 below, showing that even the raw material contains significant residual stress. Annealing can remove this residual stress. However, the baseline process adds considerable stress back into the part, even when annealed. Annealing after processing is much more effective at reducing the residual stress. The impact of this reduction is shown in Figure 71 below, indicating a 50% reduction in uptake rate. Still, while annealing can significantly reduce hydrogen embrittlement, it adds to an already costly process to coat the plates to maintain conductivity. Nitriding was therefore examined as a potential replacement for the existing process. Nitriding had previously shown very low uptake in Proton experiments, as confirmed in the ORNL experiments (Figure 71). Figure 71

Process Step	Residual Stress (MPa)	Standard Deviation
Unprocessed	-134	10
Annealed only	15	9
Baseline process	-387	47
Annealed – Baseline	-384	58
Baseline – Annealed	30	29

Table 13: Residual Stress Measurements For Titanium Plates

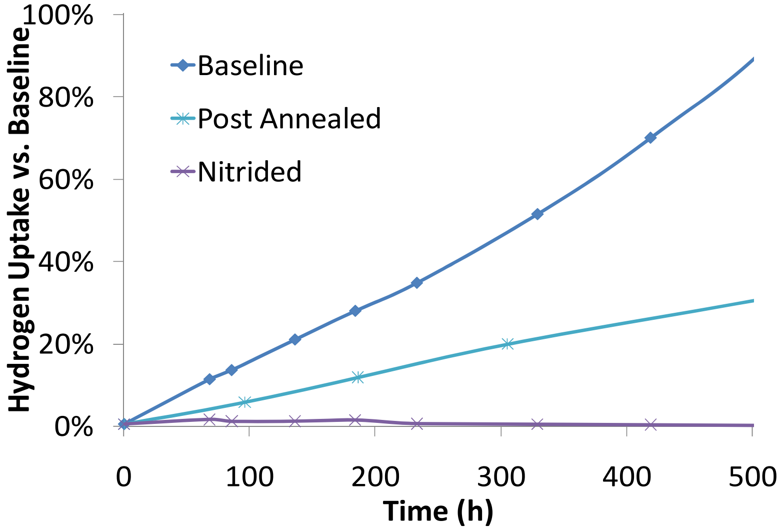

Figure 71: Hydrogen Uptake as a Function of Process Steps

Both plasma nitriding, which is a coating process, and thermal nitriding, which is a conversion process, were examined. Pure titanium and titanium alloys were also investigated by Oak Ridge National Lab (ORNL). Initial samples given to Oak Ridge for SEM evaluation showed differences in the resulting layer composition based on the type of nitriding used. Plasma nitriding provided a uniform layer of TiN, which Proton has previously shown to prevent uptake and provide several thousand hours of performance at steady voltage. ORNL thermal nitride provided a much thicker layer but was mostly composed of Ti_2N (Figure 72, upper panel).

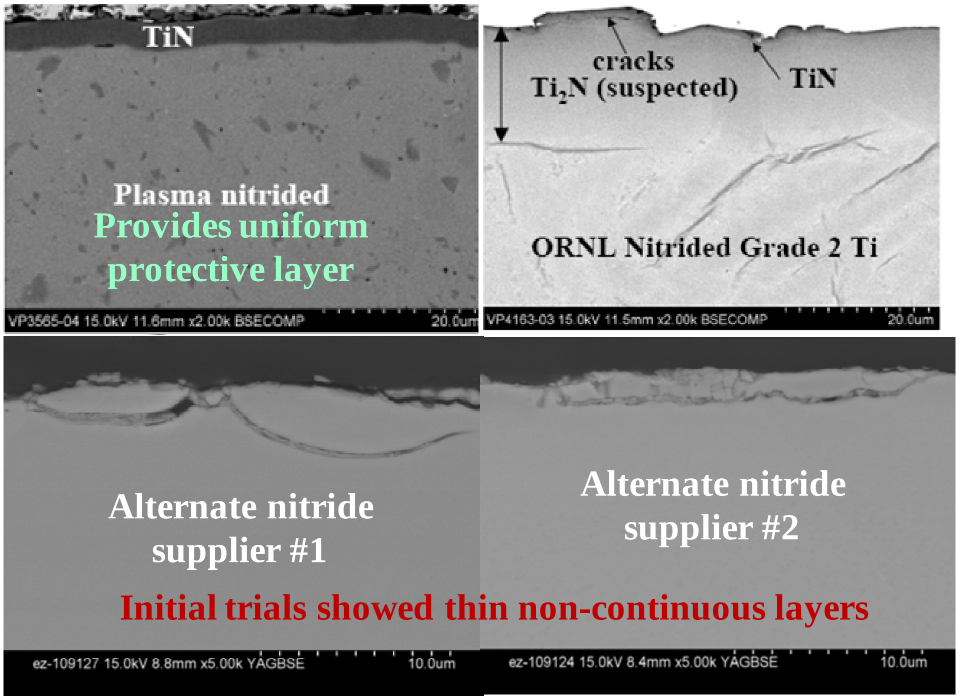

Figure 72: SEM of Nitrided Titanium Samples

At the beginning of the program, it was not clear whether the two compositions would provide the same level of protection to oxidation on the anode. Initial survey of thermal nitride suppliers outside of ORNL also demonstrated that additional work was needed to obtain a suitable layer for hydrogen protection (Figure 72, bottom panel).

Several manufacturing methods were surveyed for nitride coatings. Overall, deposition methods are line of sight limited and the batch size is limited at large active area. Thermal methods provide more flexibility but can result in less desired compositions. Initially, it was suspected that there would be a preference for TiN vs. Ti_2N for higher corrosion potential, although subsequent electrochemical testing has shown that Ti_2N appears stable. Proton worked with multiple suppliers to tune the application parameters for the desired results. Plamsa nitrided parts were also fabricated with similar features to the planned design in the active area. Uniform coatings were obtained even within the channels, providing a promising pathway for this approach. Suppliers of thermally nitride parts were also able to improve layer deposition and provide a part with uniform thickness (Figure 73).

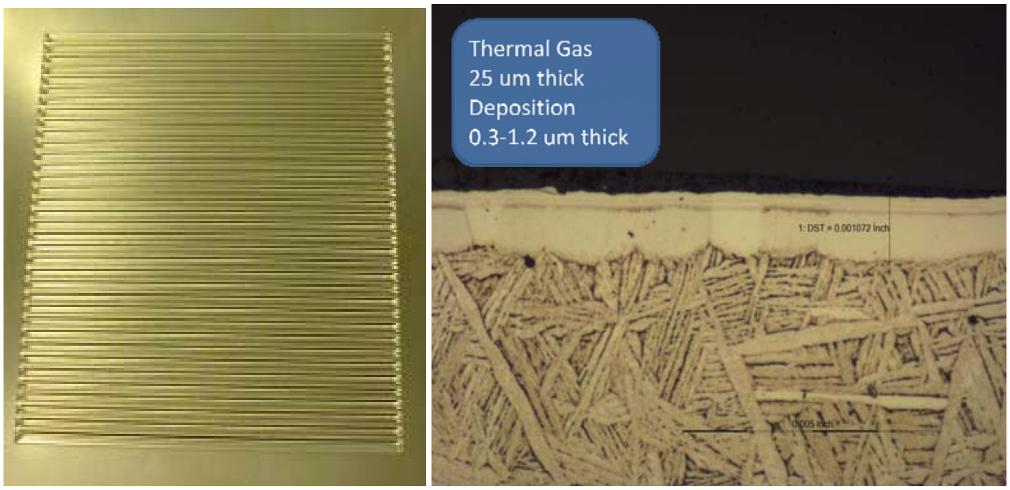

Figure 73: Plasma Nitrided Anode Flow Field and Cross-Section of Thermally Nitrided Part

ORNL performed electrochemical screening tests on various titanium parts. Samples were originally tested with a commercially available gas diffusion layer (GDL) material. The titanium alloy parts provided slightly better voltage performance before nitriding. However, the voltages were very high vs. typical electrolysis operation. Proton provided proprietary GDLs to ORNL for additional testing, which brought the performance closer to more typical levels. Based on the results, most work focused on the base Ti material as the substrate, although it is possible that with an optimized GDL, the alloy would provide additional performance benefit. Thermally nitride samples were then operated for 500 hours, with negligible change in performance (Figure 74).

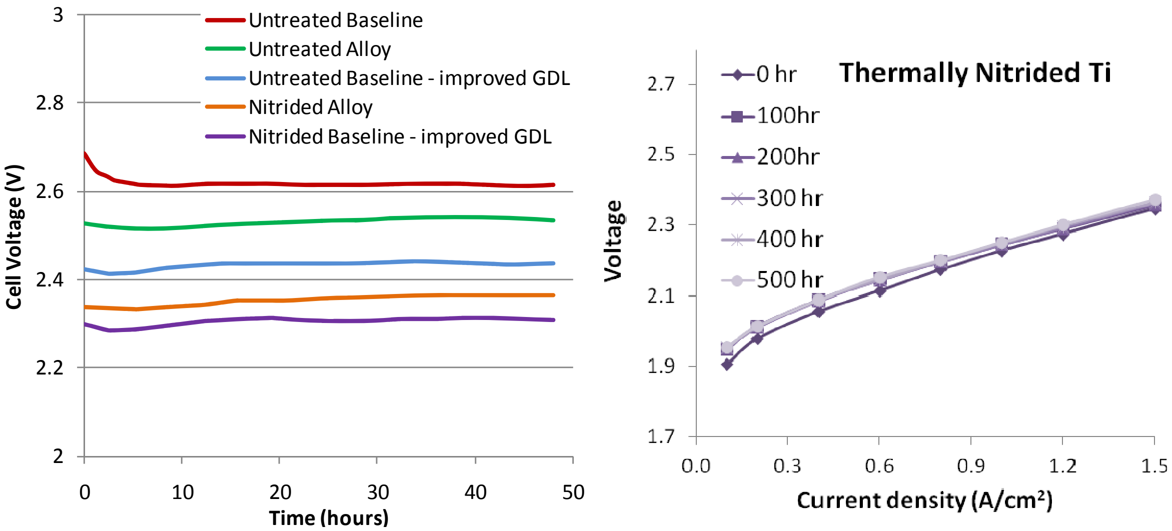

Figure 74: ORNL Electrochemical Screening of Titanium Samples

5.4 Task 4.0 Prototype Bipolar Plate Evaluation

5.4.1 Subtask 4.1 Sample Operational Tests

For the next stage in qualification, nitrided plates were made with the desired features using the downselected manufacturing process and inspected before building into cell stacks. Single cell stacks passed all acceptance criteria and showed no concerns in operation over several hundred hours. A three-cell stack using the same component configurations was then built and operated for 5000 hours for the evaluation of hydrogen uptake and other visual analysis. The stack and operating data are shown in Figure 75 below.

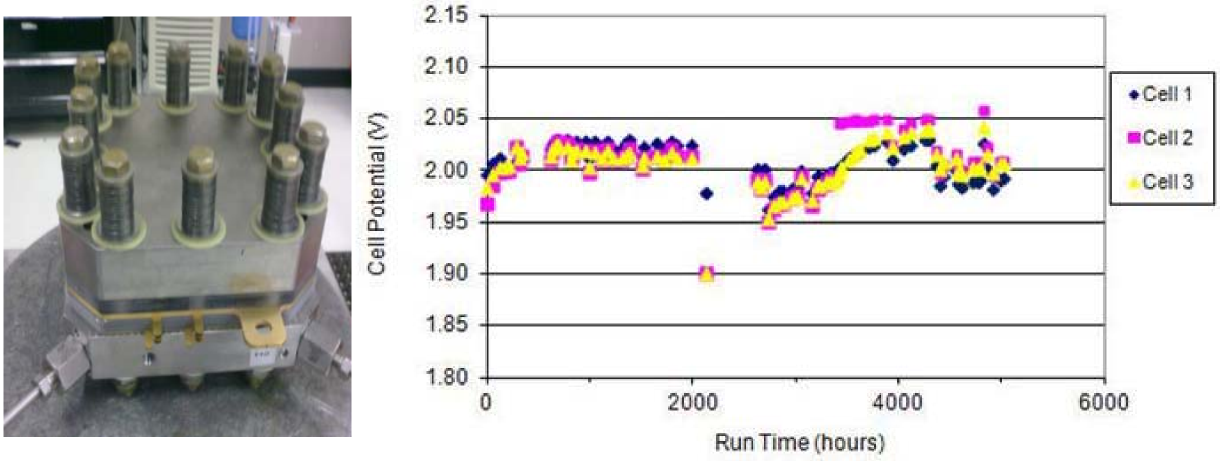

Figure 75: 3-Cell Stack and Operating Data

5.4.2 Subtask 4.2 Post Operational Testing Analysis

Samples from the above cell stack were sent back to ORNL for analysis. Parts removed from operating stacks showed some discoloration after 500 hours, limited to the channels. The land areas, which are directly in contact with the catalyst layer, showed much better retention of the typical gold nitride color (Figure 76, top left). Within the channels, the discoloration appeared to be due to loss of the nitride layer (Figure 76, top right). XPS depth sputtering analysis at different areas of the part showed some oxidation of the part in the channels, but no corresponding change in voltage was observed, indicating that sufficient conductivity was maintained in the critical areas (Figure 76, bottom).

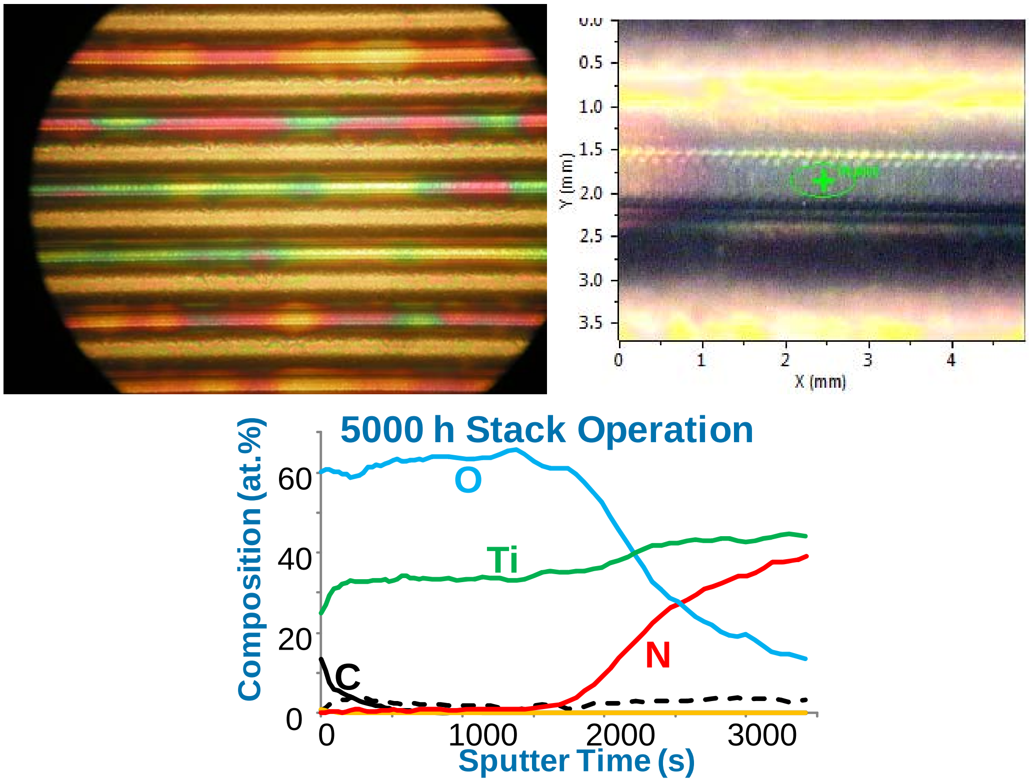

Figure 76: Part from 5000 Hour Cell and XPS Analysis of Surface Composition

5.4.3 Subtask 4.3 Stack Scale Up

Based on the results of Tasks 4.1 and 4.2, the 10-cell stack was built and placed on test. This stack is depicted in Figure 77. As of this report, the stack has been operational for nearly 10,000 hours, with steady voltage, indicating the continuing stability of the nitride coatings.

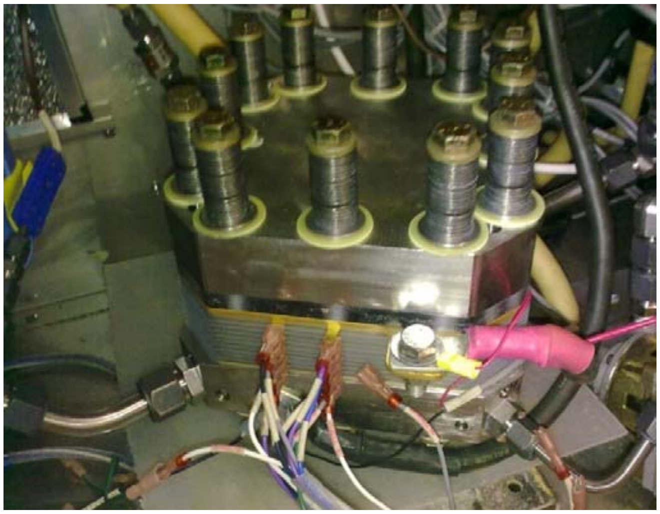

Figure 77: 10-Cell Validation Stack Installed in System

In parallel, the larger stack active area was initiated. Based on supply chain capability, the final active area was set at 680 cm^2. Design refinement of large active area stack included finite element analysis (FEA) of critical components such as flow fields, frames, endplates. CFD modeling of individual cells was performed to determine sensitivity analysis to flow rate variations, while CFD of the entire stack was performed to understand cell count impact on individual cell flow rate. Examples of the modeling output are shown in Figure 78. Based on the output of the modeling calculations, the design parameters were finalized.

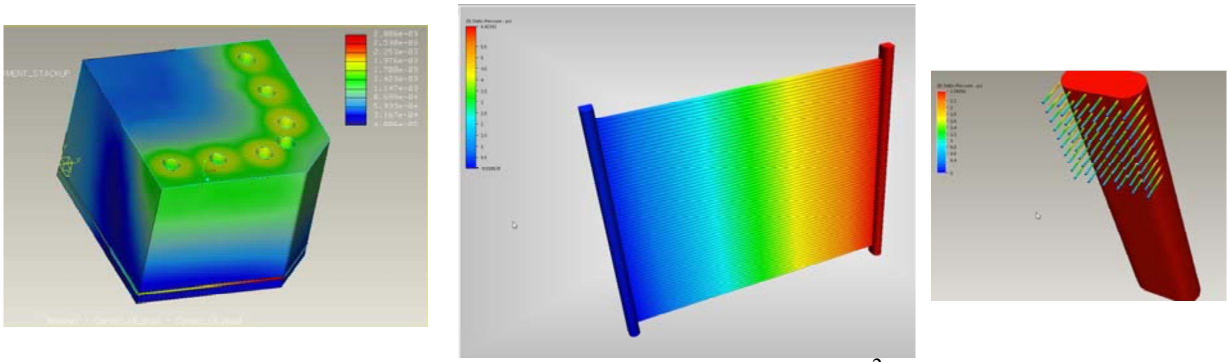

Figure 78: Examples of FEA and CFD Analysis for 680 cm^2 Active Area Stack

5.5 Task 5.0 Bipolar Plate Manufacturing Development

Once the initial proof of concept nitrided titanium parts were successfully operated and the modeling was completed, final design changes were made to maximize the manufacturability of the stack. Design for manufacturability included frame orientation features for error-proofing of the assembly, and development of GDL registration features for alignment were developed. Load testing was completed on the GDL and separator to verify the results of the FEA modeling, and no deformation was observed. Frame testing was also completed. A successful hydrostatic test was achieved to a proof pressure of over 700 psi.

Critical features of the new bipolar plate design were fabricated by the supplier and measured for dimensional tolerances to finalize size and spacing. Several iterations of the geometry were attempted in order to optimize the shape for manufacturability. Parts are shown in Figure 79 with proprietary features obscured for both the 100 cm^2 and 680 cm^2 designs.

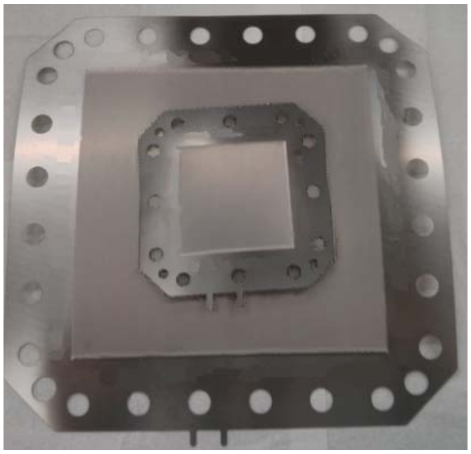

Figure 79: Small and Large Separator Plate Developed in this Program

Due to the material characteristics of titanium, the design was modified to ensure quality and repeatable components. Pressure testing was completed to 1.5 times the operational design intent with the full set of cell parts. Flow testing showed the appropriate pressure drop.

Membrane electrode assembly development was based on Proton's existing processes for membrane processing, tooling, and other equipment. Ink formulations developed under the SBIR mentioned in Task 1 were leveraged in the final MEA fabrication for this project. Tooling was procured and manufacture of large active area MEAs was completed. A single cell stack was built and operated for 1000 hours (Figure 80) before taking the stack apart and building a 3-cell stack.

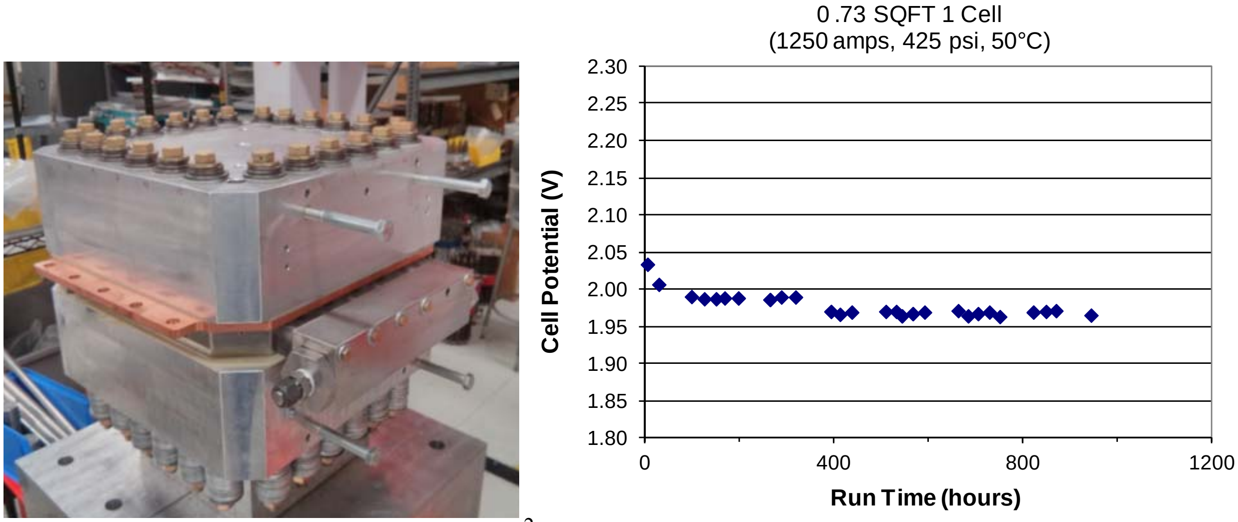

Figure 80: 0.73 ft^2 Cell Stack and Operational Data

5.6 Task 6.0 Bipolar Plate Manufacturing Qualification

A final prototype die was made based on the previous testing to ensure that the flow field geometry was manufacturable. Several lots of material were tested using this prototype die with successful results. The first production bipolar plates manufactured using the production die were received. Feedback to the supplier regarding minor cosmetic defects that occurred during shipping and a minor manufacturing quality issue were both resolved with the second production run. Dimensional analysis to determine manufacturing capability and dimensional accuracy showed that both runs resulted in parts that met all dimensional and functional criteria. Fit check with adjacent components was verified. The supplier and manufacturing method for the bipolar plate is at a state where Proton is comfortable transitioning these parts into production. Several hundred parts were ordered and have been received. A 10-cell stack was built and operated for 500 hours.

5.7 Task 7.0 Cost Analysis

5.7.1 Subtask 7.1 Product Cost Model

The Bills of Materials (BOMs) for all of the stack design generations developed in this program were summarized and compared. At the 100 cm^2 stack level, the initial cost reduction on the carbon flow field provided a significant portion of the overall cost savings. However, conversion to the new bipolar assembly and implementation of a fully inked electrode with 50% reduction in catalyst loading provides more than double the cost savings (Figure 81). Overall, this program was successful in commercialization of a 15% reduction in cell stack cost for three years of production, and in providing a pathway to overall cost reduction of over 40% in cell stack cost for Proton's S-series and H-series products. The advanced stack is slated to be released to production in 2014.

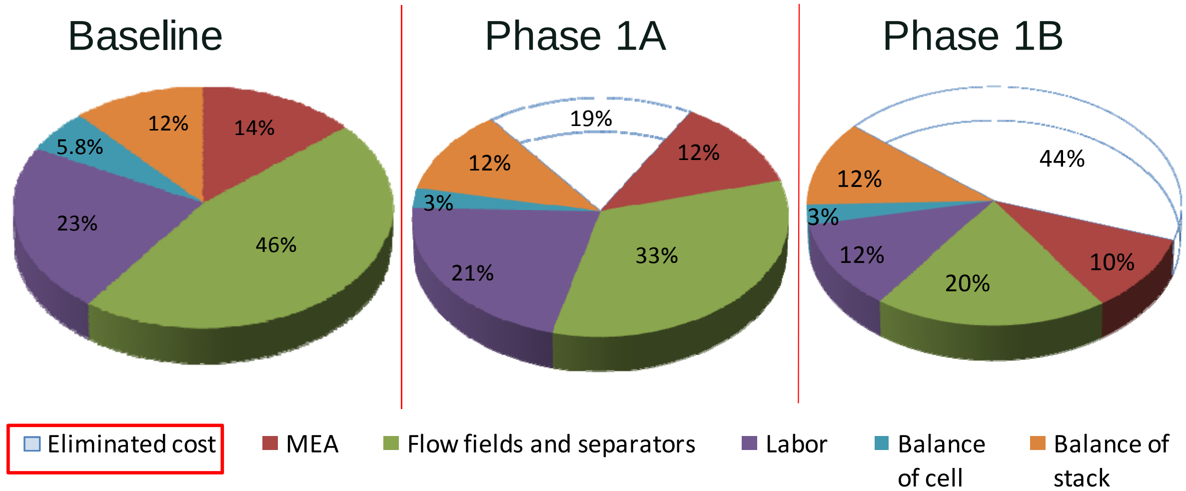

Figure 81: Cost Reduction for 2008 Baseline vs. Expected 2014 Commercial Product

Proton also had an existing 550 cm^2 cell stack design at a prototype level which provided a baseline for assessing the cost reduction for the large active area design. This legacy design would have served as the stack platform for Proton's next generation system development effort and also provided confidence in many of the design calculations and approaches in this program. The new design developed in this project was scaled to 680 cm^2 and still resulted in cost reduction of approximately 40% (Figure 82).

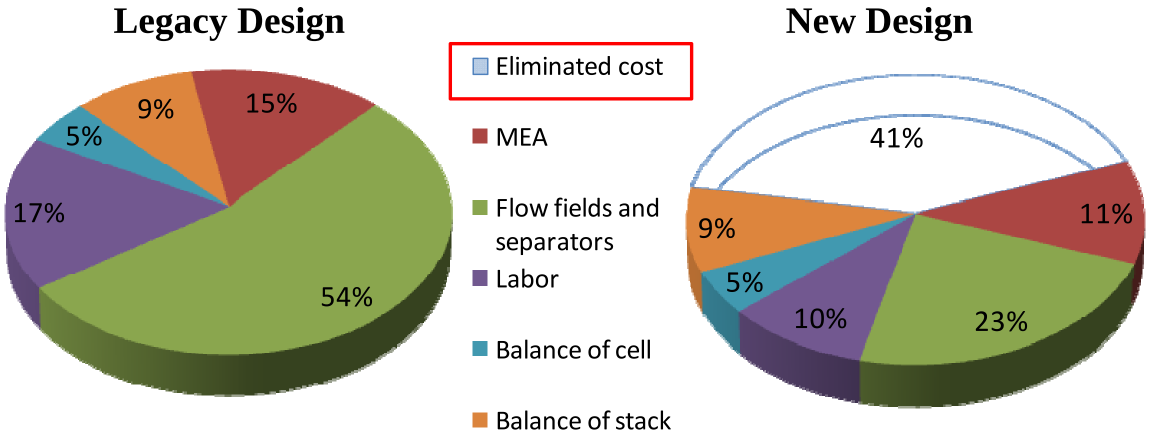

Figure 82: Cost Comparison for Large Active Area Designs

The two cell stacks are shown side by side in Figure 83 below. From the photo it can be seen that the cheaper, larger active area stack (right) is significantly more compact than the legacy stack (left), providing some support for the large cost savings realized. In addition, similar to the 100 cm^2 design, the new large active area design removes approximately 50% of the titanium from the cell.

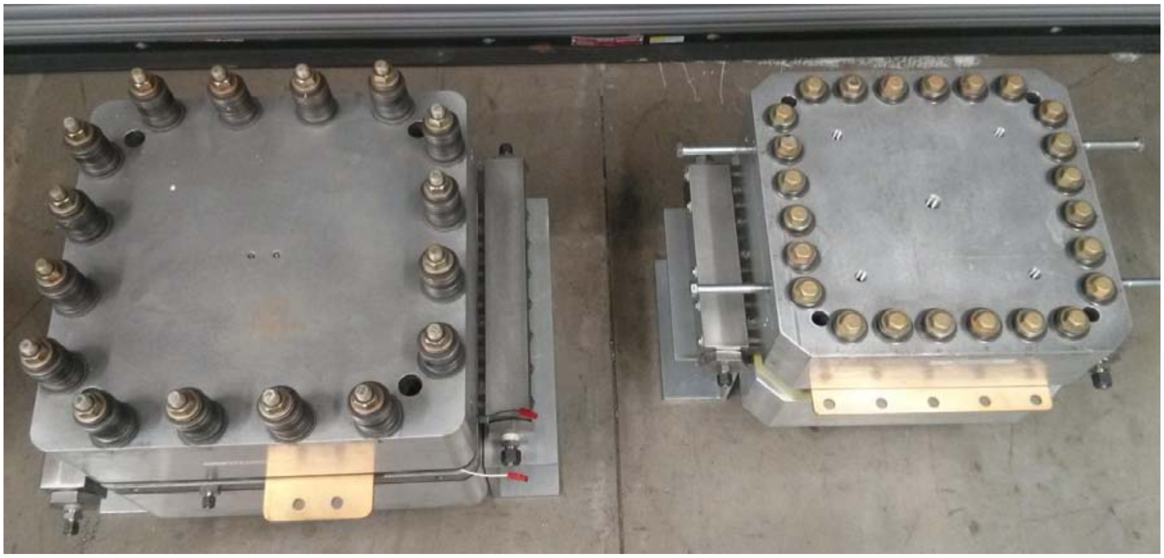

Figure 83: Legacy Stack vs. 40% Cost-Reduced Stack (20% Larger Active Area)

5.7.2 Subtask 7.2 H2A Model

This program focused on cost reduction and advanced manufacturing, with minimal emphasis on efficiency. Therefore, the key parameter in the H2A Analysis is the capital cost, for comparing one cell stack to another. Costs were input to Proton's electrochemical interface to the H2A model and polarization curves based on current membrane electrode assemblies were added. Based on the current design intent for Proton's MW scale electrolyzers, the operating conditions such as current density and cell count in the stack were used to calculate the cell stack capital cost. Results are shown in Figure 84 below, showing the importance of scale in cost reduction. The cost-reduced 100 cm^2 format is twice the cost per kilogram H_2 vs. the large active area stack.

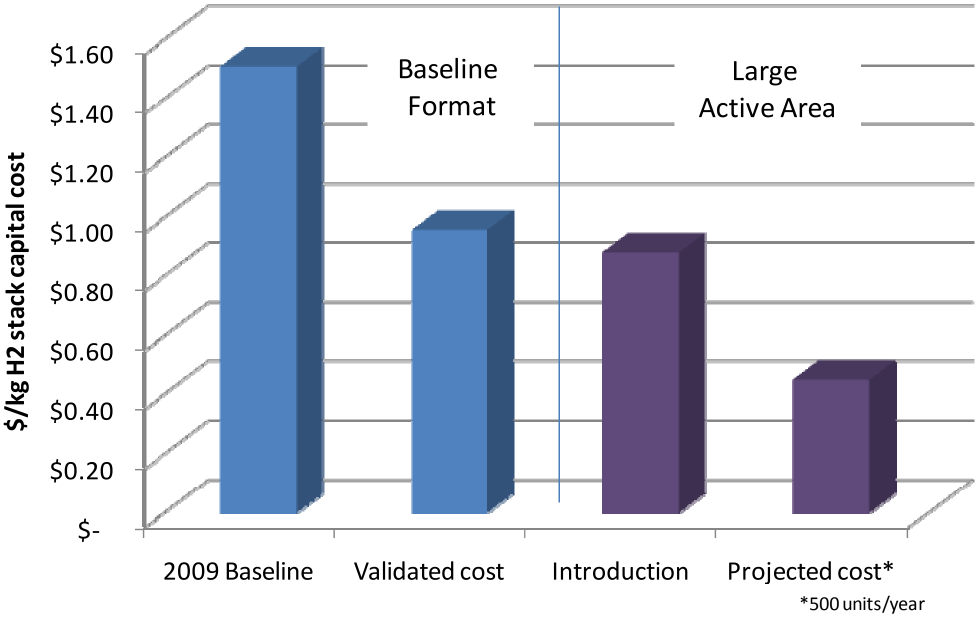

Figure 84: Cost Estimates for High Volume Production of Cost-Reduced Stacks

The H2A model assumes inclusion of existing technology as well as volumes of 500 units/year each capable of producing 500 kg/day in calculating the overall cost of hydrogen. Proton has parallel programs which focus on efficiency improvements and additional cost reduction strategies for the membrane electrode assembly which were therefore included in the calculations for cell voltage and capital cost. Labor reductions and other assumptions for high volume manufacturing such as reduction in set up charges, investment in tooling and equipment for improved throughput, and leveraging of parallel fuel cell supply chain cost reductions were also included. Based on these assumptions, the final cost of hydrogen for the larger system was calculated to be $3.46/kg.

This number compares to current values for Proton's commercial C-series of closer to $9-10/kg, and a system based on the 550 cm^2 active area stack design being closer to $5-6/kg, representing a substantial cost savings based on the portfolio of design improvements being made at Proton.

6.0 Conclusions

This project was highly successful in accomplishing the objectives of the project. While control of catalyst loading was still an issue, initial efforts in anode ink development were successful in demonstrating feasibility for 50% reduction in catalyst loading through improved deposition processes. A subsequent program has since addressed these issues and this process is moving to commercialization. A comprehensive electrochemical and fluid flow model was developed which accelerated design efforts for the flow field cost reductions. Significant understanding of hydrogen embrittlement was gained, as well as factors that impact the kinetics of hydrogen uptake in titanium. Treatments of the titanium were explored for mitigation of hydrogen uptake while reducing cost and maintaining oxidative stability on the anode. Two new stack designs were initiated, taken through the full design process, and validated during the course of the project. Both of these designs provided 40% cost reductions vs. the legacy designs. This program has therefore provided significant cost reduction for Proton's existing product lines, specifically the S-series and H-series products which currently make up the largest number of cells manufactured per year. In addition, the program has provided a stack design which will enable launch of Proton's MW-scale electrolyzer. This effort strategically essential to remain competitive in the marketplace with the increasing need for hydrogen energy storage in Europe. Overall, the program provides a basis for hydrogen production below $3.50/kg, at 1500 kg/day output capacity.

Still, in order to achieve this production cost, additional U.S. investment in manufacturing is needed. With the cost reductions achieved in this program, the membrane electrode assembly (MEA) becomes the highest cost component in the cell. Proton has shown that the catalyst loading can be reduced by an additional order of magnitude through various methods, each of which has shown good durability but requires manufacturing development to be practical. Similarly, much thinner membranes have shown good durability in electrolysis cells over 1000's of hours of operation, but fabrication and assembly processes need to catch up to ensure consistent and robust performance. In addition, existing form factors for gas diffusion layer and flow field materials need to be expanded to keep pace with larger MEA production. New design strategies may be required to match the different supplier manufacturing capabilities. On the systems side, efficiency losses in drying and power conversion need to be addressed, and new design approaches are needed as phase separators and other components reach manufacturing scales that require additional certification and safety chain development. All of these areas are understood at a basic science level, but applied research and development is required to translate this understanding to marketable commercial product.

7.0 References

---

[1] http://www1.eere.energy.gov/hydrogenandfuelcells/mypp/pdfs/production.pdf

[2] http://www.ewea.org/fileadmin/files/library/publications/statistics/Wind_in_power_2011_European_statistics.pdf

[3] http://www.technologyreview.com/news/427360/hydrogen-storage-could-be-key-to-germanys-energy/2/

[4] Gas World Magazine, 95, April 2013, p22.

[5] Wang, C.Y. and P. Cheng, *A multiphase mixture model for multiphase, multicomponent transport in capillary porous media--I. Model development.* International Journal of Heat and Mass Transfer, 1996. **39**(17): p. 3607-3618

[6] Wang, Z.H., C.Y. Wang, and K.S. Chen, *Two-phase flow and transport in the air cathode of proton exchange membrane fuel cells.* Journal of Power Sources, 2001. **94**(1): p. 40-50.

[7] Wang, Y., S. Basu, and C.-Y. Wang, *Modeling two-phase flow in PEM fuel cell channels.* Journal of Power Sources, 2008. **179**(2): p. 603-617.

[8] Ugur, P. and C.Y. Wang, *Liquid Water Transport in Gas Diffusion Layer of Polymer Electrolyte Fuel Cells*. 2004, ECS. p. A399-A406.